The Pennsylvania State University

The Graduate School

Department of Mechanical and Nuclear Engineering

DESIGN, FABRICATION, MODELING, AND EXPERIMENTAL TESTING OF A PIEZOELECTRIC FLEXTENSIONAL MICROACTUATOR

A Thesis in

Mechanical Engineering

by

Jongpil Cheong

Submitted in Partial Fulfillment
of the Requirements
for the Degree of

Doctor of Philosophy

May 2005

The thesis of Jongpil Cheong was reviewed and approved* by the following:

Christopher D. Rahn
Professor of Mechanical Engineering
Thesis Co-Advisor
Co-Chair of Committee

Srinivas Tadigadapa
Associate Professor of Electrical Engineering
Thesis Co-Advisor
Co-Chair of Committee

Eric Mockensturm
Assistant Professor of Mechanical Engineering

M. Amanul Haque
Assistant Professor of Mechanical Engineering

Richard C. Benson
Professor of Mechanical Engineering
Head of the Department of Mechanical Engineering

*Signatures are on file in the Graduate School

ABSTRACT

The necessity for reliable and low-cost microactuators capable of providing high resolution displacements and controlled force has been consistently being brought up because of their applications in RF and optical switches, microfluidic pumps and valves, micromanipulators for nanoscale handling and atomic force microscope drives. In this thesis, a piezoelectric flextensional microactuator is designed, fabricated, modeled, and tested for the amplification of the small piezoelectric strain to achieve large displacements. Bulk PZT material available in the form of 500 μm thick polished substrate is integrated with a precision micromachined silicon beam structure to fabricate the clamped-clamped flextensional microactuator. A high strength, high precision, and low temperature (~200 °C) In/Sn solder bonding process is developed and used to bond the PZT and the beam. This process can also be used for the heterogeneous integration of various materials for MEMS fabrication as well as for their packaging. The experimentally measured static deflection characteristics of the silicon micromachined beam show a flextensional gain factor of 20 with a large amplitude stroke of ~8 μm when actuated using -100 V to 100 V. The fabrication process produces devices with variable initial imperfection so a nonlinear model is developed to predict static and dynamic performance based on a polynomial curve fit of the initial shape. A static analysis of this model shows that for maximal actuator displacement, gain factor, and blocked force, the microactuator should have a thin beam structure and initial imperfection tuned to the maximum contraction provided by the PZT. For large PZT displacement, a perfect beam provides maximum gain factor but some imperfection is required to guarantee actuator

movement in the desired (up or down) direction. For small PZT displacement, more initial imperfection improves performance. The theoretical model, based on the measured initial beam shape, predicts the experimentally measured direction and magnitude of beam displacement for three devices. The dynamic response of the microactuator results from buckling of the clamped beam in response to contraction of the bonded PZT support. Unlike previous research where sinusoidal initial beam shapes are analyzed, in this work the polynomial initial beam shape enables more accurate prediction of beam natural frequencies, frequency response, and time response when compared with experimental results. The inclusion of squeeze film damping between the beam and PZT support enables the model to predict response times. Experiments show that mounting the PZT with soft carbon tape limits PZT vibration.

TABLE OF CONTENTS

LIST OF FIGURES

LIST OF TABLES

ACKNOWLEDGEMENTS

First of all, I am grateful to my parents for their love and support, especially giving me this chance to thank the following people.

I wish to express my sincere gratitude to Dr. Christoper Rahn and Dr. Srinivas Tadigadapa for their guidance, advice and support for me to pursue doctorate degree at the Penn State University. I would also like to thank the other members of my committee, Dr. Eric Mockensturm and Dr. M. Amanul Haque.

Facility support for this research from Electrical Engineering microfab and the staffs is sincerely appreciated. Also, I appreciate help of CNF in Cornell University in fabrication. I am also grateful to Dr. Qiming Zhang for his help to measure the dynamic response.

I would like to thank my colleagues in MEMS group of electrical engineering and in Mechatronics Research Lab of mechanical engineering. I would specially like to thank Dr. Eunki Hong for his help in fabrication.

I also want to acknowledge the financial support for my Ph.D. studies provided by Hacheong Academic Scholarship Foundation.

Finally, I would like to express my gratitude to my family, especially my lovely wife, Hyoeun for her invisible help at foreign land and my sweet son, Wonjun for preventing me from leading an idle life.

Chapter 1

Introduction

1.1 Motivation and Background

There are limitations of space, fabrication, and operation in MEMS. To overcome these limitations, the concept of a flextensional actuator that typically uses stacked peizoceramics and an external amplification mechanism to convert the motion generated by the stack to a usable output motion in the transverse direction is applied to this research (See Fig. **1.1**). The need for low-cost microactuators capable of providing controlled force, high resolution, and large displacements has been steadily growing due to their applications in RF and optical switches, microfluidic pumps and valves, micromanipulators for nanoscale handling and atomic force microscope (AFM) drives, and others. [1]. The performance of an actuator depends not only upon the mechanism of actuation used but also on the design and structure of the actuators [1]. Shape memory alloy actuators [2] can generate a large displacement and force, but their actuation frequency is poor. Electrostatic devices (See Fig. **1.2**), while relatively simple and inexpensive to fabricate, provide limited stroke, displacement, and linearity (and/or may require high actuation voltage) [3]. In comparison to electrostatic actuators, electromagnetic actuators are capable of generating stronger driving force over a long distance and can offer micrometer resolutions in linear motion but at a higher complexity [4]. On the other hand, piezoelectric materials exhibit high energy density, bipolar

actuation and high speed response to electric fields [5, 6]. Additionally, miniaturization of piezoelectric devices scales in a very desirable way. For example, if the thickness of the piezoelectric material is unchanged, then for a given electric field, the energy stored in the piezoelectric material scales as L^2 as the electrode dimensions are scaled by a factor of L. The displacement of the piezoelectric actuator, on the other hand scales, in proportion to L, resulting in the energy consumed per traveled distance to scale in proportion to L [7].

Many kinds of microelectronic devices have been already realized based on piezoelectric films [8] (See Fig. **1.3**). Although thin films of lead zirconate titanate (PZT) are increasingly being integrated into microsensors and microactuators, their electromechanical coefficients are still inferior to those of bulk PZT (See Fig. **1.4**) by factor of ~5 [6]. To exploit the full potential of piezoelectric actuation, it is, therefore, desirable to use bulk PZT material. Such integration has been hampered until now due to the lack of precision micromachining techniques applicable for processing bulk PZT material. An alternative approach is to integrate precision micromachined silicon structures on to PZT substrates. This has the advantage of being able to use the large array of silicon microfabrication techniques without the need to develop extensive micromachining capabilities for PZT. However, the success of this technique is predicated upon the availability of low-temperature (Preferably <200°C), precision aligned bonding techniques. This thesis develops a low temperature bonding technique [9, 10] for this purpose.

Although piezoceramic materials exhibits high electromechanical coefficients, the observed strain in these materials is very small (~ 0.1% for PZT) [11] (See Fig. **A.1**). Several structures have been implemented for the amplification of the small strain of the piezoelectric materials to achieve large displacements. Piezoelectric actuation structures can generally be categorized into one of three based on amplification function: externally leveraged, internally leveraged, and frequency leveraged (See [12] for more details). These techniques are based upon trading off the generative force to achieve a large out-of-plane displacement and are typically implemented as unimorph/bimorph and flextensional structures. Unimorph actuators are typically made of a bilayer structure consisting of a piezoelectric (active) thin film deposited on a passive material. Application of an electric field across the piezoelectric material results in the generation of a moment causing the freestanding actuator structure to bend out of plane. Piezoelectric thin film unimorph devices providing linear actuation with reasonable stroke have been recently demonstrated [13]. On the other hand, flextensional actuators like the Moonie [14, 15] and Cymbal [16-18] (See Fig. **1.5**) generally consist of a piezoelectric disk bonded to endcaps that flex in response to piezoelectric contraction. Thus, the small piezoelectric in-plane contraction is amplified through buckling of the flextensional structure to produce large transverse displacement [19]. Flextensional actuators have been successfully demonstrated in the macro-scale but have not yet been realized on the micro-scale. This thesis presents the design, fabrication, modeling, and operation characteristics of the first piezoelectric flextensional microactuators realized using silicon micromachining and low temperature wafer bonding techniques.

1.2 The Flextensional Microactuator

Figure 1.6 shows the schematic diagram of the flextensional microactuator. It consists of PZT substrate of length l_p, width w_p, and a thickness t_p and poled through the thickness of the material. A beam of length l_b, width w_b and thickness t_b is micromachined in silicon and bonded at the two ends to the PZT substrate as shown. Using the d_{31} piezoelectric effect, through-the-thickness electric field produces longitudinal PZT contraction and compressive stress in the silicon beam. The small PZT contraction is amplified by the clamped-clamped silicon micromachined structure as it moves transversely in response to the longitudinal compressive force. Depending on initial beam and/or bonding imperfections, the beam can either buckle up or down.

To realize this device, two different fabrication processes are used. The first technique consists of using a thin layer of degenerately boron-doped silicon and wet etching in ethylene-diamine-pyrocatechol (EDP) to define the silicon beam [20] and epoxy glue bonding the structure to the PZT. The primary goal of this fabrication process is to rapidly prototype a proof of concept device capable of the displacement amplification through the flextensional effect. However, this fabrication technique is not a precision batch fabrication process and thus had poor repeatability and unpredictable yield.

Thus, an alternative fabrication technique based on the use of deep reactive ion etching (DRIE) and low temperature solder bonding is developed. This technique exploits the precision micromachining techniques of silicon and integrates the structure with a high energy density bulk material such as PZT to maximize the mechanical performance

of the flextensional device. Silicon On Insulator (SOI) wafer is used to accurately control the thickness of the silicon beam on the PZT substrate. These fabrication processes are described in detail in Chapter **2**.

To investigate the response of the microactuator to applied voltage and forces, nonlinear static and dynamic model are developed. First, the static response is analyzed nonlinearly based on Fang and Wickert [21] in Chapter **3**. Variable initial shapes due to fabrication process are represented and applied with a 6^{th} order polynomial.

In Chapter **4**, the dynamic response is studied to predict response times and operational bandwidth and establish proper mounting configurations for dynamic operation. Researchers have studied the linear and nonlinear dynamics of buckled beams with pinned and clamped boundary conditions using modal and direct approaches (See [22] for a review). In this work, the initial shape is not due to buckling of an initially straight beam but due to small imperfections in the fabrication process that cause a non-sinusoidal initial shape. Thus, many of the previous results for buckled beams cannot be used. In [23], for example, the second natural frequency of a buckled beam is shown to be independent of initial shape, however. This is not true for a beam with an asymmetric initial shape. A number of researchers have applied buckled beam analyses based on sinusoidal initial shapes to static [21] and dynamic analysis of microbridges [24].

In this thesis, the actuator is theoretically modeled to predict dynamic response following the approach of [22, 23]. Unlike previous research, however, the beam shape can not be accurately approximated using a sinusoid. The theory is, therefore, extended to the 6^{th} order polynomial initial shape and the corresponding natural frequencies, frequency response, and step response are compared with experimental results.

1.3 Research Objectives

The objectives of this research are to design, fabricate, model, and experimentally test flextensional microactuators. The specific goals are as follows:

- ✓ Design a flextensional microactuator with high stroke, large blocking force, and high bandwidth.
- ✓ Develop a fabrication process for the realization of the proposed flextensional microactuators.
- ✓ Develop a low temperature solder bonding technique and an improved fabrication process for the realization of the actuator.
- ✓ Develop static models of the flextensional microactuators that predict stroke and blocking force.
- ✓ Develop dynamic models of flextensional microactuators that predict bandwidth and step and frequency response characteristics.
- ✓ Experimentally test the flextensional microactuators to demonstrate performance and validate the models.

1.4 Research Applications

We may be able to apply these flextensional actuators introduced in this thesis to many cases, for example, a MEMS contact or non-contact switch, a Grating Light Valve (GLV), and other similar fields. Figure **1.7** represents a typical MEMS switch. The signal line can be connected by the transversely deflected beam, and its position will be

able to located according to its own performance. On-off frequency of the signal will also depend on the frequency of the buckled beam. Figure **1.8** shows an example of mirror application. It could be used for non-contact switches. Unlike the contact switch, there is no limitation in position of the signal line. As another example in Fig. **1.9**, these flextensional actuators could be used as a GLV [25] that is an advanced application based on the mirror.

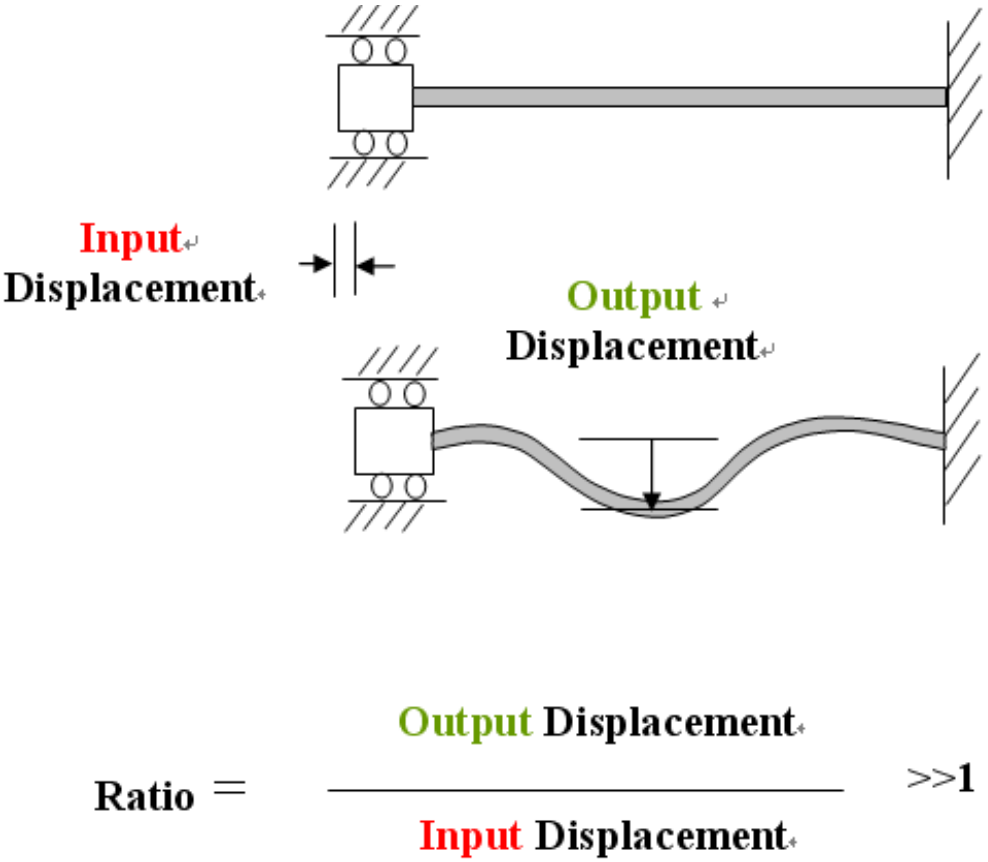

Fig. 1.1: Research concept.

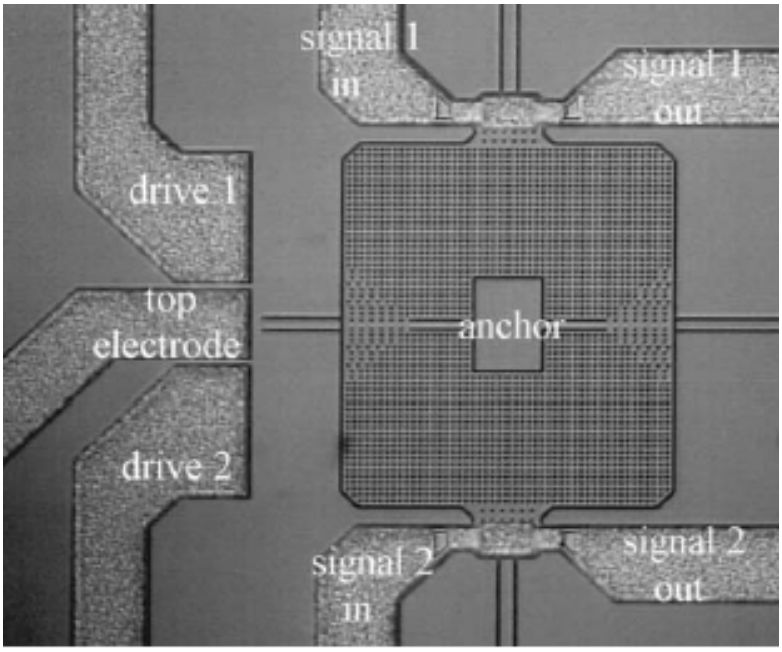

Fig. **1.2**: Electrostatic device [3].

This shown torsional switch is the example of the electrostatic device. By the electrostatic force, the rectangular plate is tilted to connect each signal line. This kind device is relatively simple and inexpensive, but it has limited stroke and linearity.

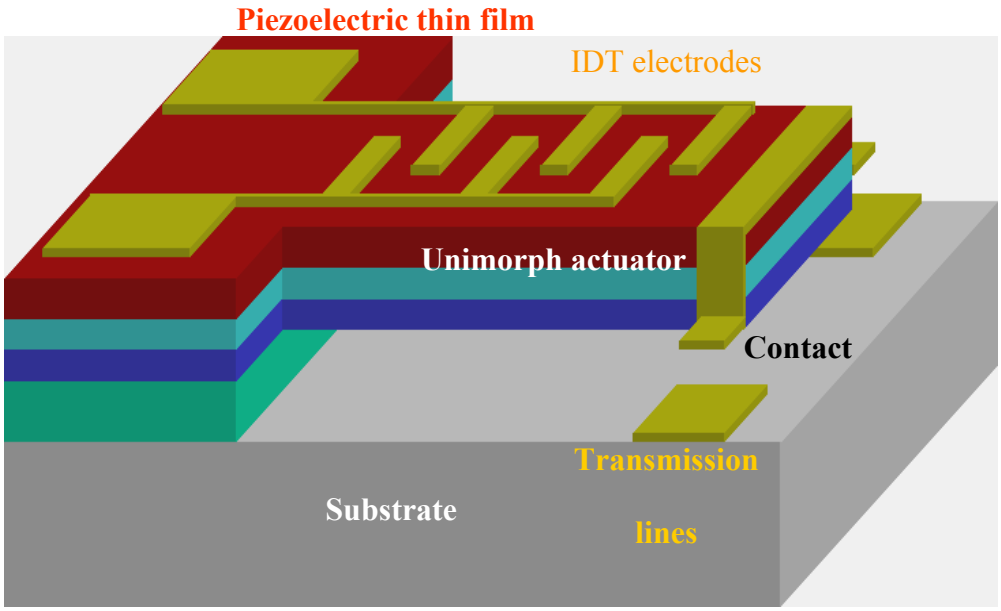

Fig. 1.3: Piezoelectric thin film unimorph device.

Gross, et al [13] have researched this RF switch. The cantilever beam is deflected by the piezoelectric thin film. This kind device provides linear actuation with reasonable stroke, but has limited force and limited strain due to PZT property.

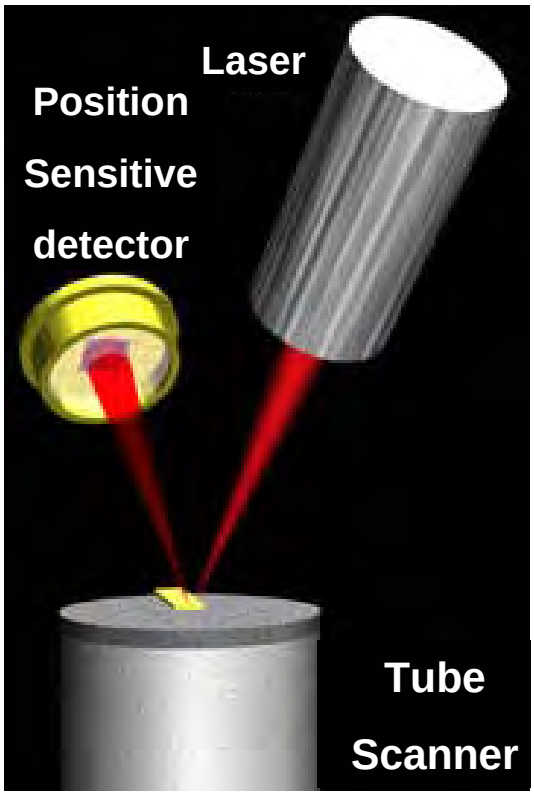

Fig. **1.4**: Monolithic piezoelectric device [26].

This shown device is used as a Tube scanner in AFM drive. This kind device generates high force and high energy density. This device also has limited strain due to the PZT.

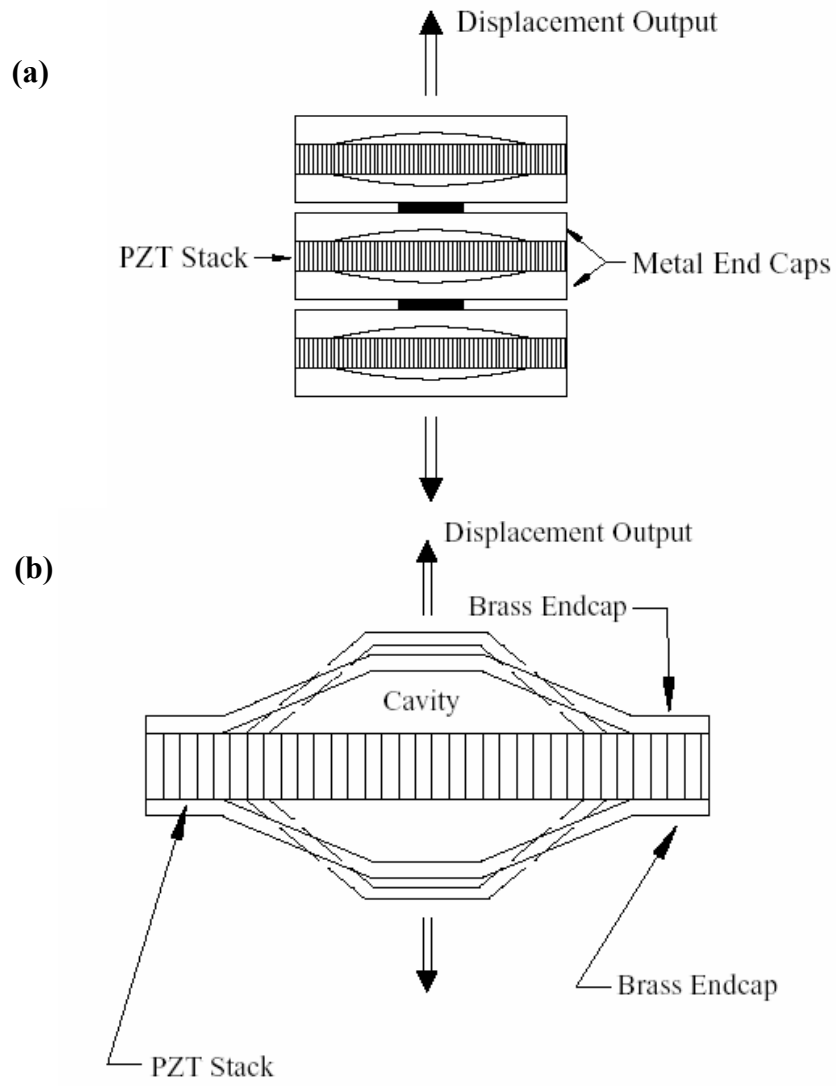

Fig. 1.5: Flextensional actuators.

This represents flextensional actuators whose meaning is combined with flexural and extensional. These are the examples of flextensional actuator in macro size. As shown here, flextensional actuator is called when the transverse displacement is generated or amplified by the longitudinal motion. The shown Fig. 1.5 (a) Moonie [15] and Fig. 1.5 (b) Cymbal [17] actuator is a typical example of the flextensional actuator.

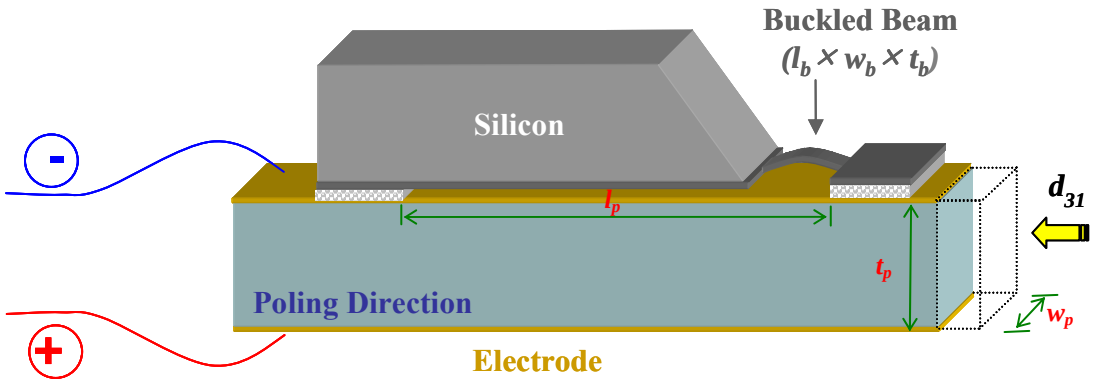

Fig. **1.6**: Principle of operation of a piezoelectric flextensional microactuator.

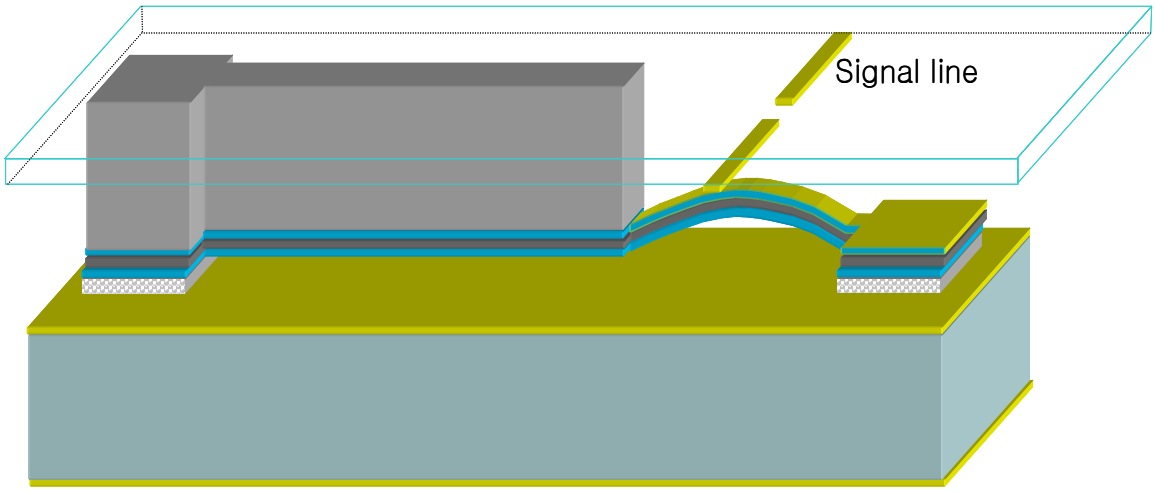

Fig. **1.7**: Example of switch application with a piezoelectric flextensional microactuator.

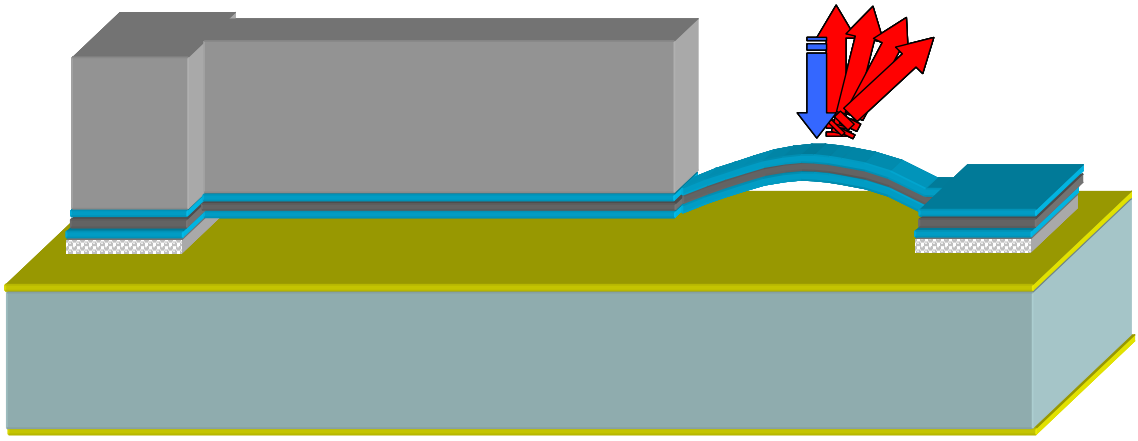

Fig. **1.8**: Example of mirror application with a piezoelectric flextensional microactuator.

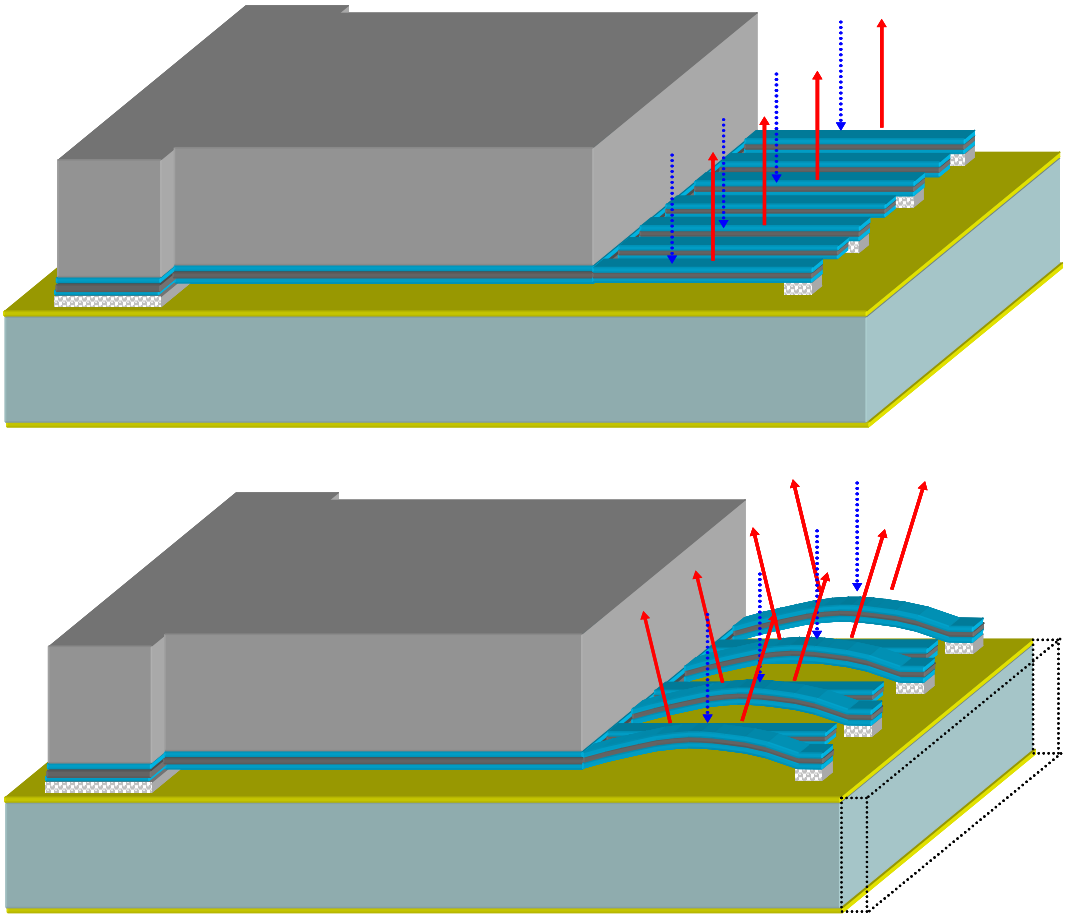

Fig. **1.9**: Example of Grating Light Valve (GLV) application with a piezoelectric flextensional microactuator.

References

1. Fujita, H., *Microactuators and Micromachines.* Proc. IEEE, 1998. 86(8): p. 1721-1732.

2. Mineta, T., et al., *An Active Guide Wire with Shape Memory Alloy Bending Actuator Fabricated by Room Temperature Process.* Sensors and Actuators A: Physical, 2002. 97-98: p. 632-637.

3. Sattler, R., et al., *Modeling of an Electrostatic Torsional Actuator Demonstrated with an RF MEMS.* Sensors and Actuators A, 2002. 97-98: p. 337-346.

4. Gong, Q., et al., *Design, Optimization, and Simulation on Microelectromagnetic Pump.* Sensors and Actuators A, 2000. 83: p. 200-207.

5. Flynn, A.M. and S.R. Sanders, *Fundamental Limits on Energy Transfer and Circuit Considerations for Piezoelectric Transformers.* Power Electronics, IEEE Transactions on, 2002. 17(1): p. 8-14.

6. Xu, F., et al. *Piezoelectric Films for MEMS Applications*. in *Electrets, 2002. ISE 11. Proceedings. 11th International Symposium on*. 2002.

7. Driesen, W., et al., *Energy Consumption of Piezoelectric Actuators for Inertial Drives.* IEEE Proc. Intl. Symp.on Miromechatronics and Human Science, 2003: p. 51-58.

8. Ren, T.-L., et al., *Piezoelectric and Ferroelectric Films for Microelectronic Applications.* Materials Science and Engineering, 2003(B99): p. 159-163.

9. Goyal, A., J. Cheong, and S. Tadigadapa, *Tin-based solder bonding for MEMS Fabrication and Packaging Applications.* Journal of Micromechanics and Microengineering, 2004(6): p. 819-825.

10. Cheong, J., Goyal A., Tadigadapa S., and Rahn C., *Reliable Bonding using Indium Based Solders.* Proceedings of the SPIE - The International Society for Optical Engineering, Reliability, Testing, and Characterization of MEMS/MOEMS III, 26-28 Jan. 2004, 2003. 5343(1): p. 114-20.

11. Uchino, K., *Piezoelectric Actuators and Ultrasonic Motors*. Electronic materials: Science and Technology, ed. H.L. Tuller. 1997: Kluwer Academic Publishers.

12. Niezrecki, C., et al., *Piezoelectric Actuation: State of the Art.* The Shock and Vibration, 2001. 33(4): p. 269-280.

13. Gross, S.J., et al., *Lead Zirconate Titanate-based Piezoelectric Micromachined Switch.* Applied Physics Letters, 2003. 83(1): p. 174-176.

14. R. E. Newnham, A.D., Q. C. Xu, and S. Yoshikawa, *Flextensional 'Moonie' Actuators.* Proc. IEEE Ultrason. Symp., 1993. 1: p. 509-513.

15. Onitsuka, K., et al., *Metal-Ceramic Composite Transducer, the 'Moonie'.* Journal of Intelligent Material Systems and Structures, 1995. 6: p. 447-455.

16. J. D. Zhang, A.C.H.-H., W. J. Hughes, R. E. Newnham, *Modeling and Underwater Characterization of Cymbal Transducers and Arrays.* IEEE Trans. Ultrason., Ferroelect., Freq. Contr., 2001. 48(2): p. 560-568.

17. Dogan, A., et al., *The Cymbal Electromechanical Actuator.* IEEE International Symposium on Applications of Ferroelectrics, 1996. 1: p. 213-216.

18. Dogan, A., K. Uchino, and R.E. Newnham, *Composite Piezooelectric Thansducer with Truncated Conical Endcaps 'Cymbal'.* IEEE Trans. Ultrason., Ferroelect., Freq. Contr., 1997. 44: p. 597-605.

19. Wang, Z., W. Zhu, and X. Yao, *d31 Type Inplane Bending Multilayer Pieozoelctric Microactuators-a Design Concept and Its Applications.* Sensors and Actuators A, 2002. 101: p. 262-268.

20. Tadigadapa, S. and S.M. Ansari. *Applications of High-performance MEMS Pressure Sensors Based on Dissolved Wafer Process*. in *Proceedings SENSORS EXPO Baltimore*. 1999. Baltimore, MD, USA: Helmers Publishing.

21. Fang, W. and J. Wickert, *Post Buckling of Micromachined Beams.* J. Micromech. Microeng., 1994. 4: p. 116-122.

22. Emam, S.A. and A.H. Nayfeh, *On the Nonlinear Dynamics of a Buckled Beam Subjected to a Primary-Resonance Excitation.* Nonlinear Dynamics, 2004. 35(1): p. 1-17.

23. Nayfeh, A.H. and W. Kreider, *Investigation of Natural Frequencies and Mode Shapes of Buckled Beams.* AIAA, 1995. 33: p. 1121-1126.

24. Nicu, L. and C. Bergaud, *Experimental and Theoretical Investigations on Nonlinear Resonances of Composite Buckled Microbridges.* Journal of Applied Physics, 1999. 86: p. 5835-5840.

25. Senturia, S.D., *Microsystem Design*. 2001: Kluwer Academic Publishers.

26. Binnig, G., C.F. Quate, and C. Gerber, *Atomic Force Microscope.* Phys. Rev. Lett., 1986. 56(9): p. 930-933.

Chapter 2

Fabrication

To realize this device, two different fabrication processes are used. The first technique consists of using a thin layer of degenerately boron-doped silicon and wet etching in ethylene-diamine-pyrocatechol (EDP) to define the silicon beam [1] and epoxy glue bonding the structure to the PZT. The primary goal of this fabrication process is to rapidly prototype a proof of concept device capable of the displacement amplification through the flextensional effect. However, this fabrication technique is not a precision batch fabrication process and thus had poor repeatability and unpredictable yield.

Thus, an alternative fabrication technique based on the use of deep reactive ion etching (DRIE) and low temperature solder bonding is developed. This technique exploits the precision micromachining techniques of silicon and integrates the structure with a high energy density bulk material such as PZT to maximize the mechanical performance of the flextensional device. Silicon on Insulator (SOI) wafer is used to accurately control the thickness of the silicon beam on the PZT substrate.

2.1 Method 1: Wet Etching (EDP) and Epoxy Glue

Figure 2.1 shows the important fabrication steps of the first fabrication procedure (See A.1). The beam structure is fabricated from a <100>, double side polished, 500 μm thick silicon wafer. Boron is diffused through the front surface of the wafer to a depth of

5 μm at a concentration of greater than 10^{19} cm^{-3}. The boron diffused Si layer acts as an etch stop layer when wet anisotropically etched in EDP. A thermal oxide layer was then grown to protect the backside silicon in the masked areas during EDP etching. Since the thermal oxidation process results in dopant redistribution, it was followed by a thermal annealing step to reduce any dopant gradients created thereof. The front oxide layer is removed. Lithography on the front side of the wafer defines the window regions where the boron doped Si layer is etched using reactive ion etching (RIE). To ensure that the silicon beam will be defined after EDP etching, the windows were etched to a depth of greater than 5 μm. This was followed by double side alignment and lithography for the definition of the through wafer etch window in EDP. Silicon is then etched in EDP etchant for nine hours. The anisotropic characteristic of the EDP etching results in a wall angle of 54.74 degrees. A polished bulk PZT substrate (APC-855, d_{31}= 276x10^{-12} m/V, Curie Temperature=250 °C, see Table **5.2**) was then coated with Cr/Au in an evaporator for defining the electrodes and cut to the desired size with a dicing saw. The silicon bridge was cut with a dicing saw and was bonded to the PZT substrate using an epoxy glue. Finally, the electrode wires are attached to apply electric field to the device. Figure **2.2** shows a schematic illustration of the fabricated device using this method and an optical picture of the flextensional silicon beam.

2.2 Indium Based Solder Bonding Process Development and Testing

The adhesive bonding technique used in the fabrication of the initial devices produced low yield and unpredictable results. Thus, a novel solder bonding technique is

developed using indium based solders. These solders have low bonding temperature to prevent depoling of the PZT. MEMS fabrication and packaging processes often require bonding technology that enables integration of dissimilar materials, including ceramics, ferroelectrics, polymers, semiconductors, and the others for device fabrication. A bonding technology, which is reliable and requires low processing temperature, is desirable not only to maintain the functionality of temperature sensitive materials but also to avoid stresses and deformations in materials due to differences in the coefficients of thermal expansions. Ideally, the bonding process should be independent of the substrate materials, highly reliable, easy to implement, and strong in bond strength. Additionally, patterned bond areas with high alignment accuracy are also desirable.

Several bonding techniques like anodic bonding [2, 3] and silicon-silicon direct bonding [4, 5] are available for joining substrates. Additionally, a number of intermediate-layer bonding processes have been researched for low temperature applications [6]. The use of solders as an intermediate layer is being brought up to meet the requirements. Some techniques for depositing and patterning of solders have been suggested [7-10]. Mixture of tin, indium, lead, and bismuth can provide many solder compositions for bonding applications. However, the use of lead is being decreased because of environmental contamination. Two solder compositions; one of pure indium (melting point 156°C) and the other of 52%In-48%Sn (atom %) alloy (melting point 118°C) have been investigated as a new bonding material for MEMS applications in this research [11]. Solders are used in flip-chip technology that has been applied for packaging electronic and optical components [12, 13]. The recent advances in this technology have been able to achieve bump diameters of 45 μm and bumping pitch of 60

μm with a placement accuracy of ±5 μm [14]. The novel bonding technique proposed in this research is motivated by tin solder bonding [15] that advances the flip-chip technology and attempts to exploit the existing bonding technologies for packaging and fabricating MEMS devices. Bonding using tin solder as an intermediate layer has already been investigated by the author and the others [15, 16]. An average tensile strength of 14 MPa, and hermetic sealing capabilities of better than $1x10^{-11}$ mbar-l/s are obtained using pure tin as the bonding material [16]. However, a temperature of 350°C for 25 minutes is required for tin solder based bonding. In order for this bonding technology to be useful for the fabrication of a flextensional MEMS actuator employing the bulk PZT, it is necessary to reduce the bonding temperature to ~200-250°C. Hence solder compositions with melting temperatures less than 250°C have been investigated as bonding layers.

2.2.1 Sample and Seed Layer Preparation

Polished 2.54 cm by 2.54 cm square Pyrex 7740 substrates are used for specimen preparation. A two stage cleaning step including acetone and IPA rinse followed by piranha clean (1 part H_2SO_4: 1 part H_2O_2) for half an hour is conducted to remove any impurities or organic films on the surface of the substrate for good bonding quality. 2000 Å thick gold layer is then deposited on a 200 Å thick chromium adhesion layer that is also deposited on the substrate by evaporation. The deposited Cr/Au layer is patterned as a square annulus using photolithography and wet etching processes.

Figure 2.3 illustrates the top view of the patterned seed layer. Four different bond areas as defined by the area of the square annulus are provides. The bond areas and the

area enclosed by the square annulus are also listed in Table 2.1. The patterned Cr/Au film acts as the seed layer for electroplating around 10 μm thick solder film. Since plating occurs only on the seed layer, the plated features can be exactly obtained as the seed layer.

2.2.2 Electroplating of the Solder Films

Electroplating is accomplished using a simple pulsed dc electrochemical set up as shown in Figs. 2.4 and 2.5 (See Fig. A.5 for more details). The use of pulsed power source results in the formation of a uniform solder film on the seed layer. Earlier electroplating efforts involving the use of a non-pulsed dc power source resulted in the formation of films with non-uniform thickness across the substrate with high wide wall build-up on the edges of the electroplated features, necessitating the use of a mechanical polishing step. The improvement in bond strength and bond uniformity accomplished using the polishing step has already been reported by the author [15]. The use of a pulsed power source eliminated build-up of sidewalls and also improved the uniformity of the electroplated solder film across the substrate. Advantages of Pulsed Electro Plating (PEP) include: 1) Higher uniformity in the deposited films because of better deposition in corners or spaces that would otherwise not receive the same coating thickness; 2) Films with fine grain structure because of the nucleation of new grains induced by pulsed dc current; 3) Control of crystal orientation through PEP can improve electrical and wear properties of plated films; and 4) Stress control in the deposited films by adjusting the duty cycle [17]. The uniformity of the electroplated solder across the substrate was further enhanced by using two contact pads (for the application of voltage during

electroplating) at the opposite edges of the seed layer rather than using only one contact pad. Further, variations in the thickness of the deposited solder arising from variation in concentration gradient of the electrolyte across the surface of the wafer and non-uniform distance between the anode and the sample are reduced by rotating the substrate during the electroplating process. However, due to the lack of continuous filtration, the surface roughness could not be reduced below 1 μm rms. Smoother films with smaller surface roughness may be obtained by continuous sub-micron level filtration of the electrolyte and continuous monitoring and stabilization of the pH of the electrolyte. In the present work, a magnetic stirrer was used to continuously refresh the solution at the cathode surface. This is because good agitation increases the maximum current that can be used by "pumping" reactants from the bulk solution into the regions near the cathode.

2.2.3 Bonding Process

Two chips with same patterns, with one having a hole drilled through its center, are then aligned and clamped together. The clamped substrates are then bonded in a vacuum ambient at the peak temperature of 225°C for 1 hour for indium and 200°C for 25 minutes for 52%In-48%Sn samples. The chamber is cleaned with nitrogen and forming gas (95% N_2+5% H_2) before bonding the two chips to prevent the formation of the oxygen and water vapor content in the bonding chamber because this step is not expected to remove the thin oxide film formed on the surface of electroplated solder, but made sure that there is no subsequent oxidation in molten solder. The native oxide films formed are typically ~10-50 nm thick. This is confirmed by Auger analysis of tin solder

films in a separate study wherein the solder surface shows presence of oxygen, sulfur, and some carbon. However, if the electroplated solder is milled by 50 nm in depth, all shown impurities are eliminated. The oxide film formed on the surface of the solder generally prevents the bonds to be reliable and strong. It also results in the formation of weak bonds when the bonding temperature is in the vicinity of the melting point of the solder or when the bonding times are somewhat short [15]. Thus, exposure of samples to a temperature of 225°C for one hour (or 200°C in the case of In-Sn alloy for 25 minutes) ensures the physical breakdown of the interfacial oxide thus resulting in molten solder to come into better contact with each other and resulting in the formation of strong and reliable bonds in the this study.

Molten indium and tin at the present bonding temperature are known to leach Au out of the seed layer. Such a leaching effect is more distinguished for tin as compared to indium. Since the thickness of the deposited Au is small compared to the thickness of the electroplated solder, the change in composition and hence properties of the solder due to dissolution of the seed layer into the molten solder is small. After the dissolution of Au, chromium film acts as the adhesion layer between the solder and the substrate. The bonded samples are then diced into individual dies of 8 mm by 8 mm for further characterization and testing.

2.2.4 Characterization and Testing

The substrate without the drilled hole was diced to be smaller than the substrate with the drilled hole as shown in Fig. 2.7. This enables clamping of the bonded samples

for tensile testing as well as hermetic sealing capabilities. A custom test fixture was designed for the evaluation of the tensile strength of bonds by the application of pneumatic pressure at the bond interface, and is shown in Fig. **2.8**. The bonds were evaluated for hermetic sealing capabilities using a commercial He leak detector.

2.3 Method 2: Dry Etching (DRIE) and Solder Bonding

For this method a different PZT material (APC-850, d_{31}= 175x10^{-12} m/V, Curie Temperature=360 °C) was used. The PZT material was changed because to achieve good bonding using the In-Sn solder the PZT samples had to be subjected to temperatures of ~200 °C. To avoid any depoling effects due to the bonding temperature a conservative specification of the Curie temperature for the PZT material was chosen. This material, however, had a lower piezoelectric d_{31} coefficient as specified above than the earlier PZT substrate. Figure **2.9** shows the second fabrication plan (See **A.2**). In this method, the beam structure is fabricated from a 5 μm thick silicon layer in a SOI (Silicon on Insulator) wafer. The handle layer in the SOI wafer was 500 μm thick, and the oxide layer was 0.47 μm thick.

The SOI wafer was thermally oxidized with an oxide thickness of 0.5 μm. The SOI wafer was diced into 2.54 cm by 2.54 cm chips which were easier to handle. The top side of the silicon wafer was patterned with 200 Å of Cr and 1000 Å of Au using lift-off method. The flextensional beam and the support thick silicon beam areas were defined using photolithography and were etched through the device silicon and the oxide layer into the substrate silicon in a reactive ion etcher. Using double side alignment, the backside oxide was patterned using a thick positive photoresist (AZ9260) and buffered oxide etch to define the support thick silicon beam areas. The 10 μm thick photoresist layer along with the 0.5 μm thick oxide layer acts as the mask for the through silicon

DRIE etch. A polished bulk PZT 500 μm thick is metallized on both sides with Cr/Au in an evaporator for making electrodes. One side of the PZT electrode and the patterned Cr/Au layer on the silicon chip were electroplated with 52 % In-48 % Sn solder. The electroplated solder thickness was around 8 μm. Electroplating was performed using a pulsed dc power supply, and the electroplating solution was magnetically stirred during the process to obtain a uniform deposition. The solder stoichiometry was maintained by accurately controlling the current and time of each component. Details of the solder electroplating and bonding process have been reported in detail elsewhere [18]. The electroplated SOI and PZT chips were aligned and clamped together and then bonded in a vacuum ambient for a duration of 1 hour at a temperature 200°C. Although 30 minutes have been determined to be sufficient for a good bond, an additional 30 minutes were added to ensure a good bond between the two chips. Prior to heating the bond chamber, it was flushed with nitrogen and forming gas (95% N_2 +5% H_2) to reduce any oxygen and water vapor in the chamber. Finally, the bonded device was etched in the DRIE for removing the substrate silicon from everywhere except where the thick silicon beams were desired. The oxide layer of the SOI wafer was the etch stop layer and accurately controlled the thickness of the flextensional beam realized using this method. Finally, the electrode wires were attached to the both electrodes of the PZT. Figure **2.10** shows an optical photograph of the fabricated flextensional device using this technique. Since the solder was electroplated in well defined areas as shown in Fig. **5.4**, the bonding occurred only in these areas and the flextensional device was accurately defined.

2.3.1 Bond Stress and In-Sn Solder Bonding

Both the SOI chip and the PZT were electroplated with the mixture of 52 % In-48 % Sn which has the lowest melting point (118 °C) of all alloys made of In/Sn and a tensile bond strength of 7.38 MPa [18]. The maximum stress (σ) generated in the PZT due to the application of the voltage across it can be estimated from the expression [19]

$$\sigma = Y\varepsilon = Y_p(d_{31}E_f) \qquad (2.1)$$

where Y_p is the Young's modulus of the PZT ($6.3\text{x}10^{10}\,Pa$), ε is the strain in PZT arising from the application of the electric field E_f, and d_{31} is the piezoelectric coefficient of PZT. At the maximum voltage suggested by the manufacturer of 250 V (corresponding to an electric field E_f(max.) = $5\text{x}10^5$ V/m), the maximum generated stress can be calculated using Eq. **2.1** to be 5.51 MPa. This generated stress results in a net generated force (P) being transferred to the beam and can be expressed as

$$P = Y_b\varepsilon w_b t_b = Y_b(d_{31}E_f\frac{l_p}{l_b})w_b t_b\,, \qquad (2.2)$$

where Y_b (125GPa [20-22]) is is the Young's modulus, w_b is width, t_b is thickness, and l_b is length of the etched beam, and l_p represents the length of the PZT as shown in Fig. **1.6**. Considering the Device 2 listed in Table **5.3**, the generated force can be calculated to be around 0.035 N. If this force is converted to stress using a bond area of 500 µm x 700 µm, the smallest bond area, the generated shear stress is 0.1 MPa. This is the maximum shear stress experienced by the bond areas as well as the stress which is transferred to the silicon beam by the PZT. Therefore, it can be concluded that the use of 52 % In-48 % Sn

is very resonable for this application. To verify the solder bond quality, the PZT was peeled off from an actuator. Figure **5.4** shows the bottom surface of the etched beam and the large rectangular bonding area. The uniformity of the asperities seen in Fig. **5.4** and the well defined geometry of the bond area show the suitability of this technique for realizing MEMS devices by the heterogeneous integration of materials.

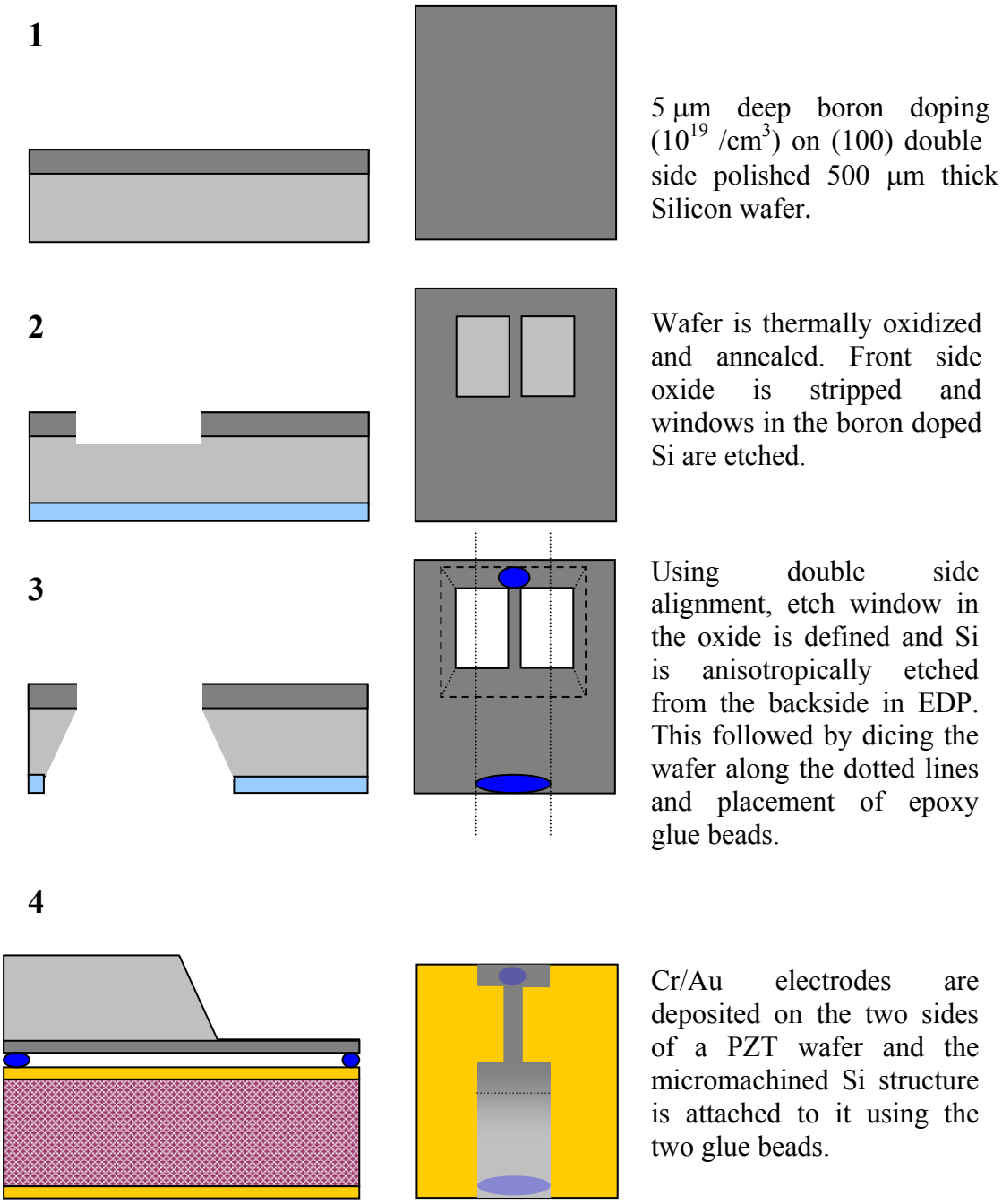

Fig. **2.1**: Schematic illustration of the fabrication process based on anisotropic EDP etching of silicon and adhesive bonding to PZT substrate.

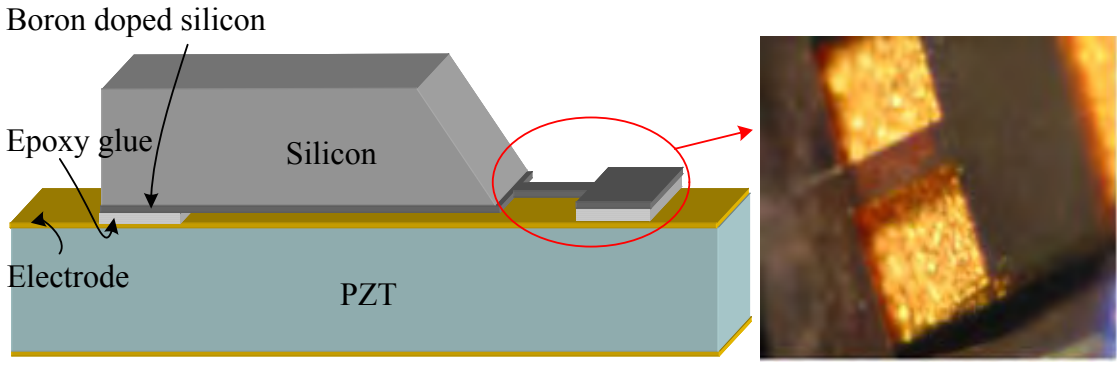

Fig. 2.2: Pictures of the flextensional microactuator fabricated using EDP etching and adhesive bonding.

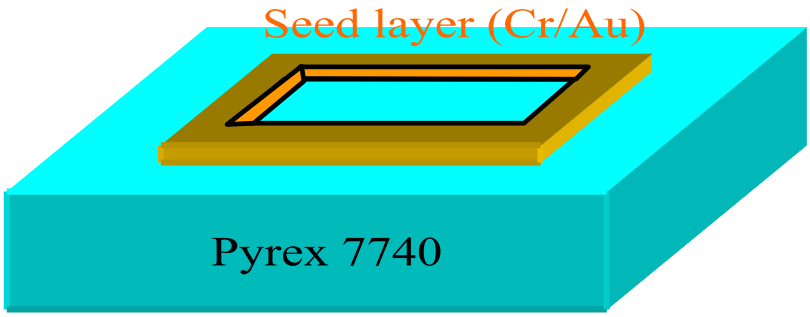

Fig. **2.3**: Top view of the seed metal layer shaped in the form of a square ring. Four different line widths were used in the present study thus yielding four different areas of the square ring.

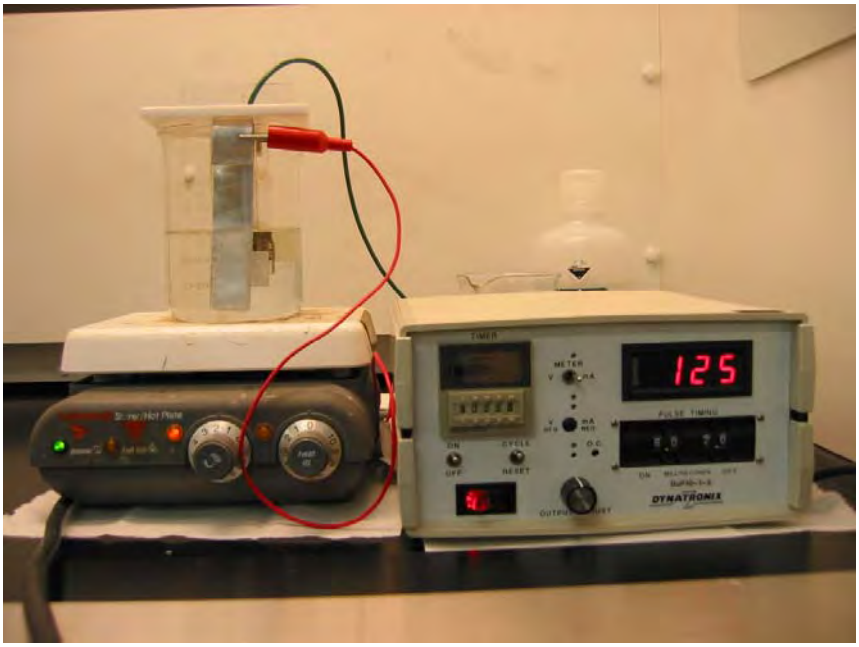

Fig. **2.4**: Picture of the pulsed electroplating apparatus.

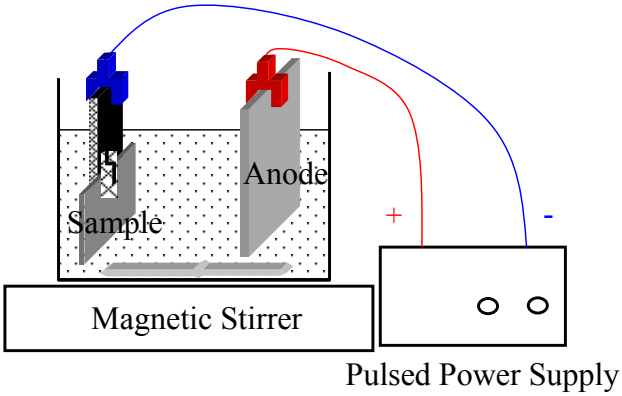

Fig. **2.5**: Schematic illustration of the pulsed electroplating apparatus.

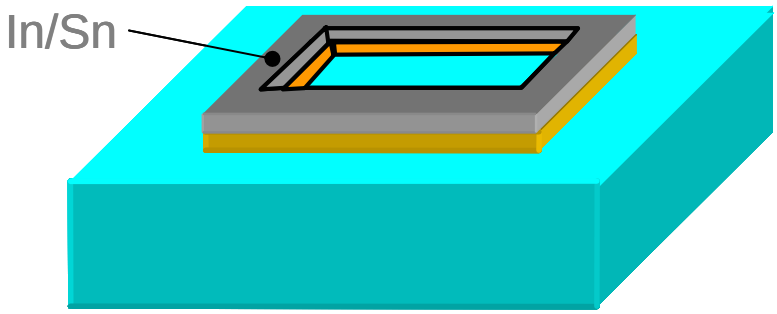

Fig. **2.6**: Schematic illustration of electroplated In/Sn.

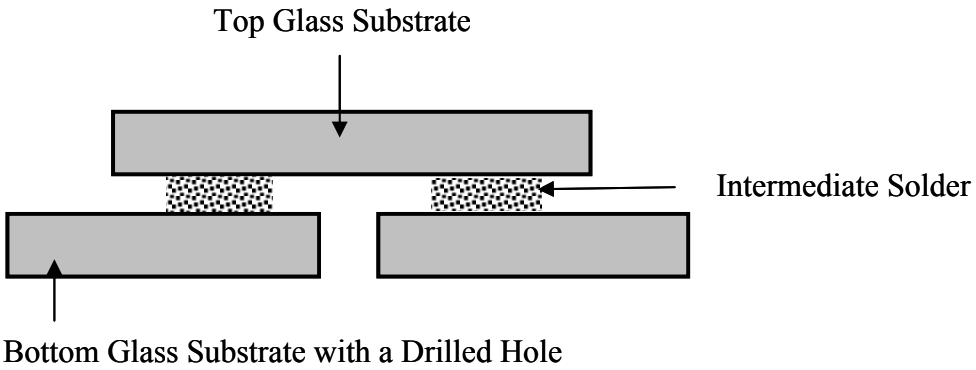

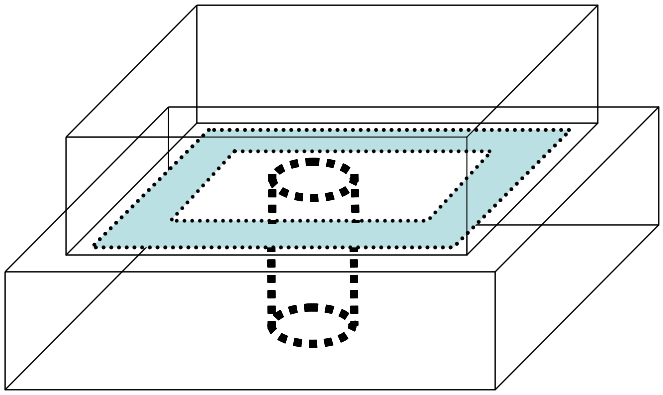

Fig. **2.7**: Cross section view of a bonded sample, showing a smaller top substrate and a larger bottom substrate with a hole drilled through its center

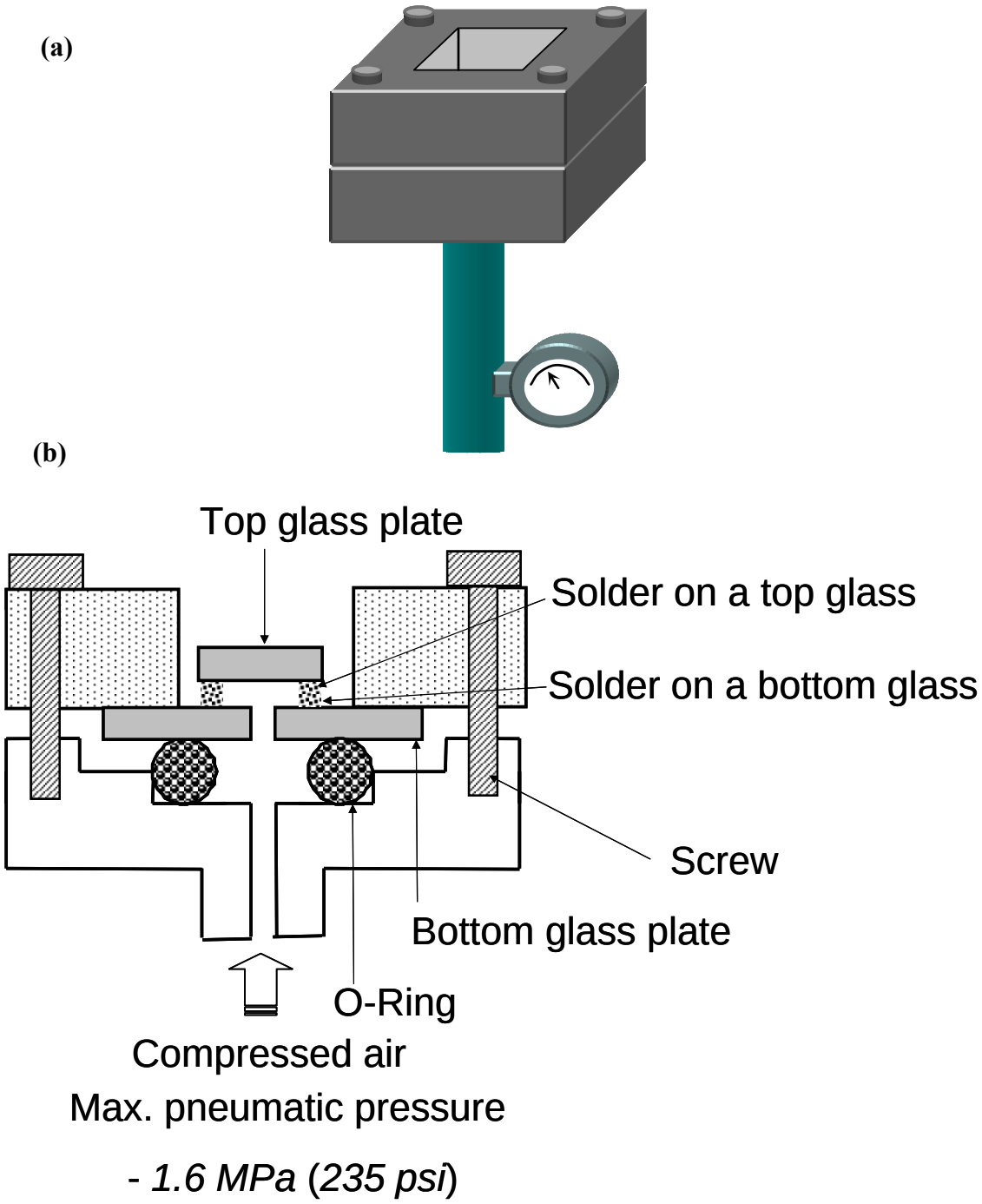

Fig. **2.8**: Custom test set up for tensile strength evaluation of bonds by application of pneumatic pressure: (a) schematic view and (b) cross section.

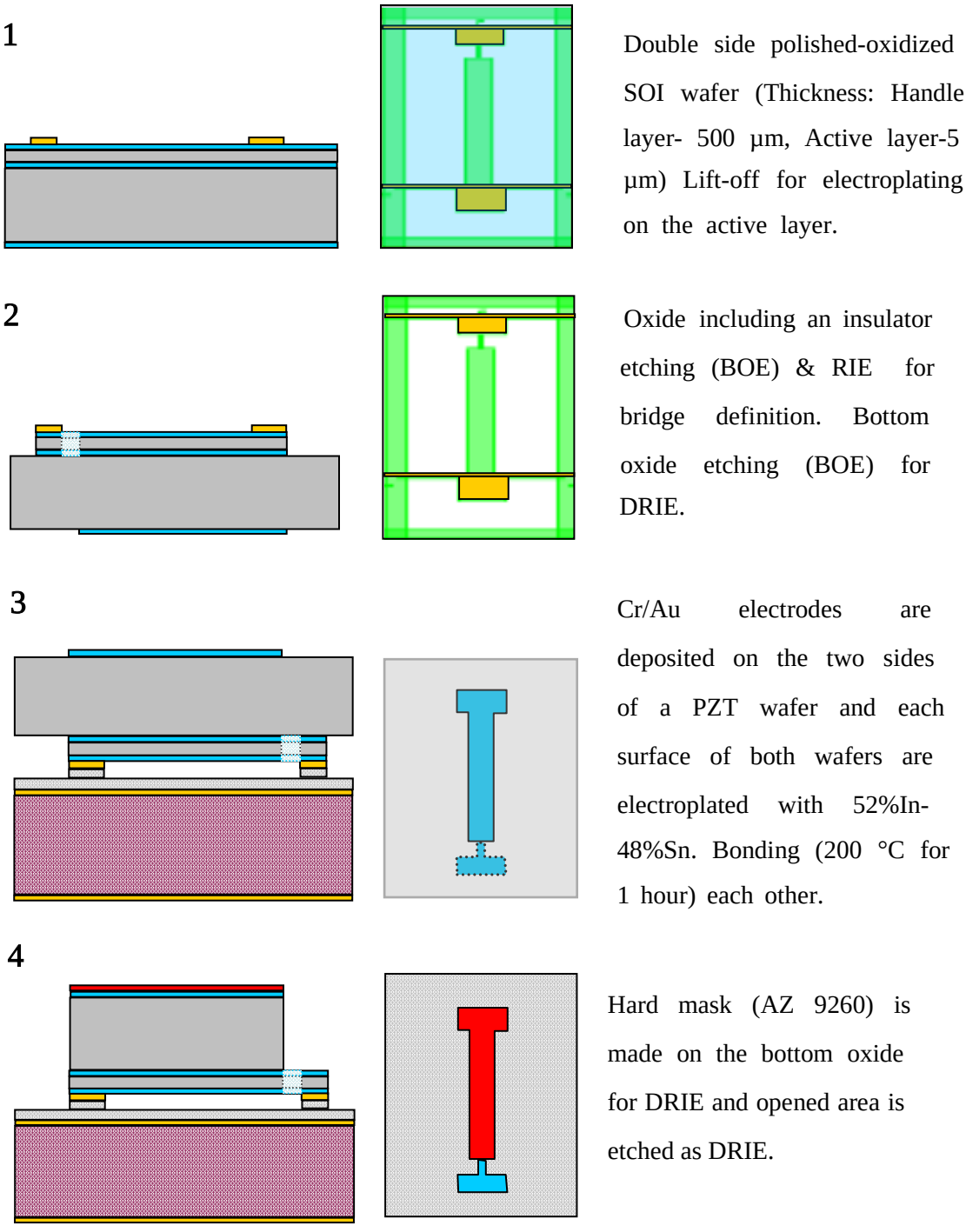

Fig. **2.9**: Schematic illustration of the fabrication process based on anisotropic DRIE etching of silicon and solder bonding to PZT substrate.

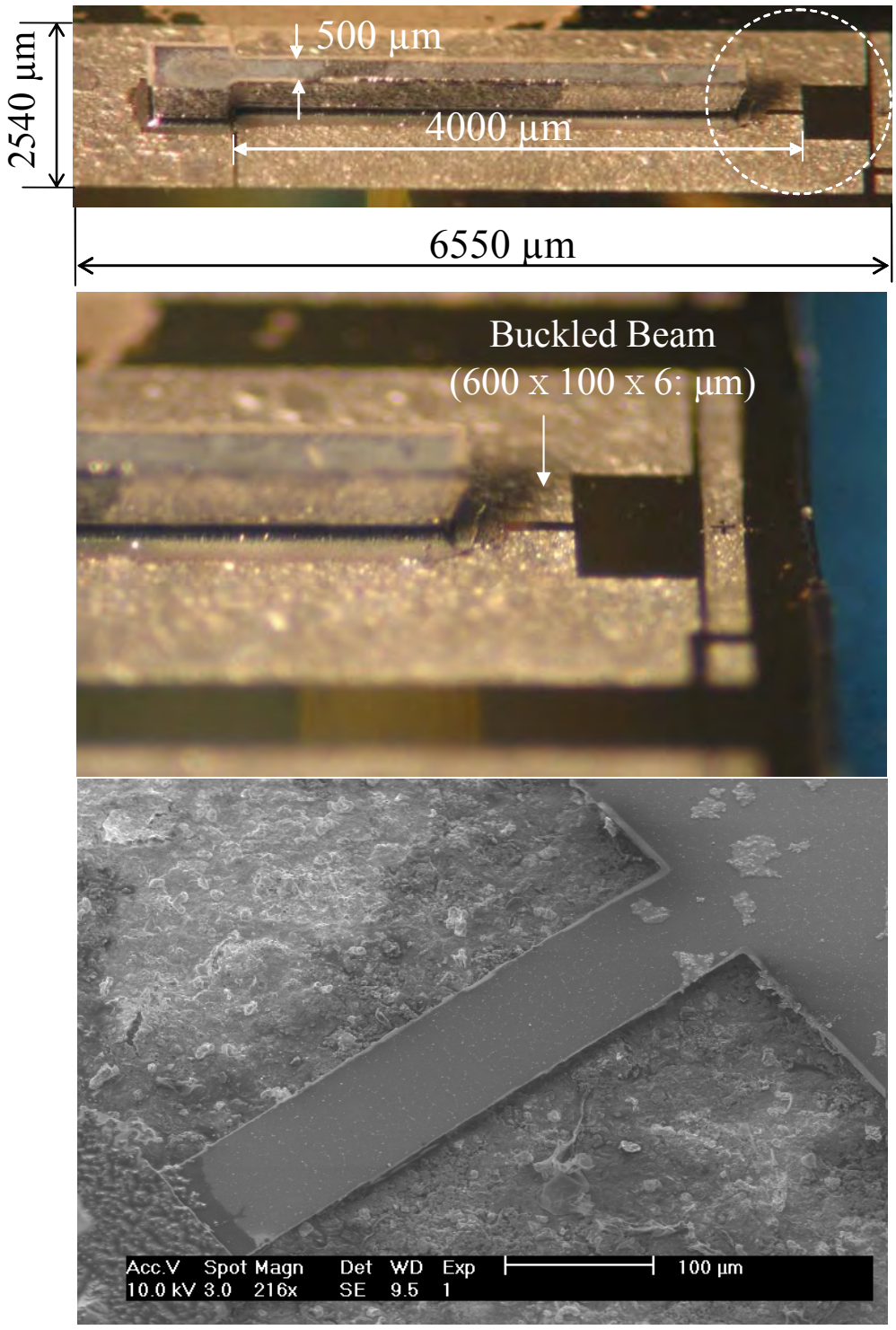

Fig. **2.10**: Pictures of the micro-flextensional actuator fabricated using SOI wafer, deep silicon etching and solder bonding process.

Table 2.1: Bond line widths, bond areas, and areas enclosed by the bonds.

Line Width (mm)	Area of Bond Pads, A_b (mm^2)	Area enclosed by bond pads, A_p (mm^2)
0.1	1.96	23.04
0.25	4.875	21.39
0.5	9.5	18.0625
1	19.6	15.21

References

1. Tadigadapa, S. and S.M. Ansari. *Applications of High-performance MEMS Pressure Sensors Based on Dissolved Wafer Process*. in *SENSORS EXPO Baltimore*. 1999. Baltimore, MD, USA: Helmers Publishing.

2. Wei, J., et al., *Low Temperature Wafer Anodic Bonding.* Journal of Micromechanics and Microengineering, 2003. 13(2): p. 217-222.

3. Wallis, G. and D.I. Pomerantz, *Field Assisted Glass-metal Sealing.* Journal of Applied Physics, 1969. 40(10): p. 3946-9.

4. Maszara, W.P., et al., *Bonding of Silicon-Wafers for Silicon-on-Insulator.* Journal of Applied Physics, 1988. 64(10): p. 4943-4950.

5. Thompson, K., et al., *Direct Silicon-silicon Bonding by Electromagnetic Induction Heating.* Journal of Microelectromechanical Systems, 2002. 11(4): p. 285-292.

6. Ristic, L.J., *Chapter 4/5*, in *Sensor Technology and Devices*. 1994, Artech House: Boston, MA.

7. Lemmerhirt, D.F. and K.D. Wise. *Field-operable Microconnections Using Automatically-triggered Localized Solder-bonding*. in *The Fifteenth IEEE International Conference on Micro Electro Mechanical Systems, 2002*. 2002.

8. Chan, W.K.Y.-Y., A.; Bhat, R., *Tip-chip Bonding: Solder Bonding to the Sides of Substrates*. Electronics Letters. Vol. 28. 1992. 1730-1732.

9. Cheng, Y.T., L. Lin, and K. Najafi, *Localized Silicon Fusion and Eutectic Bonding for MEMS Fabrication and Packaging.* Journal of Microelectromechanical Systems, 2000. 9(1): p. 3-8.

10. Lee, C.C., C.Y. Wang, and G.S. Matijasevic, *A New Bonding Technology Using Gold and Tin Multilayer Composite Structures.* IEEE Transactions on Components, Hybrids, and Manufacturing Technology, 1991. 14(2): p. 407-12.

11. Cheong, J., S. Tadigadapa, and C. Rahn. *Reliable Bonding Using Indium Based Solders*. 2004. Proceedings of the SPIE - The International Society for Optical Engineering, Reliability, Testing, and Characterization of MEMS/MOEMS III, 26-28 Jan. 2004, 2003. 5343(1): p. 114-20.

12. Singh, A., et al., *Batch Transfer of Microstructures Using Flip-chip Solder Bonding.* Journal of Microelectromechanical Systems, 1999. 8(1): p. 27-33.

13. Basavanhally, N.R., M.F. Brady, and D.B. Buchholz, *Optoelectronic Packaging of Two-dimensional Surface Active Devices.* IEEE Transactions on Components Packaging and Manufacturing Technology Part B-Advanced Packaging, 1996. 19(1): p. 107-115.

14. Beelen-Hendrikx, C. and M. Verguld. *Trends in Electronic Packaging and Aassembly for Pportable Consumer Products*. in Proceedings of 3rd Electronics Packaging Technology Conference (EPTC 2000) (Cat. No.00EX456). 2000. Singapore: IEEE.

15. Goyal, A., S. Tadigadapa, and R. Islam, *Solder Bonding for Microelectromechanical (MEMS) Fabrication and Packaging Applications.* Proceedings of the SPIE - The International Society for Optical Engineering, 2003. 4980: p. 281-8.

16. Goyal, A., J. Cheng, and S. Tadigadapa, *Tin-based Solder Bonding for MEMS Fabrication and Packaging Applications.* J. Micromech. Microeng., 2004. 14: p. 819-825.

17. Kovacs, G.T.A., *Micromachined Transducers-Sourcebook*. 1998: McGraw-Hill.

18. Cheong, J., Goyal A., Tadigadapa S., and Rahn C., *Reliable Bonding Using Indium Based Solders.* Proceedings of the SPIE - The International Society for Optical Engineering, Reliability, Testing, and Characterization of MEMS/MOEMS III, 26-28 Jan. 2004, 2003. 5343(1): p. 114-20.

19. Crandall, S.H., N.C. Dahl, and T.J. Lardner, *An Introduction to the Mechancs of Solids*. Second ed. Engineering Mechanics Series. 1978: McGRAW-HILL INTERNATIONAL EDITIONS.

20. Petersen, K.E., *Electron Devices ED-25.* IEEE Trans., 1978: p. 1241.

21. Roark, R.J. and W.C. Young, *Formulas for Stress and Strain*. 6th ed. 1989, New York: Mcgraw-hill.

22. Riethműller, W. and W. Benecke, *Thermally Excited Sillicon Microactuators.* IEEE Transactions on Electron Devices, 1988. 35(6): p. 758-763.

Chapter 3

Static Analysis

To investigate the response of the microactuator to applied voltage and forces, nonlinear static model is developed. First, the static displacement is analyzed nonlinearly and then the blocked force is also considered. Variable initial shapes due to fabrication process are represented and applied with a 6^{th} order polynomial.

3.1 Displacement

Figure 3.1 shows a schematic diagram of the buckling beam model used to predict the static performance of the actuator. The beam is clamped at $X = 0$ and l_b, has an initial shape $W_0(X)$, and is actuated at $X = l_b$ by the PZT. The PZT compresses the beam with load P, causing horizontal displacement of the right boundary U_L. Under assumptions of linear elasticity, static deformation, and small displacements, the transverse displacement is governed by

$$EI\left(\frac{d^4W}{dX^4}-\frac{d^4W_0}{dX^4}\right)+EA\left[-\frac{U_L}{l_b}-\frac{1}{2L}\int_0^{l_b}\left\{\left(\frac{dW}{dX}\right)^2-\left(\frac{dW_0}{dX}\right)^2\right\}dX\right]\frac{d^2W}{dX^2}=0, \qquad (3.1)$$

based on Fang and Wickert [1]. To minimize the number of parameters, we introduce the nondimensional variables and parameters

$$X=l_b x,\ W=l_b w,\ W_0=l_b w_0,\ U_L=l_b u_L,\ \text{and}\ v_l^2 = \frac{EAl_b^2}{EI}=\frac{12l_b^2}{t_b^2} \qquad (3.2)$$

for a square cross-section beam with thickness t_b. Substitution of Eq. **2.2** into Eq. **2.1** produces

$$\frac{d^4w}{dx^4}-\frac{d^4w_0}{dx^4}+v_l^2\left[-u_L-\frac{1}{2}\int_0^1\left\{\left(\frac{dw}{dx}\right)^2-\left(\frac{dw_0}{dx}\right)^2\right\}dx\right]\frac{d^2w}{dx^2}=0 \qquad (3.3)$$

Substitution of a sinusoidal initial imperfection and final displacement

$$w_0(x)=\frac{g}{2}\left[1-\cos(2\pi x)\right],\ w(x)=\frac{w_{\max}}{2}\left[1-\cos(2\pi x)\right] \qquad (3.4)$$

into Eq. **3.3** produces the polynomial

$$v_l^{\,2}\pi^2w_{\max}^3+\left(16\pi^2+4v_l^{\,2}u_L-v_l^{\,2}\pi^2g^2\right)w_{\max}-16\pi^2g=0 \qquad (3.5)$$

Given v_l^2 and u_L, the roots of Eq. **3.5** generate the maximum (midspan) displacement w_{max}.

Figure **3.2** shows the theoretical results for v_l = 360 with various initial imperfections. In Fig. **3.2** (a) the bifurcation diagram *w(1/2)* versus u_L shows an upward buckling curve (solid line) and, after the bifurcation point near u_L = -0.0003, two buckled down solutions (dashed and dotted line). Thus, for u_L < -0.0003, multiple solutions exist. These negative solutions would not be observed in practice, however, unless a large disturbance forces the beam into a negative equilibrium shape. The dashed solutions are unstable so they are not experimentally observed. With increasing initial imperfection, the upward displacement solution smoothes out between u_L = 0 and -0.0003. Fig. **3.2** (b) shows the change in displacement achieved from the initial imperfection [$w_0(1/2) = g$] to the final displacement $\Delta w_{max} = w(1/2) - g$. The actuator displacement or stroke is a figure of merit and Fig. **3.2** (b) shows that for small longitudinal displacement u_L > -0.0003, it

is advisable to use a large initial imperfection (g =*0.005*). If $g < 0.005$, then w *(1/2)* is smaller.

Increasing $g > 0.005$ increases the displacement for smaller u_L but decreases it for higher u_L. For actuators with $u_L < -0.0003$, maximum displacement occurs at $g = 0$, but the displacement direction is undetermined. Fig. **3.2** (c) shows another figure of merit, the gain factor $GF = [g - w(1/2)]/ u_L$. This measures the amplification of the longitudinal PZT motion by the flextensional structure. Again, for small u_L, $g = 0.005$ produces the largest gain factor. For $u_L < -0.0004$, however, the small imperfection case provides maximum amplification. Figure **3.3** shows that increasing v_l to 485 (increasing length or decreasing thickness according to Eq. **3.2** moves the bifurcation point closer to the origin and increases gain factor from $GF = 18$ at $u_L = -0.0006$ for $v_l = 360$ to $GF = 25$ at $u_L = -0.00035$ for $v_l = 485$. Thickness only appears in v_l, but l_b is used to nondimensionalize all the length variables (*e.g.* u_L). Thus, to maximize GF, the thickness should be minimized and the initial imperfection designed according to the available u_L.

The initial imperfection observed in the fabricated devices generally does not have a sinusoidal profile. To solve these more general cases, we observe that the nondimensional axial tension does not vary with x, so

$$p = \frac{l_b^{\,2}}{EI} P = v_l^2 \left[-u_L - \frac{1}{2} \int_0^1 \left\{ \left(\frac{dw}{dx} \right)^2 - \left(\frac{dw_0}{dx} \right)^2 \right\} dx \right] \qquad (3.6)$$

is constant. Substitution of Eq. **3.6** into Eq. **3.3** yields the linear, constant coefficient, ordinary differential equation

$$\frac{d^4 w}{dx^4} - \frac{d^4 w_0}{dx^4} + p\frac{d^2 w}{dx^2} = 0 \,. \qquad (3.7)$$

If we assume that the initial shape can be fit with a 6 order polynomial

$$w_0(x) = a_0 \; + \; a_1 x \; + \; a_2 x^2 \; + \; a_3 x^3 \; + \; a_4 x^4 \; + \; a_5 x^5 \; + \; a_6 x^6 \,, \qquad (3.8)$$

then the solution of Eq. 3.7 is

$$w(x) = \frac{-C_2 p \sin\left(\sqrt{p}x\right) - C_1 p \cos\left(\sqrt{p}x\right) + 12pa_4 x^2 + 20pa_5 x^3 + 30pa_6 x^4 - 360a_6 x^2}{p^2} + C_3 x + C_4 \,, \qquad (3.9)$$

where C_1, ..., C_3, and C_4 are constants of integration. Substitution of Eq. 3.9 into the boundary conditions

$$w(0) = a_0 \,, \quad \frac{dw}{dx}(0) = a_1 \,, \quad w(1) = \sum_{i=1}^{7} a_{i-1} \,, \quad \frac{dw}{dx}(1) = \sum_{i=1}^{6} a_i \,, \qquad (3.10)$$

results in four equations in four unknowns (C_1, ..., C_3, and C_4) that can be solved analytically (See section B.1). Thus, for a given initial shape (a_0, ..., a_5, and a_6) and compression p, the exact solution can be found. Then, given v_l, one can invert Eq. 3.6 to solve for u_L. Although the linear Eq. 3.7 has a unique solution, there are often multiple solutions with the same u_L calculated from the nonlinear Eq. 3.6. In the experiment, however, the input is the longitudinal contraction

$$u_L = -\frac{d_{31} l_p V}{t_p l_b} \,, \qquad (3.11)$$

where V is voltage applied across the PZT, and d_{31} is the piezoelectric charge constant.

3.2 Blocked Force

Figure 3.4 shows a schematic diagram of the blocked beam model used to predict the blocked force of the actuator. The objective is to determine the blocked force F_B as a function of the applied PZT force P and/or displacement U_L. We assume that the beam contacts a flexible point constraint with stiffness K at $X = A$. An external force F_0 is also applied at this point so the blocked force[2, 3]

$$F_B = F_0 + K[W^L(A) - W_0(A)], \tag{3.12}$$

where the domain is divided into $W^L(X)$ for $X \in (0, A)$ and $W^R(X)$ for $X \in (A, l_b)$. Using Eqs. 3.2, 3.7, and 3.12, and the same assumptions as in the previous section, the transverse displacement is governed by the nondimensional equations

$$\frac{d^4 w^L}{dx^4} - \frac{d^4 w_0}{dx^4} + p\frac{d^2 w^L}{dx^2} = 0 \tag{3.13}$$

$$\frac{d^4 w^R}{dx^4} - \frac{d^4 w_0}{dx^4} + p\frac{d^2 w^R}{dx^2} = 0. \tag{3.14}$$

The blocked force in Eq. 3.12 is also nondimensionalized as

$$f_B = \frac{l_b^{\,2}}{EI} F_B = f_0 + k[w^L(a) - w_0(a)] \tag{3.15}$$

where $k = \frac{l_b^{\,3}}{EI} K$ and $A = l_b a$. Substitution of the 6th order polynomial initial imperfection in Eq. 3.8 into Eqs. 3.13 and 3.14 produces solutions

$$w^L(x) = \frac{1}{p^2}\left[-D_2 p\sin\left(\sqrt{p}x\right) - D_1 p\cos\left(\sqrt{p}x\right) + 12pa_4x^2 + 20pa_5x^3 + 30pa_6x^4 - 360a_6x^2\right] + D_3x + D_4 \quad (3.16)$$

$$w^R(x) = \frac{1}{p^2}\left[-E_2 p\sin\left(\sqrt{p}x\right) - E_1 p\cos\left(\sqrt{p}x\right) + 12pa_4x^2 + 20pa_5x^3 + 30pa_6x^4 - 360a_6x^2\right] \cdot + E_3x + E_4 \quad (3.17)$$

To solve for unknown coefficients $D_1,...,E_4$, we use the boundary conditions

$$w^L(0) = a_0, \frac{dw^L}{dx}(0) = a_1, w^L(a) = w^R(a), \quad \frac{dw^L}{dx}(a) = \frac{dw^R}{dx}(a), \; w^R(1) = \sum_{i=1}^{7} a_{i-1}, \frac{dw^R}{dx}(1) = \sum_{i=1}^{6} a_i, \quad (3.18)$$

$$\frac{d^2w^L}{dx^2}(a) = \frac{d^2w^R}{dx^2}(a), \text{ and } \frac{d^3w^R}{dx^3}(a) - \frac{d^3w^L}{dx^3}(a) = -f_B \quad (3.19)$$

Equations **3.18** and **3.19** are the geometric and natural boundary conditions, respectively. Thus, the two exact solutions can be obtained for a given initial shape and contraction p and substituted into Eq. **3.12** to calculate the blocked force. Also, if one wants to know the blocked force according to u_L, one can invert Eq. **3.20** to solve for u_L.

Other approaches are described in section **B.2.**

$$p = \frac{l_b^2}{EI}P = v_l^2\left[-u_L - \frac{1}{2}\left[\int_0^a \left\{\left(\frac{dw^L}{dx}\right)^2 - \left(\frac{dw_0}{dx}\right)^2\right\}dx + \int_a^1 \left\{\left(\frac{dw^R}{dx}\right)^2 - \left(\frac{dw_0}{dx}\right)^2\right\}dx\right]\right]. \quad (3.20)$$

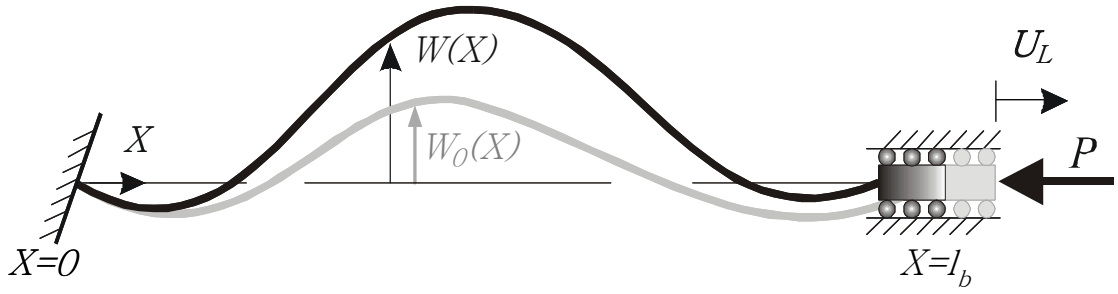

Fig. **3.1**: Schematic diagram of the buckling beam model.

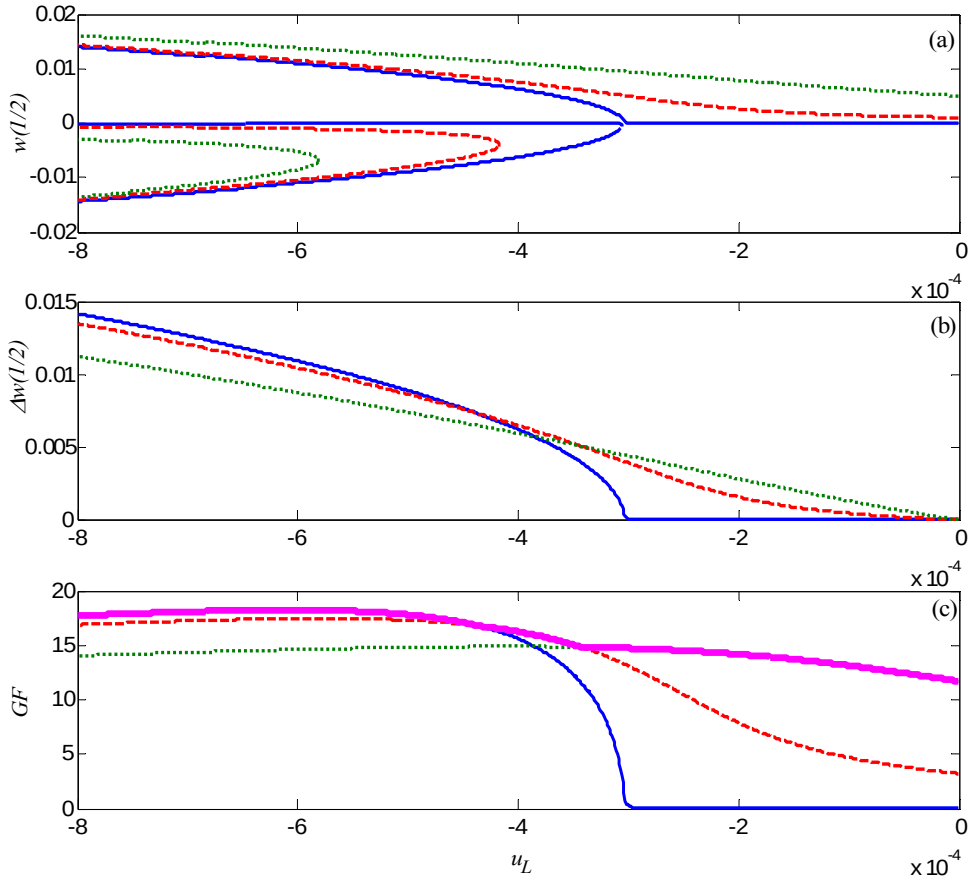

Fig. **3.2**: Theoretical results for sinusoidal initial shape ($v_l = 360$) for g = 1e-6 (solid), 1e-3 (dashed), and 5e-3 (dotted) versus longitudinal displacement u_L: (a) Midspan displacement $w(1/2)$; (b) Relative displacement $\Delta w(1/2) = w(1/2) - g$; (c) gain factor $GF = [g - w(1/2)]/ u_L$ (maximum shown with a thick line).

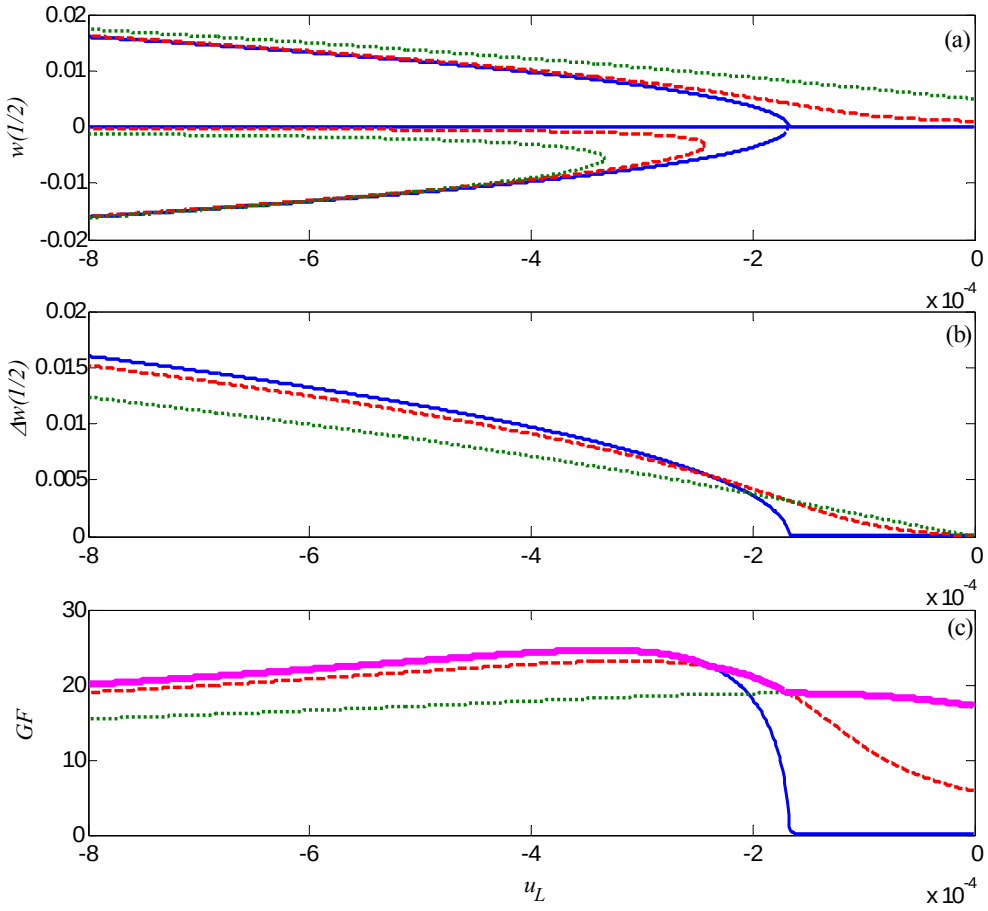

Fig. **3.3**: Theoretical results for sinusoidal initial shape (v_l = *485*) for g = 1e-6 (solid), 1e-3 (dashed), and 5e-3 (dotted) versus longitudinal displacement u_L: (a) Midspan displacement *w(1/2)*; (b) Relative displacement $\Delta w(1/2) = w(1/2) - g$; (c) gain factor $GF = [g - w(1/2)]/u_L$ (maximum shown with a thick line).

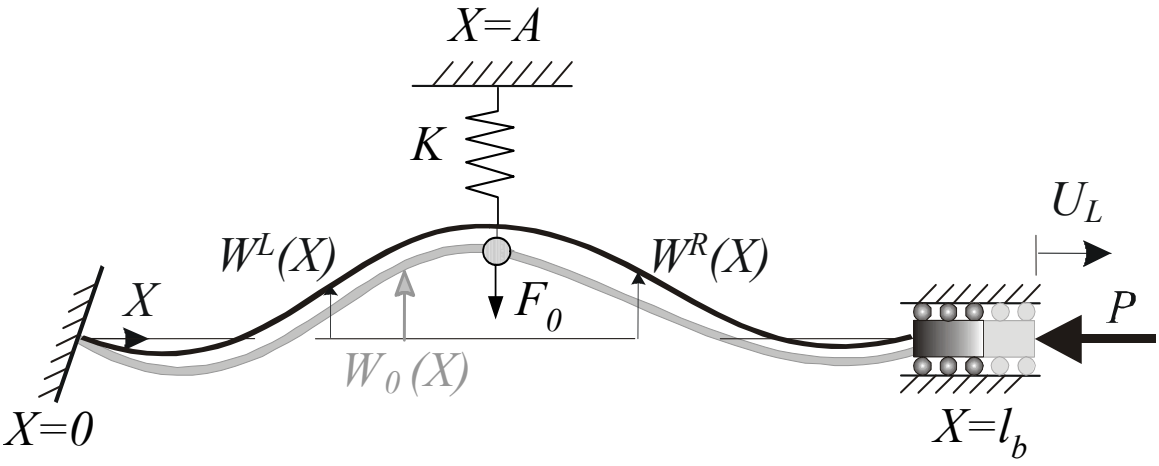

Fig. **3.4**: Schematic diagram of the blocked beam model.

References

1. Fang, W. and J. Wickert, *Post Buckling of Micromachined Beams.* J. Micromech. Microeng., 1994. **4**: p. 116-122.

2. Crandall, S.H., N.C. Dahl, and T.J. Lardner, *An Introduction to The Mechanics of Solids*. Second ed. Engineering Mechanics Series. 1978: Mcgraw-hill International Editions.

3. Timoshenko, S.P. and J.M. Gere, *Mechanics of Materials*. 1972, D.Van Nostrand.

Chapter 4

Dynamic Analysis

The dynamic response is studied to predict response times and operational bandwidth and establish proper mounting configurations for dynamic operation. Researchers have studied the linear and nonlinear dynamics of buckled beams with pinned and clamped boundary conditions using modal and direct approaches (See [1] for a review). In this work, the initial shape is not due to buckling of an initially straight beam but due to small imperfections in the fabrication process that cause a non-sinusoidal initial shape. Thus, many of the previous results for buckled beams cannot be used. In [2], for example, the second natural frequency of a buckled beam is shown to be independent of initial shape, however. This is not true for a beam with an asymmetric initial shape. A number of researchers have applied buckled beam analyses based on sinusoidal initial shapes to static [3] and dynamic analysis of microbridges [4].

In this thesis, the actuator is theoretically modeled to predict dynamic response following the approach of [1, 2]. Unlike previous research, however, the beam shape can not be accurately approximated using a sinusoid. The theory is, therefore, extended to the 6^{th} order polynomial initial shape and the corresponding natural frequencies, frequency response, and step response are compared with experimental results.

4.1 Linear Vibration Model

Figure 4.1 (a) shows a schematic diagram of the flextensional microactuator mounted on the holder by taping method. It consists of PZT substrate of length l_p, width w_p, and a thickness t_p, that is, and poled through the thickness of the material. A buckled beam of length l_b, width w_b, and thickness t_b is micromachined in silicon and bonded at the two ends to the PZT substrate as shown. Using the d_{31} piezoelectric effect, through-the-thickness electric field produces longitudinal PZT movement and axial stress in the silicon beam. The small PZT displacement is amplified by the clamped-clamped silicon micromachined structure as it moves transversely in response to the longitudinal motion. Depending on initial beam and/or bonding imperfections, the beam can either buckle up or down [5].

Figure 4.1 (b) shows a schematic diagram of the buckling beam model used to predict the dynamic performance of the actuator. The beam is clamped at $X = 0$ and $X = l_b$, has an initial shape $W_0(X)$, and is actuated at $X = l_b$ by the PZT. The PZT compresses the beam, causing horizontal displacement of the right boundary $U_L(T)$ and final transverse displacement $W(X,T)$. Under assumptions of linear elasticity and small displacements, the transverse displacement $W(X,T)$ is governed by

$$\rho\frac{d^2W}{dT^2} + C\frac{dW}{dT} + EI\left(\frac{d^4W}{dX^4} - \frac{d^4W_0}{dX^4}\right) + EA\left[-\frac{U_L}{l_b} - \frac{1}{2l_b}\int_0^{l_b}\left\{\left(\frac{dW}{dX}\right)^2 - \left(\frac{dW_0}{dX}\right)^2\right\}dX\right]\frac{d^2W}{dX^2} = 0 \tag{4.1}$$

where EA and EI are the axial and bending stiffness, ρ is the beam mass/length, and C is the viscous damping coefficient [5]. To minimize the number of parameters, we nondimensionalize as follows:

$$X = l_b x,\ W = l_b w,\ W_0 = l_b w_0,\ U_L = l_b u_L,$$
$$T = t\sqrt{\frac{\rho l_b^{\,4}}{EI}},\ C = c\sqrt{\frac{\rho EI}{l_b^{\,4}}},\ \text{and}\ \ v_l^2 = \frac{EAl_b^{\,2}}{EI} = \frac{12l_b^{\,2}}{t_b^{\,2}}. \qquad (4.2)$$

Substitution of Eq. 4.2 into Eq. 4.1 produces

$$\frac{d^2w}{dt^2} + c\frac{dw}{dt} + \frac{d^4w}{dx^4} - \frac{d^4w_0}{dx^4} + v_l^{\,2}\left[-u_L - \frac{1}{2}\int_0^1 \left\{\left(\frac{dw}{dx}\right)^2 - \left(\frac{dw_0}{dx}\right)^2\right\}dx\right]\frac{d^2w}{dx^2} = 0. \qquad (4.3)$$

We substitute

$$w(x,t) = w_0(x) + y(x,t), \qquad (4.4)$$

where displacement $y(x,t)$ is relative to the initial deflection [2, 4], into Eq. 4.3 to produce

$$\frac{d^2y}{dt^2} + c\frac{dy}{dt} + \frac{d^4y}{dx^4} + v_l^2\left\{-u_L - \frac{1}{2}\int_0^1 \left[2\frac{dw_0}{dx}\frac{dy}{dx} + \left(\frac{dy}{dx}\right)^2\right]dx\right\}\left(\frac{d^2w_0}{dx^2} + \frac{d^2y}{dx^2}\right) = 0. \qquad (4.5)$$

4.2 Modal Analysis

The linear vibration natural frequencies and mode shapes can be solved by neglecting the quadratic and cubic nonlinearities, damping ($c = 0$), and the input ($u_L = 0$) in Eq. 4.5.

Separation of variables

$$y(x,t) = Y(x)e^{i\omega t} \tag{4.6}$$

produces

$$\frac{d^4Y}{dx^4} - \omega^2 Y = v_l^2 \int_0^1 \left(\frac{dw_0}{dx}\frac{dY}{dx} \right) dx \frac{d^2 w_0}{dx^2}, \tag{4.7}$$

where $Y(x)$ is a nondimensionalized mode shape, and ω is the associated nondimensionalized natural frequency. The mode shapes satisfy the boundary conditions,

$$Y(0) = 0,\ \frac{dY}{dx}(0) = 0,\ Y(1) = 0,\ \text{and}\ \frac{dY}{dx}(1) = 0\,. \tag{4.8}$$

The integral term in Eq. 4.7

$$C_I = \int_0^1 \left(\frac{dw_0}{dx}\frac{dY}{dx} \right) dx \tag{4.9}$$

is constant, so Eq. 4.7 can be modified to

$$\frac{d^4Y}{dx^4} - \omega^2 Y = v_l^2 C_I \frac{d^2 w_0}{dx^2}\,. \tag{4.10}$$

If we assume as in [5] that the initial shape can be fit with a 6 order polynomial as Fig. 4.3

$$w_0(x) = a_0 + a_1 x + a_2 x^2 + a_3 x^3 + a_4 x^4 + a_5 x^5 + a_6 x^6 \tag{4.11}$$

then the solution of Eq. 4.10 is

$$\begin{aligned} Y(x) = {} & C_1 \sin(\sqrt{\omega}x) + C_2 \cos(\sqrt{\omega}x) + C_3 e^{\sqrt{\omega}x} + C_4 e^{-\sqrt{\omega}x} \\ & - 2C_I v_l^{\,2} (\omega^2 a_2 + 360 a_6 + 3a_3\omega^2 x + 6a_4\omega^2 x^2 + 10a_5\omega^2 x^3 + 15a_6\omega^2 x^4)/\omega^4 \end{aligned} \tag{4.12}$$

where C_1 ,..., C_4 and, C_I are constants of integration. Substitution of Eq. **4.12** into the four boundary conditions in Eq. **4.8** and integration of C_I results in five linear equations in the five unknown coefficients (See **C.2.1**). The natural frequencies and mode shapes are obtained numerically by determining the ω_i corresponding to singular coefficient matrices.

4.3 Frequency Response Function

The Frequency Response Function (FRF) is obtained from linearization of Eq. **4.5** to produce

$$\frac{d^2y}{dt^2}+c\frac{dy}{dt}+\frac{d^4y}{dx^4}-v_l^2\left[u_L+\int_0^1\left(\frac{dw_0}{dx}\frac{dy}{dx}\right)dx\right]\frac{d^2w_0}{dx^2}=0\,. \qquad (4.13)$$

We introduce the harmonic separation of variables

$$y(x,t)=Y(x)e^{i\omega t} \text{ and } u_L(t)=Ue^{i\omega t}\,. \qquad (4.14)$$

Substitution of Eq. **4.14** into Eq. **4.13** yields

$$\frac{d^4Y}{dx^4}+(ic\omega-\omega^2)Y=v_l^2\left[U+\int_0^1\left(\frac{dw_0}{dx}\frac{dY}{dx}\right)dx\right]\frac{d^2w_0}{dx^2}\,. \qquad (4.15)$$

If we again assume that the initial shape can be fit with the 6 order polynomial as in Eq. **4.11**, then the solution of Eq. **4.15** is

$$Y(x)=\mathbf{e}^{\mathbf{T}}(x)\mathbf{c}+d(x)U \qquad (4.16)$$

where

$$\mathbf{e}(x)=\begin{Bmatrix} e^{(-\omega(-\omega+ic))^{1/4}x} \\ e^{-(-\omega(-\omega+ic))^{1/4}x} \\ e^{i(-\omega(-\omega+ic))^{1/4}x} \\ e^{-i(-\omega(-\omega+ic))^{1/4}x} \\ \dfrac{d(x)}{2v_l^{\,2}} \end{Bmatrix}, \tag{4.17}$$

$$\mathbf{c}=[C_1\ C_2\ C_3\ C_4\ C_I]^{\mathrm{T}},$$

$$\begin{aligned} d(x)=2v_l^{\,2}\{&i2a_2c\omega^2+i20a_5x^3\omega^2c+i360a_6c-3a_3x\omega^3+3a_3x\omega c^2 \\ &-15a_6x^4\omega^3+6a_4x^2\omega c^2-10a_5x^3\omega^3+10a_5x^3\omega c^2+i6a_3x\omega^2c \\ &+15a_6x^4\omega c^2+i12a_4\omega^2c+a_2c^2\omega-a_2\omega^3-6a_4x^2\omega^3+i30a_6x^4\omega^2c \\ &-360a_6\omega\}/\{\omega^2(i2c\omega-\omega^2+c^2)(-\omega+ic)\} \end{aligned}$$

and C_1 ,..., C_4 and, C_I are constants of integration. Substitution of Eq. **4.16** into the boundary conditions in Eq. **4.8** and integration of C_I results in five equations in five unknowns.

$$\mathbf{A}(\omega)\mathbf{c}=\mathbf{b}(\omega)U \tag{4.18}$$

where $\mathbf{A}(\omega)$ and $\mathbf{b}(\omega)$ (See **C.2.2**) can be solved and substituted into Eq. **4.17** to produce

$$Y(x)=\left[\mathbf{e}^{T}(x)\mathbf{A}^{-1}(\omega)\mathbf{b}(\omega)+d(x)\right]U\,. \tag{4.19}$$

The experimentally measured FRF is the transverse beam velocity at $x=a$ in response to sinusoidal $u_L(t)$,

$$G(\omega)=\frac{i\omega Y(a)}{U}=i\omega\left[\mathbf{e}^{\mathrm{T}}(a)\mathbf{A}^{-1}(\omega)\mathbf{b}(\omega)+d(a)\right]. \tag{4.20}$$

4.4 Multi-mode Galerkin Discretization

To investigate the actuator time response we develop a nonlinear discretized version of Eq. **4.3** . Application of Galerkin's method to Eq. **4.3** produces the discretized equations

$$\frac{d^2\boldsymbol{\eta}}{dt^2} + 2\zeta\frac{d\boldsymbol{\eta}}{dt} + \left(\mathbf{D} - \mathbf{B}\,p(t)\right)\boldsymbol{\eta} = \mathbf{r}\,p(t)\,, \tag{4.21}$$

$$p(t) = v_l^2\left(-u_L(t) - \frac{1}{2}\boldsymbol{\eta}^T\mathbf{B}\boldsymbol{\eta} - \mathbf{r}^T\boldsymbol{\eta}\right), \tag{4.22}$$

where

$$\begin{aligned}
\zeta &= \frac{C}{2\rho}\sqrt{\frac{\rho l_b^4}{EI}},\\
\mathbf{B} &= \int_0^1 \frac{d\mathbf{w}}{dx}\frac{d\mathbf{w}^T}{dx}dx,\\
\mathbf{D} &= \int_0^1 \frac{d^2\mathbf{w}}{dx^2}\frac{d^2\mathbf{w}^T}{dx^2}dx,\\
\mathbf{r} &= \int_0^1 \frac{d\mathbf{w}}{dx}\frac{dw_0}{dx}dx,
\end{aligned} \tag{4.23}$$

with $w(x,t) = \mathbf{w}^T(x)\boldsymbol{\eta}(t)$, $\mathbf{w}(x) = [w_1(x),...,w_N(x)]^T$, $\boldsymbol{\eta}(t) = [\eta_1(t),...,\eta_N(t)]^T$, and the orthogonalized comparison functions $w_i(x)$ are the clamped-clamped beam eigenfunctions (See **C.3**). A four-mode ($N = 4$) approximation provides sufficiently accurate response. Eqs. **4.21** and **4.22** are bilinear in the input $u_L(t)$ and strictly bilinear for $w_0(x) = 0$ ($\mathbf{r} = 0$). The system also has quadratic ($\mathbf{r}^T\boldsymbol{\eta}\boldsymbol{\eta}$) and cubic ($\boldsymbol{\eta}^T\mathbf{B}\boldsymbol{\eta}\boldsymbol{\eta}$) nonlinearities.

4.5 Experimental Method

4.5.1 Test Stand Design

Figure 4.2 shows the experimental test stand used to measure the dynamic response. The function generator output is amplified and applied to the PZT. A fiber optic interferometer is used to measure transverse beam velocity at $x = a$.

4.5.2 Device Clamping Methods

Figure 4.1 shows the two clamping techniques that are investigated for holding the device. The clamps must fix the PZT but allow longitudinal motion. First, a solid clamp is applied to the end of the PZT. The PZT vibration, however, appeared in the beam response. Then, to damp the vibration and more securely fix the PZT, double sided adhesive conductive tape is applied between the PZT and base. The tape prevents vertical PZT motion but allows longitudinal PZT motion (See C.1).

4.5.3 System Parameters

The actuator beam is a composite consisting of 5 μm Si sandwiched with 0.5 μm SiO_2 on top and bottom. Thus,

$$\rho A = \rho_{Si} A_{Si} + \rho_{SiO_2} A_{SiO_2} \tag{4.24}$$

$$EI = \frac{b\left[E_{Si}{}^2 t_{Si}{}^4 + E_{SiO_2}{}^2 t_{SiO_2}{}^4 + E_{Si}E_{SiO_2}t_{Si}t_{SiO_2}(4t_{Si}{}^2 + 6t_{Si}t_{SiO_2} + 4t_{SiO_2}{}^2)\right]}{12\left(E_{Si}t_{Si} + E_{SiO_2}t_{SiO_2}\right)} \tag{4.25}$$

where $E_{Si} = 162\ GPa$, $\rho_{Si} = 2420\ Kg/m^3$, $E_{SiO_2} = 67\ GPa$, and $\rho_{SiO_2} = 2660\ Kg/m^3$ [6-8]. The remaining parameters for the three experimental devices tested are shown in Table **5.3.**

The 6th order polynomial represents the initial shape more precisely than the sinusoidal profile used in previous research [5]. Figure **4.3** shows the initial shape of the three actuators tested as measured by a white light interference microscope. Best fit 6th order polynomial (solid) and sinusoidal (dashed) curves are also shown. Least square curve fitting is used with the R^2 fit values shown in Table **5.3** [9]. The polynomial curves more accurately match the experimental data and allow asymmetry in the theoretical initial deflection that is not possible with a sinusoidal curve. The R^2 values in Table **5.3** also reflect the improved accuracy of the polynomial fit ($R^2 = 0.989 \sim 0.999$) over the sinusoidal fit ($R^2 = 0.899 \sim 0.948$). The damping constant C (kg/s/m) in Eq. **4.1** is primarily due to squeeze-film effects

$$C = \frac{96 \mu w_b^{\ 3}}{\pi^4 h_0^{\ 3}} \qquad (4.26)$$

where μ is the viscosity of air, and h_0 is the average gap between the PZT and the beam [10].

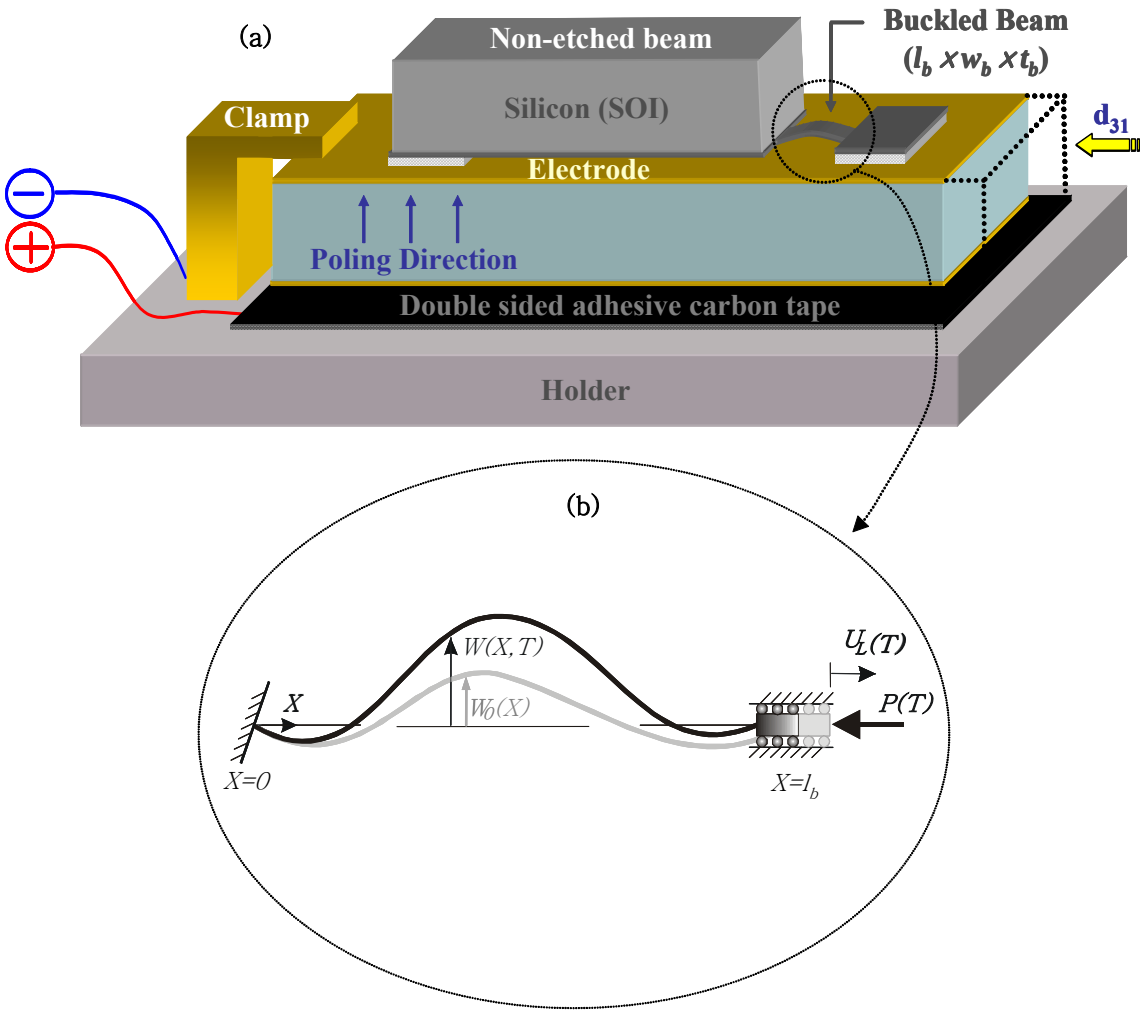

Fig. **4.1**: Flextensional microactuator: (a) concept and (b) dynamic model.

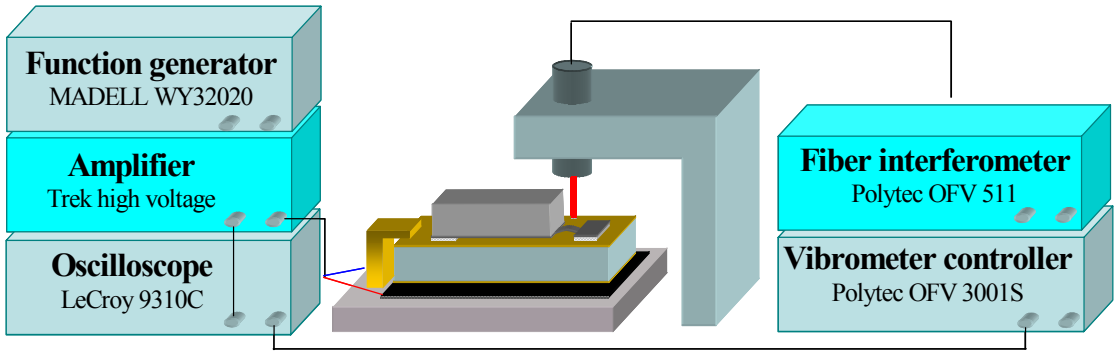

Fig. **4.2**: Experimental test stand.

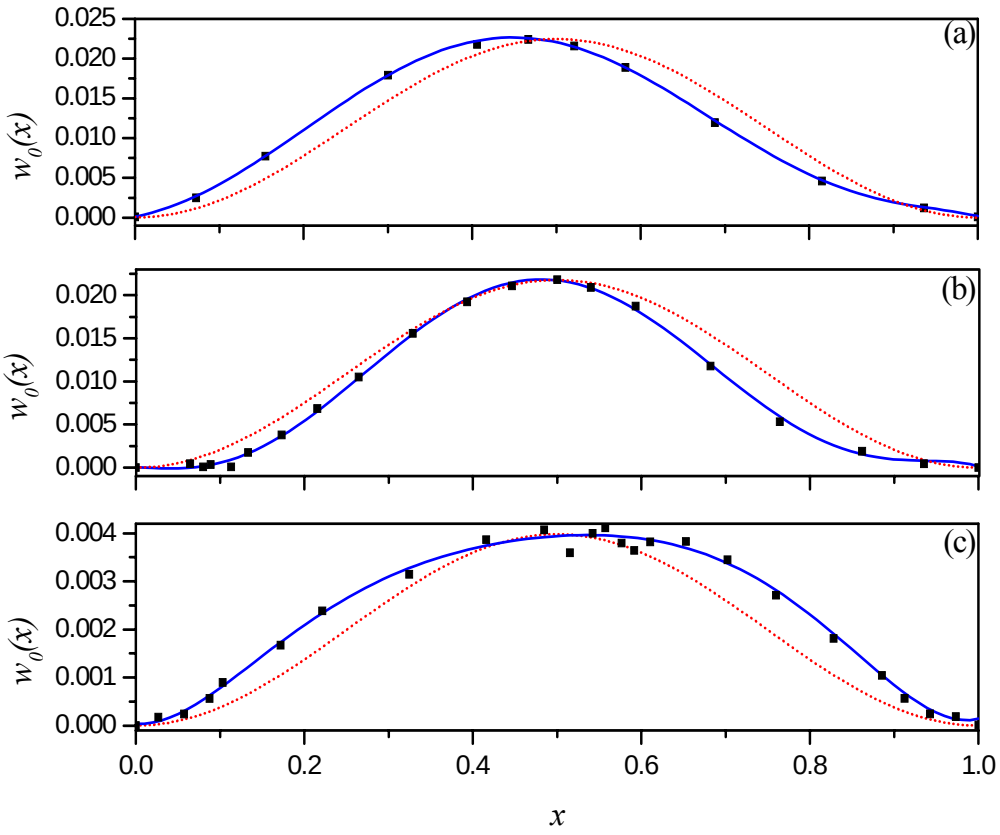

Fig. **4.3**: Initial beam shape [data (▪), best-fit sinusoidal (---), and best-fit polynomial (—)]: (a) Device 1, (b) Device 2, and (3) Device 3.

References

1. Emam, S.A. and A.H. Nayfeh, *On the Nonlinear Dynamics of a Buckled Beam Subjected to a Primary-Resonance Excitation.* Nonlinear Dynamics, 2004. 35(1): p. 1-17.

2. Nayfeh, A.H. and W. Kreider, *Investigation of Natural Frequencies and Mode Shapes of Buckled Beams.* AIAA, 1995. 33: p. 1121-1126.

3. Fang, W. and J. Wickert, *Post Buckling of Micromachined Beams.* J. Micromech. Microeng., 1994. 4: p. 116-122.

4. Nicu, L. and C. Bergaud, *Experimental and Theoretical Investigations on Nonlinear Resonances of Composite Buckled Microbridges.* Journal of Applied Physics, 1999. 86: p. 5835-5840.

5. Cheong, J., S. Tadigadapa, and C. Rahn. *Piezoelectric Micro-flextensional Actuator*. in *Proceedings of the SPIE - The International Society for Optical Engineering*. 2004. San Jose, CA.

6. Petersen, K.E., *Electron Devices ED-25.* IEEE Trans., 1978: p. 1241.

7. Riethműller, W. and W. Benecke, *Thermally Excited Sillicon Microactuators.* IEEE Transactions on Electron Devices, 1988. 35(6): p. 758-763.

8. Roark, R.J. and W.C. Young, F*ormulas for Stress and Strain.* 6th ed. 1989, New York: Mcgraw-hill.

9. Devore, J.L., *Probability and Statistics for Engineering and The Sciences.* Fourth ed. 1995: Wadsworth Inc.

10. Senturia, S.D., *Microsystem Design.* 2001: Kluwer Academic Publishers.

Chapter 5

Results and Discussion

5.1 In/Sn Solder Bonding

5.1.1 Solder Bonding and Bond Stress

It was very important to make sure that the composition of the electroplated solder for In-Sn alloy was as close to 52%-48% as possible. This is because the alloy shows the lowest melting point at this composition and any variation in the alloy composition from this ratio results in an increase in the melting temperature as seen in the In-Sn phase diagram (Fig. **5.1**) [1]. Control over solder composition was achieved by controlling the electroplating current and time. A multilayer with tin layer sandwiched between indium layers was electroplated to form the desired 52%In-48%Sn intermetallic alloy.

5.1.1.1 Tensile Strength

Samples were tested for tensile strength by subjecting them to pneumatic pressures in the custom test fixture as shown in Fig. **2.8**. The maximum pneumatic pressure that could be applied with the present set up was 1.6 MPa (235 psi). Samples prepared using pure In and 52%In-48%Sn as the intermediate bonding layers were tested.

The pneumatic pressure at which failure occurred (pressure at which complete detachment of the substrates occurred at the bond interface), was used to calculate the tensile strength of the bonds, using the following formula

$$\text{Bond Strength (MPa)} = P_a \times \frac{A_p}{A_b}, \qquad (5.1)$$

where P_a is the applied pneumatic pressure (MPa), A_p is the area over which the pneumatic pressure is applied and A_b is the bond area. The values of A_p and A_b are listed in Table 2.1. The pressure at failure and the corresponding tensile strength, for samples with an area of 1.96 and 4.875 mm^2, for both the solder compositions are listed in Table 5.1. As expected, samples with a bond area of 9.5 and 19.6 mm^2 did not show failure at the maximum applied pneumatic pressure of 1.6 MPa (235 psi). Three samples of each bond area and composition were tested. Since the pressure at which the failure occurred did not vary more than the minimum resolution [10 psi (68.9 kPa)] of the pressure regulator used for applying the pneumatic pressure, no spread in measurements was observed for the present set of samples.

Samples with 52%In-48%Sn as bonding layer not only show bonding at lower temperatures but also exhibit higher bond strengths. Also, the alloy has excellent low temperature malleability, which allows the intermediate layer to absorb any stress generated upon bonding of dissimilar substrates due to differences in the coefficients of thermal expansion. However, as is evident from Table 5.1, higher values of tensile strength were obtained for samples with lower bond area. This result is repeatable for both pure In and 52%In-48%Sn compositions. Since the thickness of the deposited film

was same for both of the bond areas, the total surface area of electroplated solder for the sample with wider line width is larger. Therefore, the amount of native oxide formed on the surface for the larger area sample is expected to be correspondingly higher. Since the breakdown of this oxide has been found to be critical for bond formation and since the oxide does not dissolve in molten solder, I believe that the presence of the larger amount of oxide causes formation of weaker bonds for the samples with larger line width. Also, samples with 100 μm line width have a surface area to volume ratio which is ~15% larger than sample with 250 μm line width. Hence the surface tension forces are more significant for samples with smaller line width (or area). Presence of higher forces due to surface tension is believed to result in enhanced breakdown of the oxide film thus promoting formation of stronger bonds. No experiments were conducted to verify these hypothesis and the causes for enhanced bond strength for lower bond area are currently under investigation.

5.1.1.2 Non-destructive Evaluation of Bond Uniformity

Acoustic imaging was used for the non-destructive study of the bond interface [2]. The process involves launching ultrasonic waves into the samples at a frequency of 230 MHz using a piezoelectric transducer. The same transducer also acts as a receiver of the reflected waves from the sample. Ultrasound waves get reflected when they encounter a material discontinuity and the reflection intensity at any pixel is represented as on a continuous black (0%) and white (100%) scale. Since the interpretation of gray scale pixels in acoustic imaging can be quite complex, we have limited our interpretation to the

simplest cases where white pixels represent voids and material discontinuity and black pixels represent area of material continuum. Figure **5.2** shows the acoustic image of the bond interface where uniform bonding with minimum void formation is observed for two bond areas. As the reflection intensity of the ultrasound waves is monitored through the bond interface, dark pixels signifying low reflection indicate good bond formation with a uniform material density through the bond.

5.1.1.3 Test for Hermetic Sealing

The bonds were tested for hermetic sealing capability using a commercial He-leak tester. The samples were fixed on a blank flange using high vacuum adhesive. The hole in the bottom substrate of the sample was aligned with the hole in the flange to make sure that correct test results are obtained, as shown in Fig. **5.3.** All the samples showed leak integrity of better than $1x10^{-11}$ mbar-l/s, even for samples having a line width of 100 μm.

The PZT is peeled off an actuator to check the bonding quality of the second fabricated devices. Figure **5.4** shows the top surface of the etched beam and the large rectangular bonding area. This excellent condition validates that the solder bonding is very reliable and well controlled.

5.2 Performance

5.2.1 Static Performance

5.2.1.1 Displacement

Figure 5.5 shows a white light interference microscope image of a fabricated flextensional device under 0 V and 100 V using the first technique, and Fig. 5.6 shows the deflection of the beam in detail. This fabrication does not provide good repeatability due to glue bonding and results in arbitrary initial shape. Since no two beams have the same initial shape, the evolution of the beam profile upon application of the voltage results in the maximum of deflection being at different locations along the beam. This made any direct comparisons and generalizations between devices very difficult. Typically, the beam was found to buckle upwards by 8.7 μm due to a PZT contraction of 0.276 μm, resulting in a gain factor (GF = 32.7) This exceeds the theoretically predicted value for a device of this size under sinusoidal initial shape [3]. It can only be concluded that this enhancement of the observed gain factor is due to the complex initial shape of the fabricated bridges.

The dimensions of the flextensional beams fabricated using the two methods described above are listed in Table 5.3. Figures 5.6, 5.7, and 5.8 show the deflection of the beam as a function of the applied electric field for the devices fabricated using the two fabrication techniques. In the case of adhesive bonding, the repeatability of the measurements is poor and results in arbitrary initial shape. In this technique since no two

beams have the same initial shape, the evolution of the beam profile upon application of the voltage results in the maximum of deflection being at different locations along the beam. This makes any direct comparisons and generalizations between devices very difficult. However, adhesive bonding of the silicon beam to the PZT at room temperature results in minimal residual stress in the beams. Thus when the PZT is cycled through the -100 - 0- +100V range, the -100-0V range resulting in a tensile stress within the beam shows no detectable deflection. This is to be expected since; a flat clamped-clamped beam under tensile stress will show no deflection. However, in the 0 - 100V region, the stress on the beam is compressive and thus results in the observed flextensional deflection characteristics.

Figure **5.9** shows the flexural behavior of the solder bonded actuator at -100V, 0V and 100V respectively. For the flextensional devices fabricated using solder bonding technique, the initial state has a larger imperfection than for the epoxy glue bonded actuators. This is due to the residual compressive stresses in the silicon beam arising from the mismatch in the thermal expansion coefficients of the PZT (1 ppm/K) and SOI wafers (2.6 ppm/K [4]). The compressive load $P_{Bonding}$ arising due to the bonding step in the silicon beam can be calculated as [5]:

$$
\begin{aligned}
&P_{Bonding} = Y_b\,\varepsilon\,(w_b t_b) \\
&\varepsilon = \frac{l_p(1+\alpha_b\Delta T)\alpha_b\Delta T - (l_p - l_b)(1+\alpha_b\Delta T)\alpha_b\Delta T - l_p(1+\alpha_b\Delta T)\alpha_p\Delta T}{l_b(1+\alpha_b\Delta T)(1-\alpha_p\Delta T)} \\
&\Delta T = T_{Bonding} - T_0 \\
&\therefore P_{Bonding} = \frac{l_b\alpha_b\Delta T - l_p\alpha_p\Delta T}{l_b(1-\alpha_p\Delta T)}
\end{aligned}
\qquad (5.2)
$$

where α_p and α_b are the thermal expansion coefficients of PZT and SOI beam respectively, Y_b (125GPa [6-8]) is the Young's modulus of the beam, $T_{Bonding}(200°C)$ is a bonding temperature, and $T_0(25°C)$ is the room temperature. If the obtained compressive load due to bonding $P_{Bonding}$ is larger than the critical load, $P_{Critical}$ given by

$$P_{Critical} = 4\pi^2\left(\frac{Y_b w_b t_b^{\,3}}{12 l_b^{\,2}}\right) \qquad (5.3)$$

for a beam with clamped-clamped boundary condition [5], the silicon beam either buckles up or down. The values of $P_{Bonding}$ and $P_{Critical}$ for the various actuators are listed in Table 5.3. For all the actuators the compressive load generated due to bonding process is greater than the critical load and thus all the fabricated actuators are buckled initially. Since the gap (~9 μm) between the beam and the PZT is typically smaller than the initial shape (12.6 μm), the beams most likely snap through and end up with an upward bending profile in all the samples tested. This imperfection is repeatable and always results in the beam being buckled-upwards (away) from the PZT surface. For Actuator 1, the initial midpoint deflection value is ~12.6 μm and the deflection changes with the application of the electric field. When +100 V is applied to the PZT, the midspan beam deflection is 15.8 μm. With -100 V the PZT is lengthened, and the beam deflection is 7.8 μm. The actuator stroke from -100 V to 100 V is around 8 μm, which is smaller than that of the previous actuator. This is due to a smaller d_{31} piezoelectric coefficient of the PZT used in this device. The high processing temperature necessitated the use of a lower d_{31} PZT which, however, had a higher Curie temperature. The gain factor was measured to be 20 for this device. All devices fabricated by either of the two techniques show high gain

factors. To check the repeatability of the devices fabricated using the second technique, the device static deflection was measured at three different times as a function of the applied voltage between -100 V and 100 V. These results are shown in Figs. **5.7** and **5.8**. The device shows good repeatability through several operational cycles with the exception of the hysteresis in each cycle. This hysteresis arises mainly from the PZT's characteristics [9] and was confirmed by measuring the PZT hysteresis curve using the Sawyer-Tower circuit in conjunction with a linear variable differential transducer and driven by a lock-in amplifier (Stanford Research Systems, Model SR830) while the PZT was immersed in Galden HT-200 to prevent arcing [10]. The larger initial imperfection of the devices fabricated using the solder bonding method results in the beam responding actively in both the negative and positive voltage (PZT strain) cycles and also results in more repeatable device characteristics.

Figure **5.10** compares the experimental and theoretical results for a 700 μm×200 μm×5 μm beam buckled by a 4.66 mm long PZT actuator. This device is initially deflected downward with a nonsinusoidal shape and nonzero slope at the boundaries. Due to device hysteresis form the PZT [9], the initial and final shapes (both at 0 V) are slightly different. The coefficients of the polynomial curve fits for these cases are averaged to provide the initial shape for the theoretical calculations. As the applied voltage increases, the beam buckles further downward and the shape becomes more sinusoidal. Figure **5.11** shows that the theoretical and experimental midspan displacements match fairly well over the entire range of applied voltage.

The decreasing voltage experimental data points almost exactly follow the theoretically predicted curve. The other theoretical solutions shown in Fig. **5.11** are not observed experimentally. At 100 V, the theoretically predicted beam shapes (Fig. **5.10** (b)) match both in shape and amplitude.

Figure **5.12** shows a beam with an initial quasi-sinusoidal shape with twice the spatial frequency. The hysteresis in this device is larger, producing the gap between the increasing (dashed) and decreasing (dotted) beam shapes. Again, the theoretical model initial shape is taken to be the average of the increasing and decreasing voltage shapes at V= 0V. Despite the lack of an obvious buckling direction based on the initial shape, the theory and experiment predict upward deflection. As the amplitude grows, the shape becomes smoother, losing its higher spatial frequency, and becoming more half-sinusoidal. The agreement between theoretical and experimental midspan displacement (See Fig. **5.13**) is not as close as the previous case. This is due to the larger hysteresis and also possibly the complicated initial shape.

The model is also verified with the advanced flextensional microactuator shown in Fig. **5.14** (See section **2.3** for fabrication). Due to large initial shape, the beam can be operated from negative (-100 V) to positive (100 V) voltages providing large stroke. Experimental midspan displacements agree with the theoretical results based on the shown initial profile in the plot at V= -100 V. The increasing voltage experimental data points accurately match the theoretically predicted curve.

5.2.1.2 Blocked Force

Figure 5.15 shows the actuation response when pushing against constraints at $a = 0.5$ with $k = 238.6$ [(a), (c), and (e)] and $k = 2386$ [(b), (d), and (f)]. The first row [Figs. 13 (a) and (b)] plots midspan displacement versus PZT contraction. Due to constraint stiffness, the buckling load increases and the bifurcation point moves to the left compared to Fig. 3.1 ($k = 0$). In Fig. 5.15 (b), for example, the constraint stiffness prevents displacement and shifts the buckling point to $u_L < -8.0 \times 10^{-4}$. Figure 5.15 (c) and (d) show that blocked force depends both on the constraint stiffness and the initial imperfection. With very small initial imperfection, the stiff spring constraint produces almost no force. Below the bifurcation point ($u_L < -4.0 \times 10^{-4}$), the soft spring produces force similar to the medium initial imperfection case. For the large initial imperfection, however, the stiff spring produces more blocked force. The deflected beam profiles show the rounding effect on the beam displacement caused by the stiff spring [Fig. 5.15 (f)]. With a smaller v_l, the actuation produces less force, and the bifurcation point moves to the left (See section B.2).

5.2.2 Dynamic Performance

5.2.2.1 Device Mounting

Figure 5.16 shows the experimental frequency response of the buckled beam and PZT with clamp and tape mountings. The PZT vibrates much less with the soft

conductive tape mounting. The spurious peaks in the beam response also disappear with tape mounting. Thus, the tape mounting is preferred for dynamic operation.

5.2.2.2 Frequency Response

Figures **5.17** and **5.18** show the experimental and theoretical frequency responses for Devices 3 and 2, respectively. The experimental frequency response curves are obtained by a 7.2 V sine sweep from 1 kHz to 1 MHz. In Fig. **5.17** (a) the theoretical and experimental curves show a large peak corresponding to the first mode. The other peaks in the experimental response correspond to the unmodeled dynamics of the silicon support structure. Laser vibrometer measurement of the support structure in Fig. **5.17** (b) shows these unmodeled modes. Fig. **5.18** shows the first two modes for Device 2 at $\omega = 46.2$ and $\omega = 63.1$, respectively. The height of the theoretical peaks are much greater than the experimental peaks. This may be due to underestimation of system damping or a relatively fast sine sweep through the resonances.

5.2.2.3 Modal Analysis

The experimental and theoretical natural frequencies are compared in Table **5.3**. The experimental ω_i are determined from the frequency response. The theoretical ω_i are calculated using the best-fit sinusoidal and polynomial initial shapes shown in Fig. **4.3**. Table **5.3** clearly shows that the polynomial initial shape more accurately predicts the

natural frequencies. For ω_1 and ω_2 of all three devices, the polynomial results are closer to the experimental results than the sinusoidal results. The closeness of fit (R^2) closely correlates with ω_i prediction accuracy. The second mode frequency is more sensitive to asymmetry, so despite the large change in R^2 from sinusoidal to polynomial cases in Device 3, the overall shape is fairly symmetric, and no change in ω_2 is calculated. There is no experimental 2nd resonance for Device 1 because the device was broken during data acquisition.

5.2.2.4 Step Response

Figure **5.19** compares the theoretical and experimental response to the 20 V "step" input shown in Fig. **5.19** (a). The $u_L(t)$ input shows slight overshoot due to the amplifier dynamics. The response amplitude agrees well for $a = 0.26$ and the squeeze film damping predicts the response decay time. Therefore, the overpredicted peaks in Fig. **5.17** (a) and Fig. **5.18** are mostly likely due to the relatively fast sweeps through resonances. The experimentally-observed beating phenomenon is due to the coupling between the silicon support structure and buckled beam modes.

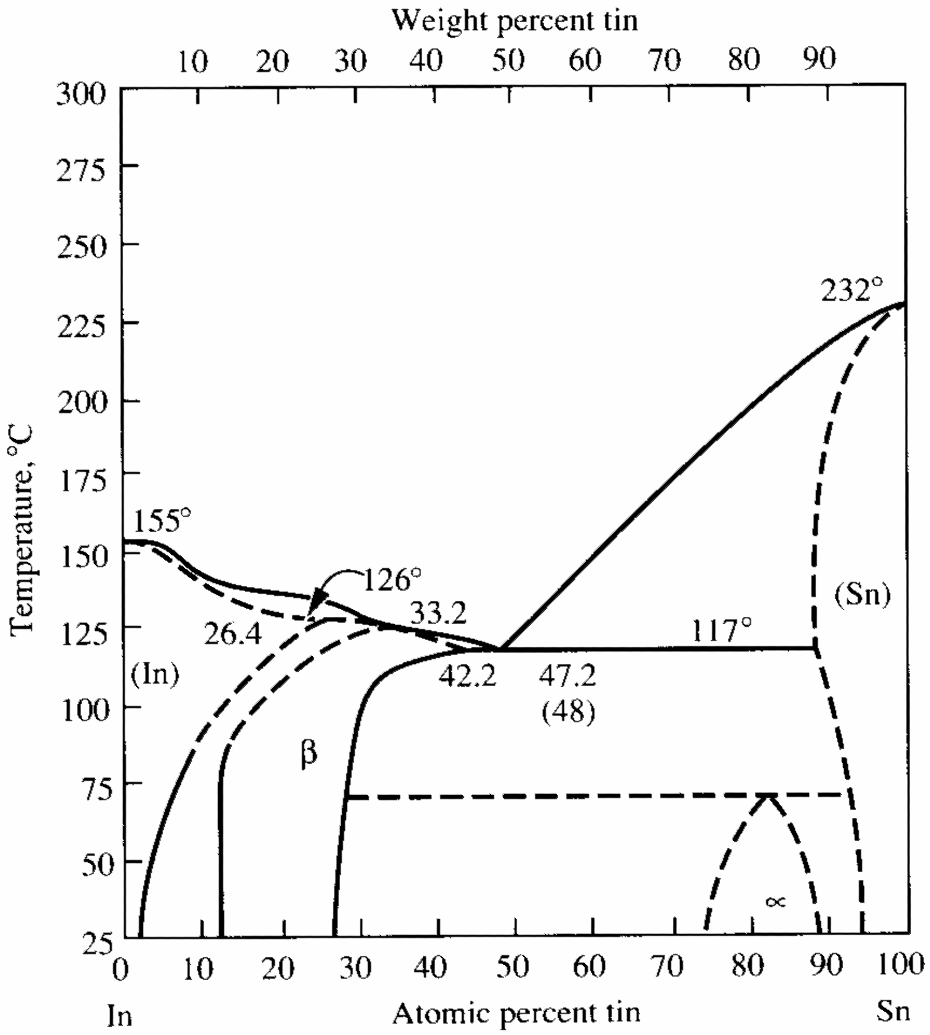

Fig. **5.1**: Phase diagram of Indium Tin [1].

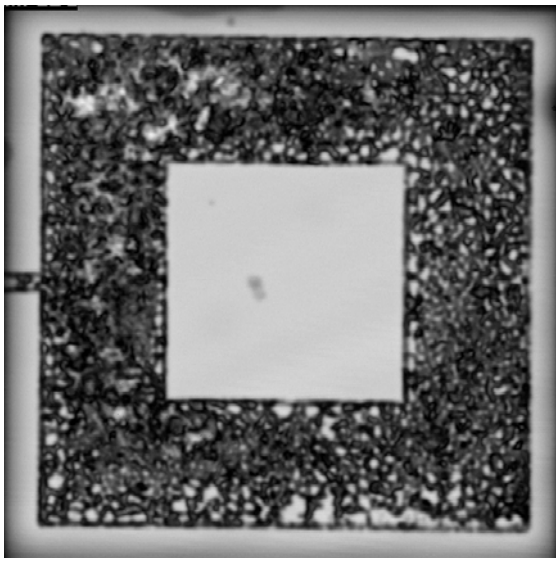

(a) 100%In as the bonding

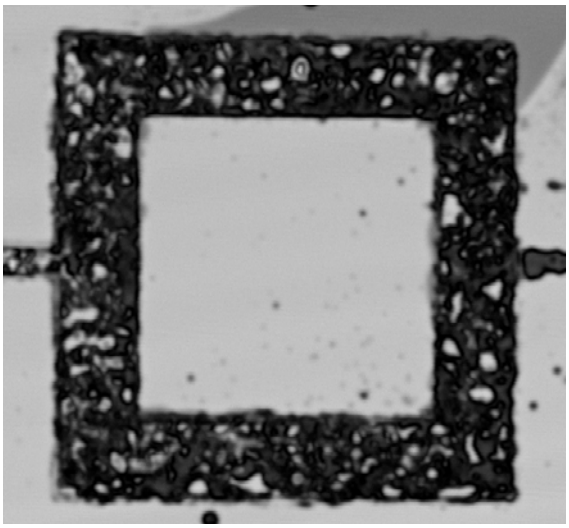

(b) 52%In-48%Sn as the bonding material

Fig. **5.2**: Acoustic image of the bond interface showing presence of uniform bonds with minimum voids.

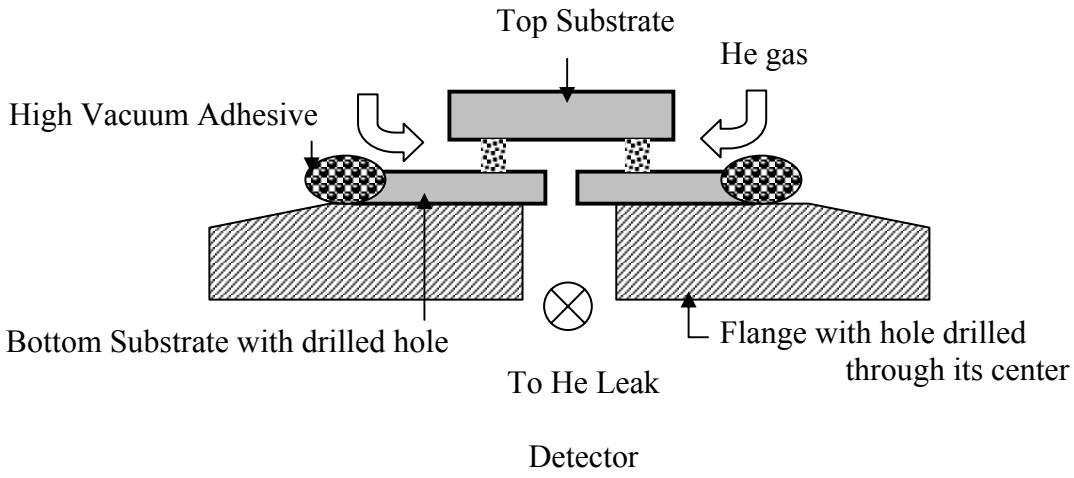

Fig. **5.3**: Set up for evaluation of bonds for hermetic sealing capability.

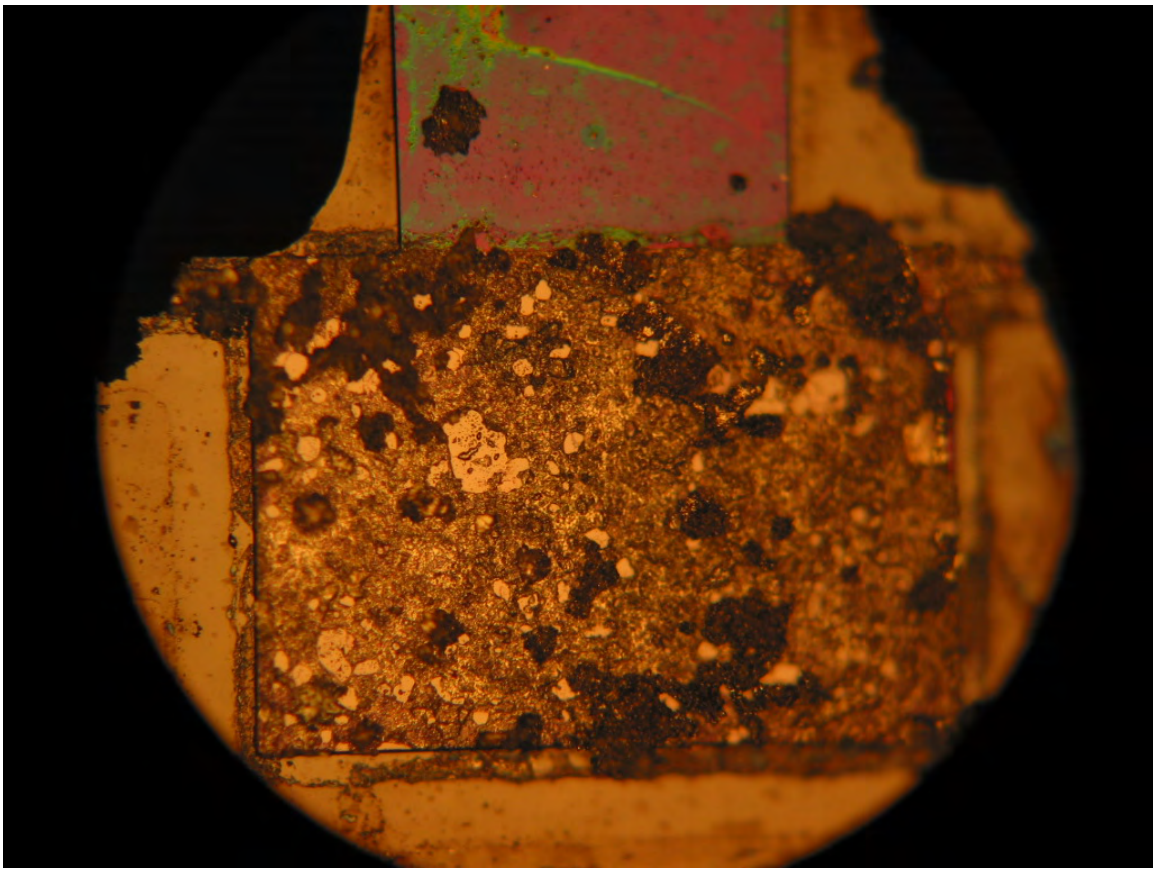

Fig. 5.4: Optical picture of the In/Sn bond area after peeling off the silicon beam from the PZT shows good bonding uniformity and pattern definition.

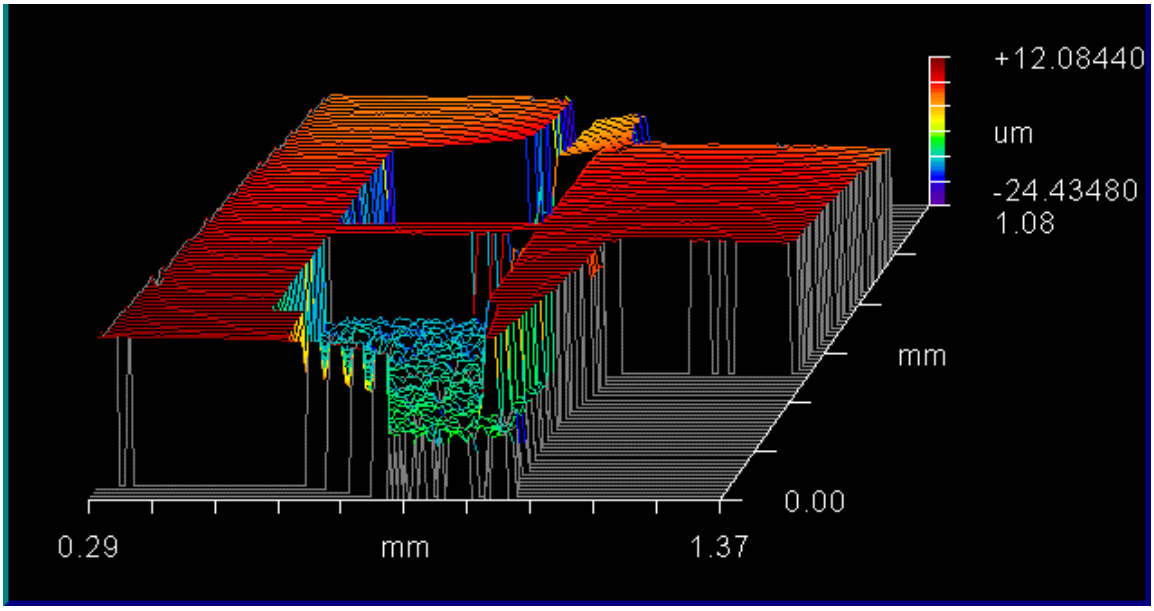

(a)

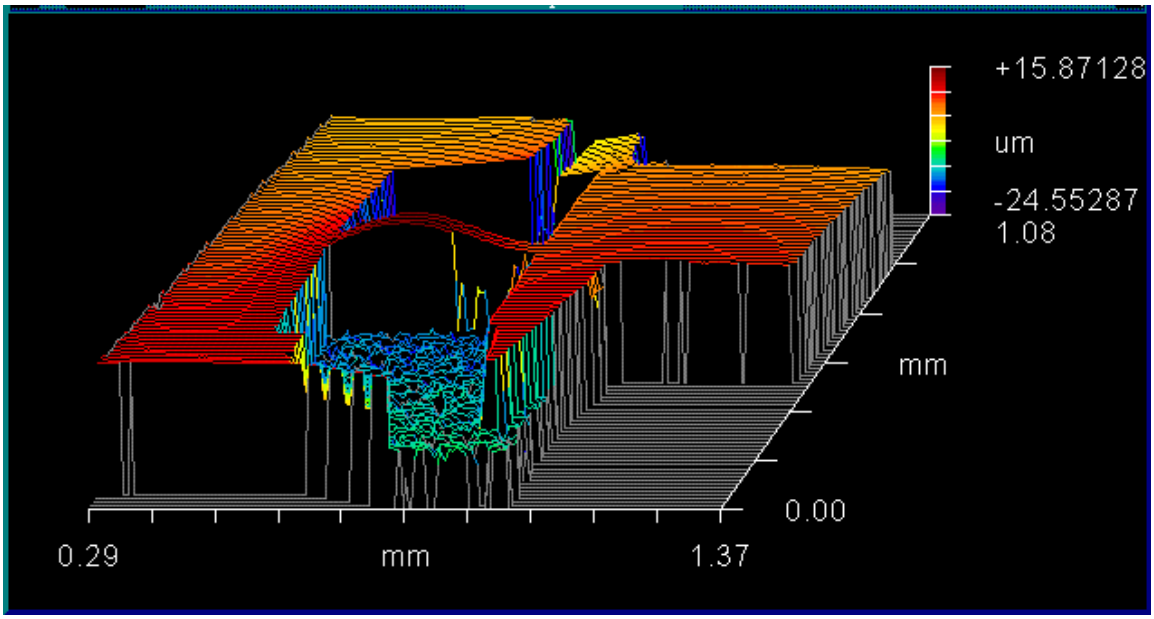

(b)

Fig. **5.5**: White interference microscope topographic projection of a 350 µm×50 µm×5 µm beam from the first technique at 0 V (a) and buckling upward under 100 V (b).

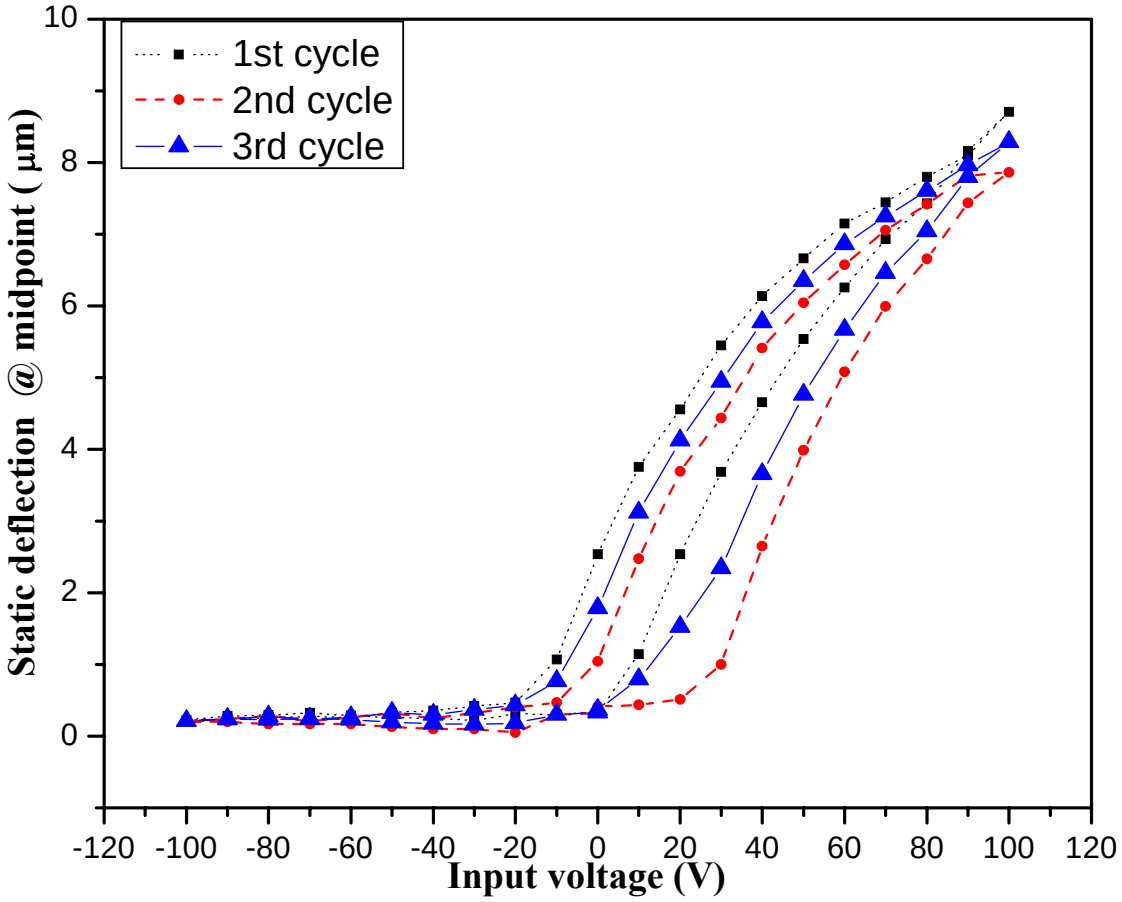

Fig. **5.6**: Static deflection measurement of the beam fabricated using adhesive bonding at the midpoint as a function of the PZT voltage for a 350 μm × 50 μm × 5 μm buckled by a 4.66 mm long PZT.

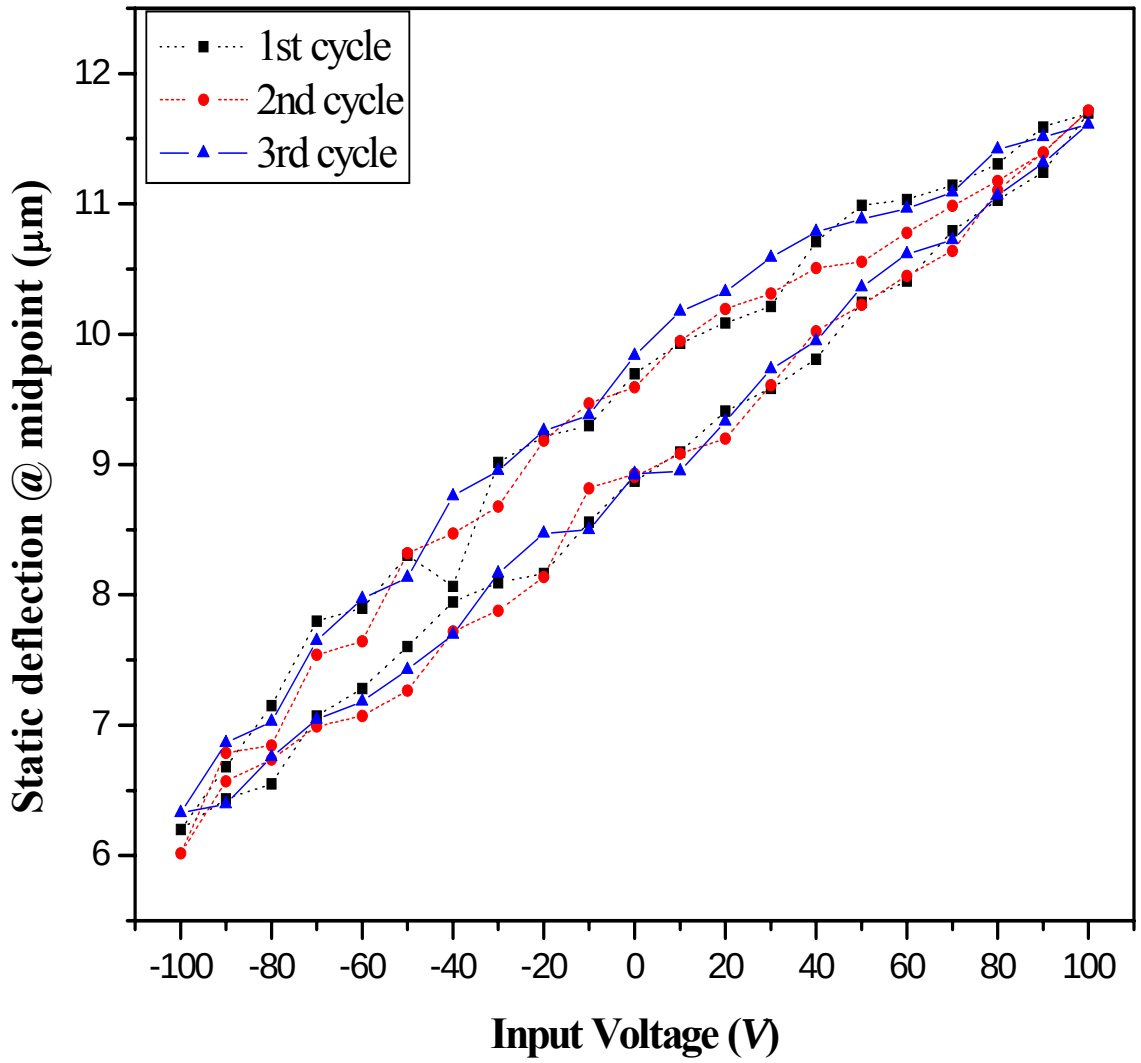

Fig. **5.7**: Static deflection measurement of the beam fabricated using solder bonding techniqe as a function of the PZT voltage for a 350 μm×50 μm×6 μm beam buckled by a 4.5 mm long PZT actuator.

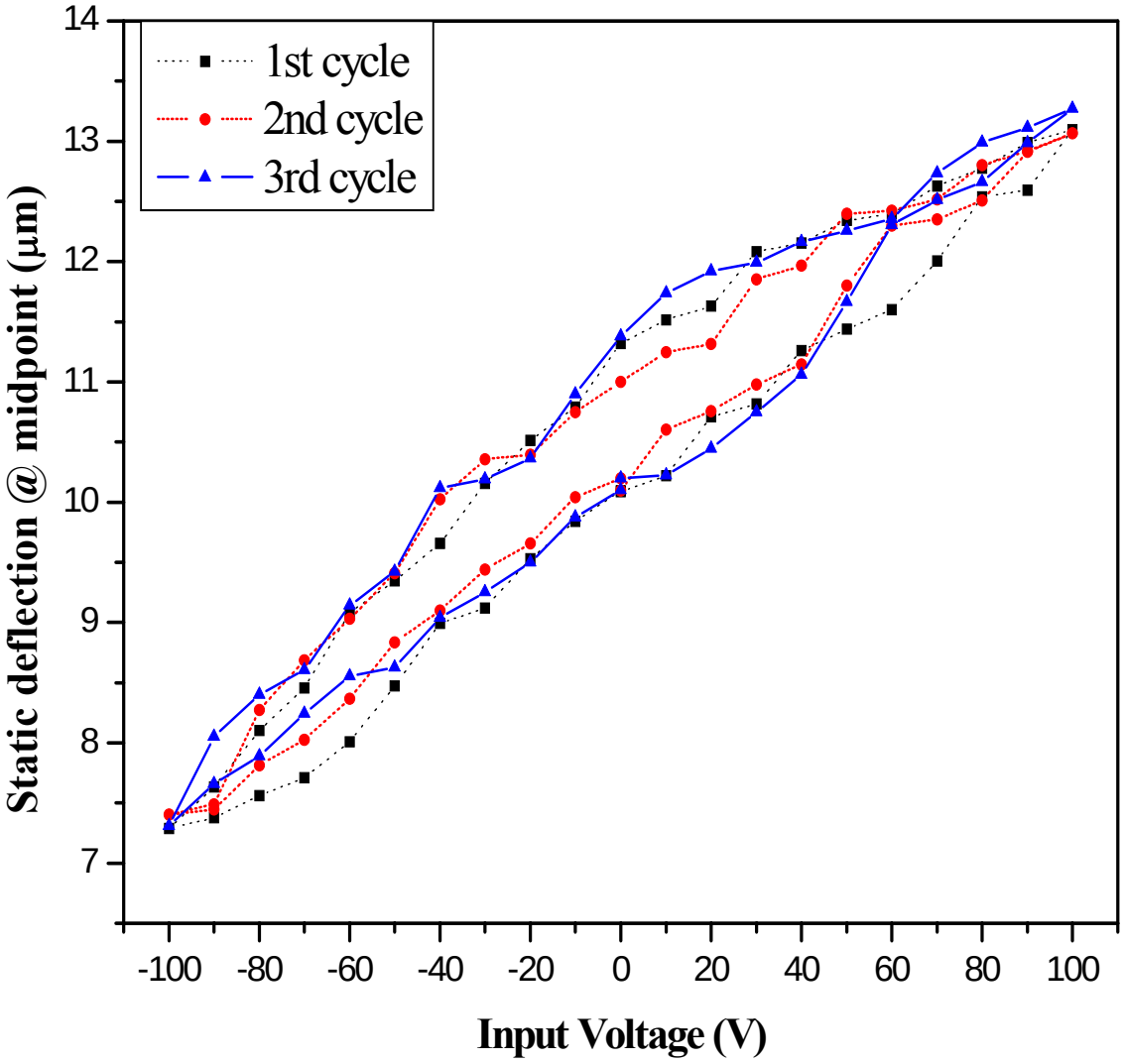

Fig. **5.8**: Static deflection measurement of the beam fabricated using solder bonding techniqe as a function of the PZT voltage for a 550 μm×100 μm×6 μm beam buckled by a 6.5 mm long PZT actuator.

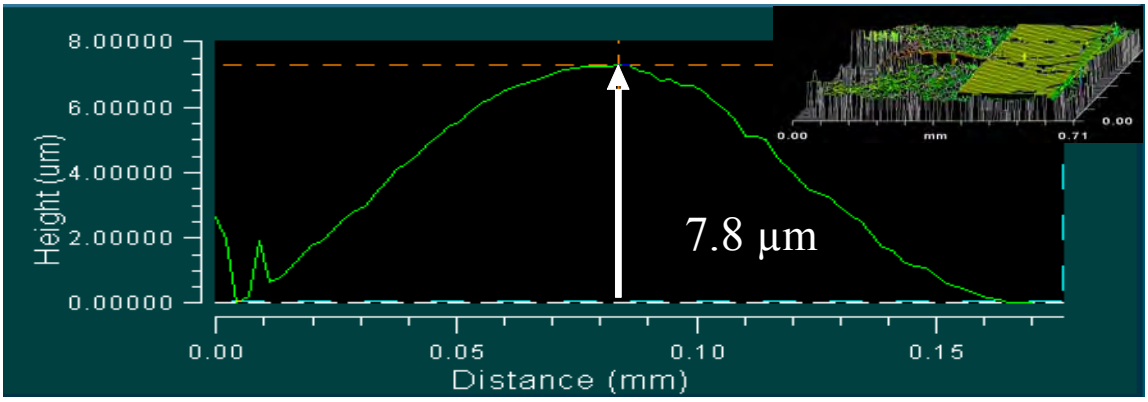

@-100 V

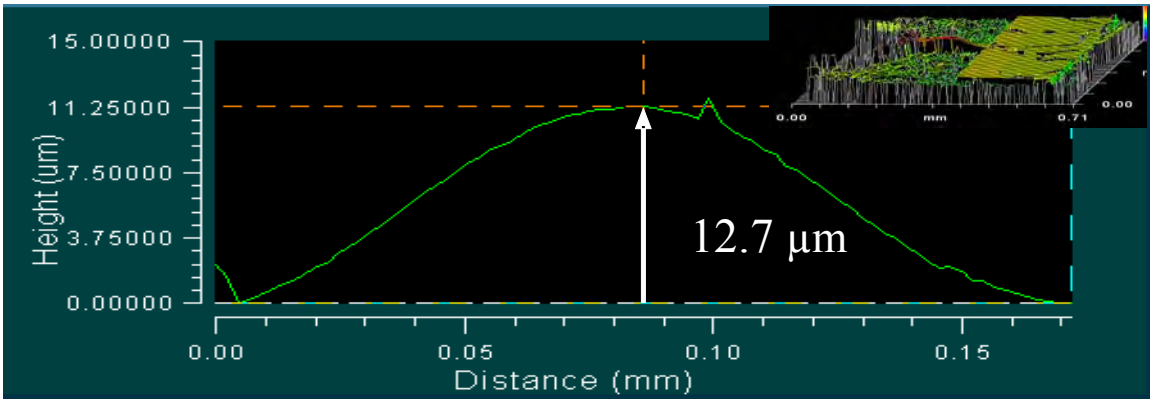

@ 0 V

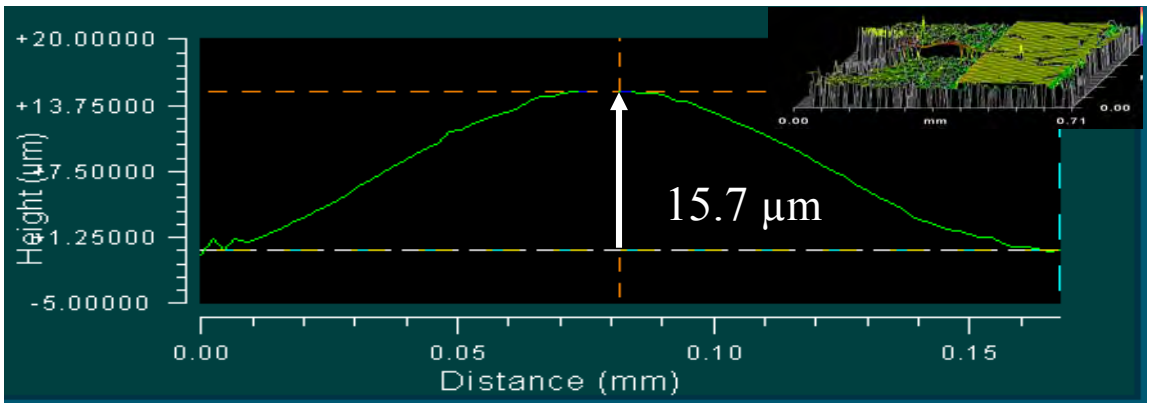

@100 V

Fig. **5.9**: White light interference microscope generated 2-D profiles of the static deflections of the flextensional beam fabricated using solder bonding technique of Device 2.

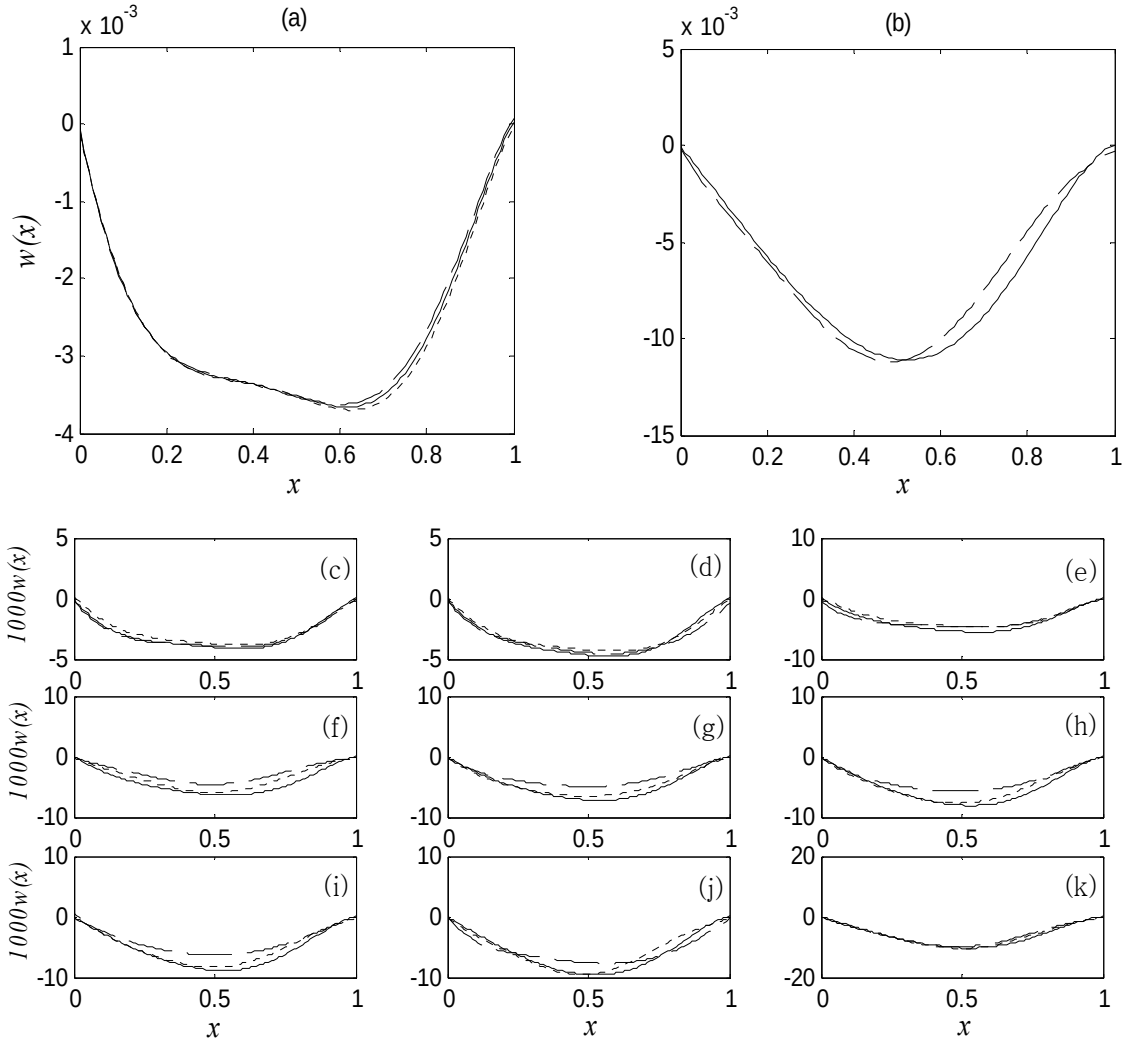

Fig. **5.10**: Theoretical (solid) and experimental [increasing (dashed) and decreasing (dotted) voltage] results for a 700 μm×200 μm×5 μm beam buckled by a 4.66 mm long PZT actuator: (a) Initial shape (0 V); (b) Maximum deflection (100 V); (c) – (k) Intermediate (10 V – 90 V).

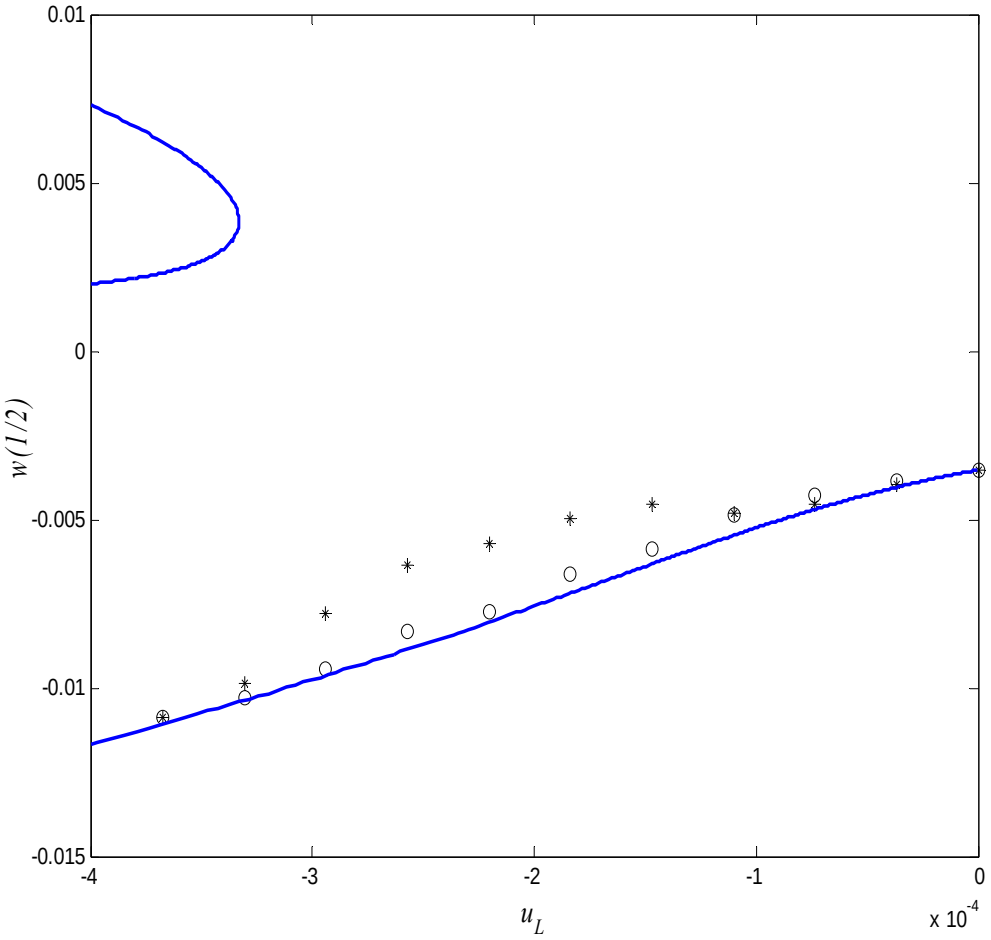

Fig. **5.11**: Theoretical (solid) and experimental [increasing (*) and decreasing (o) voltage] midspan displacement for a 700 μm×200 μm×5 μm beam buckled by a 4.66 mm long PZT actuator.

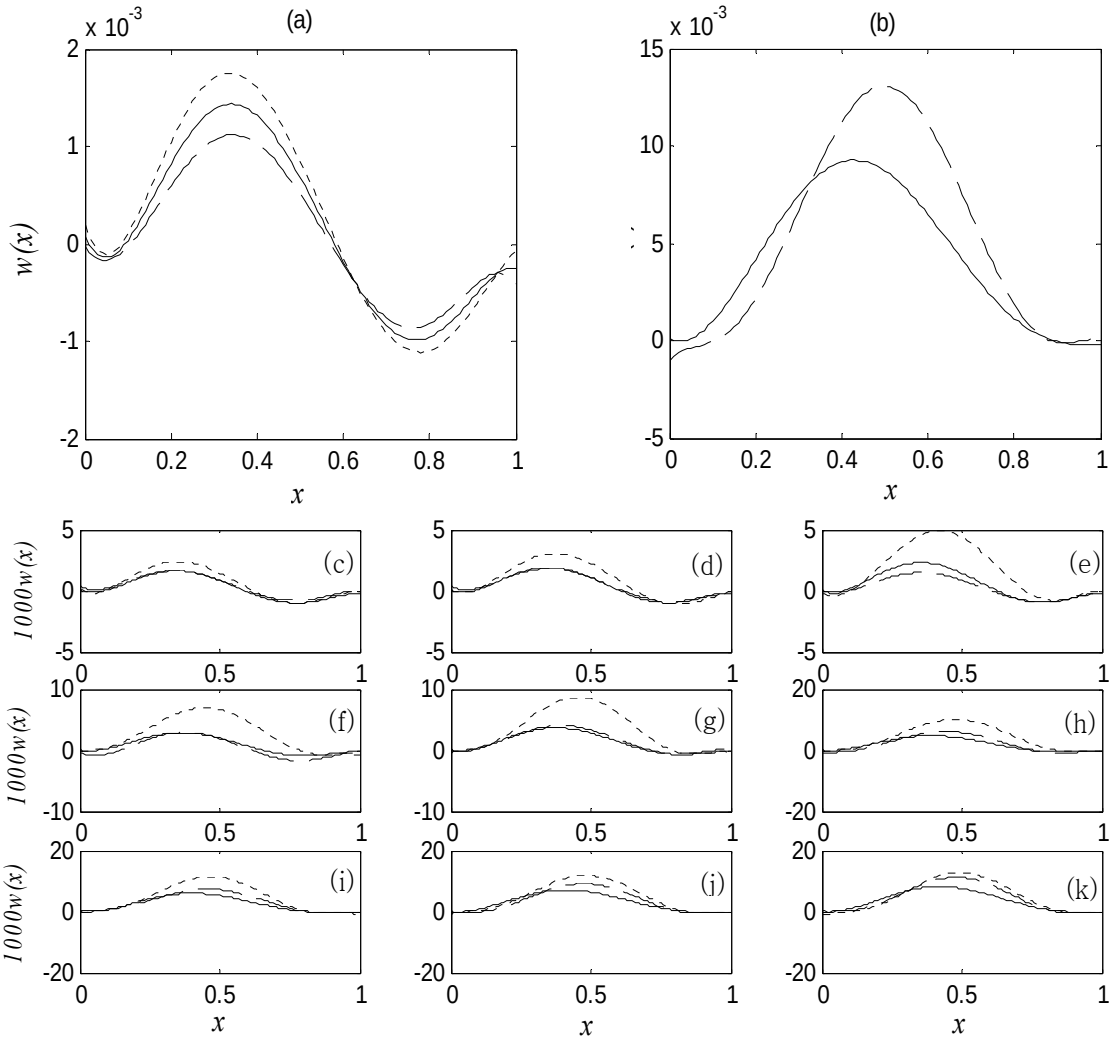

Fig. **5.12**: Theoretical (solid) and experimental [increasing (dashed) and decreasing (dotted) voltage] results for a 520 μm×50 μm×5 μm beam buckled by a 4.66 mm long PZT actuator: (a) Initial shape (0 V); (b) Maximum deflection (100 V); (c) – (k) Intermediate (10 V – 90 V).

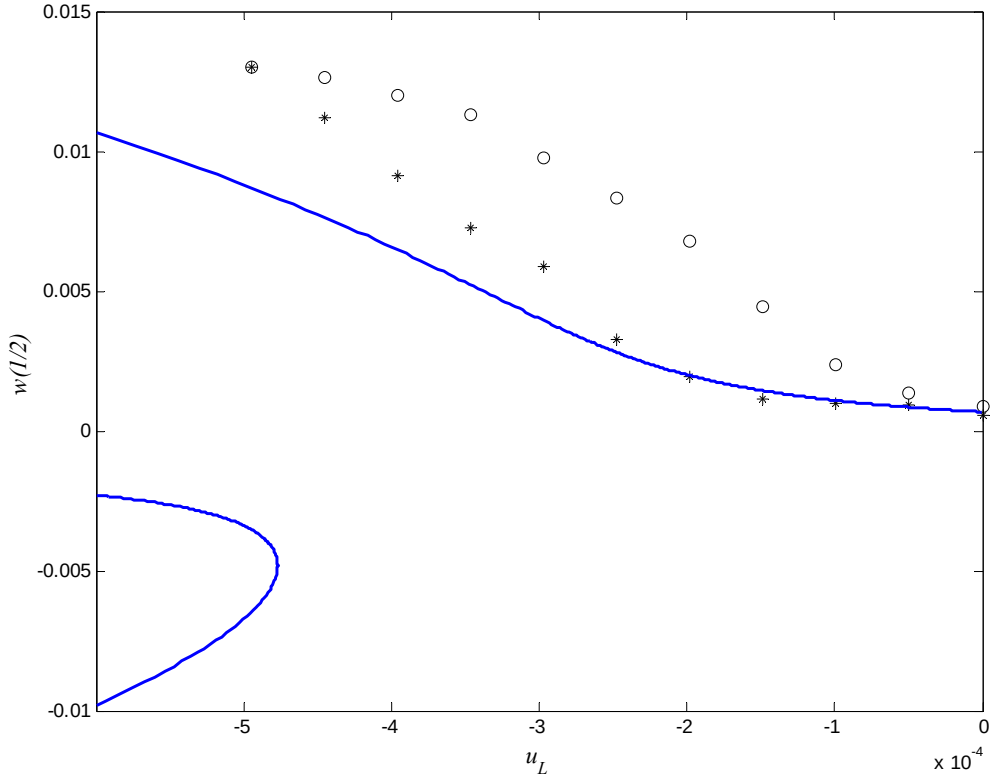

Fig. **5.13**: Theoretical (solid) and experimental [increasing (*) and decreasing (o) voltage] midspan displacement for a 520 μm×200 μm×5 μm beam buckled by a 4.66 mm long PZT actuator.

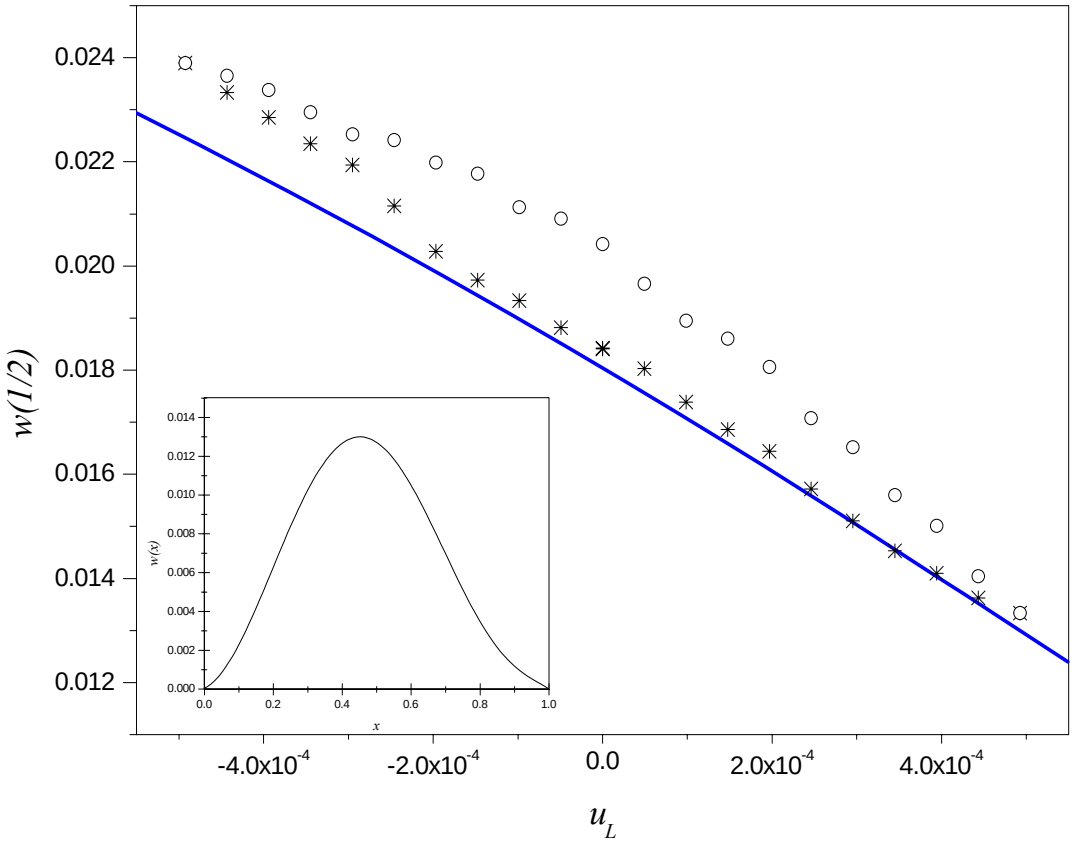

Fig. **5.14**: Theoretical (solid) and experimental [increasing (*) and decreasing (o) voltage] midspan displacement for a 550 μm×100 μm×6 μm beam buckled by a 6.5 mm long PZT actuator (Inset plot shows initial shape at $u_L = 4.9242e-4$).

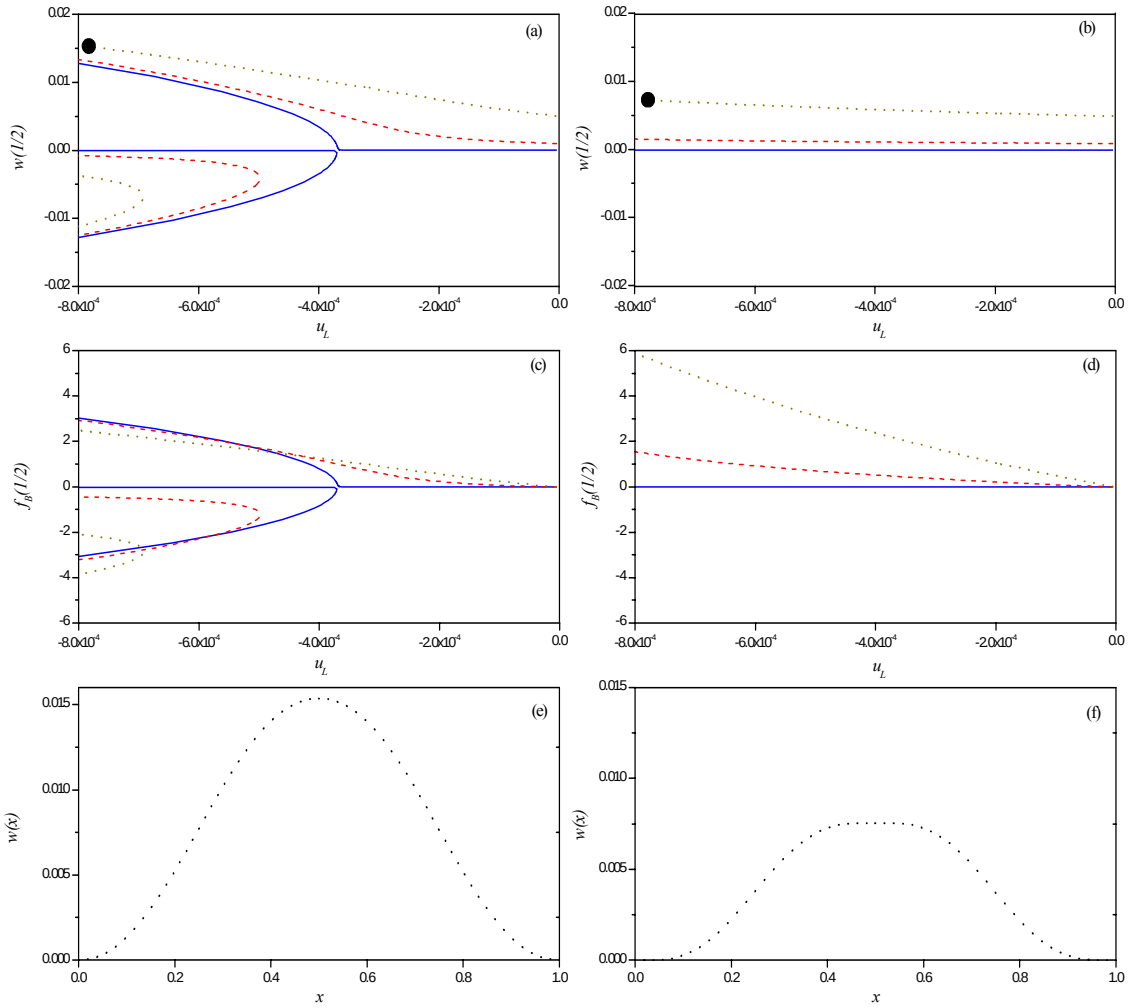

Fig. **5.15**: Theoretical blocked force [$a = 0.5$, v_l = 485, g = 1e-6 (solid), 1e-3 (dashed), and 5e-3 (dotted)]: (a) Midspan deflection versus PZT contraction ($k = 238.6$), (b) Midspan deflection versus PZT contraction ($k = 2386$), (c) Blocked force versus PZT contraction ($k = 238.6$), (d) Blocked force versus PZT contraction ($k = 2386$), (e) Deflected beam profile ($k = 238.6$) corresponding to (●) in (a), and (f) Deflected beam profile ($k = 2386$) corresponding to (●) in (b).

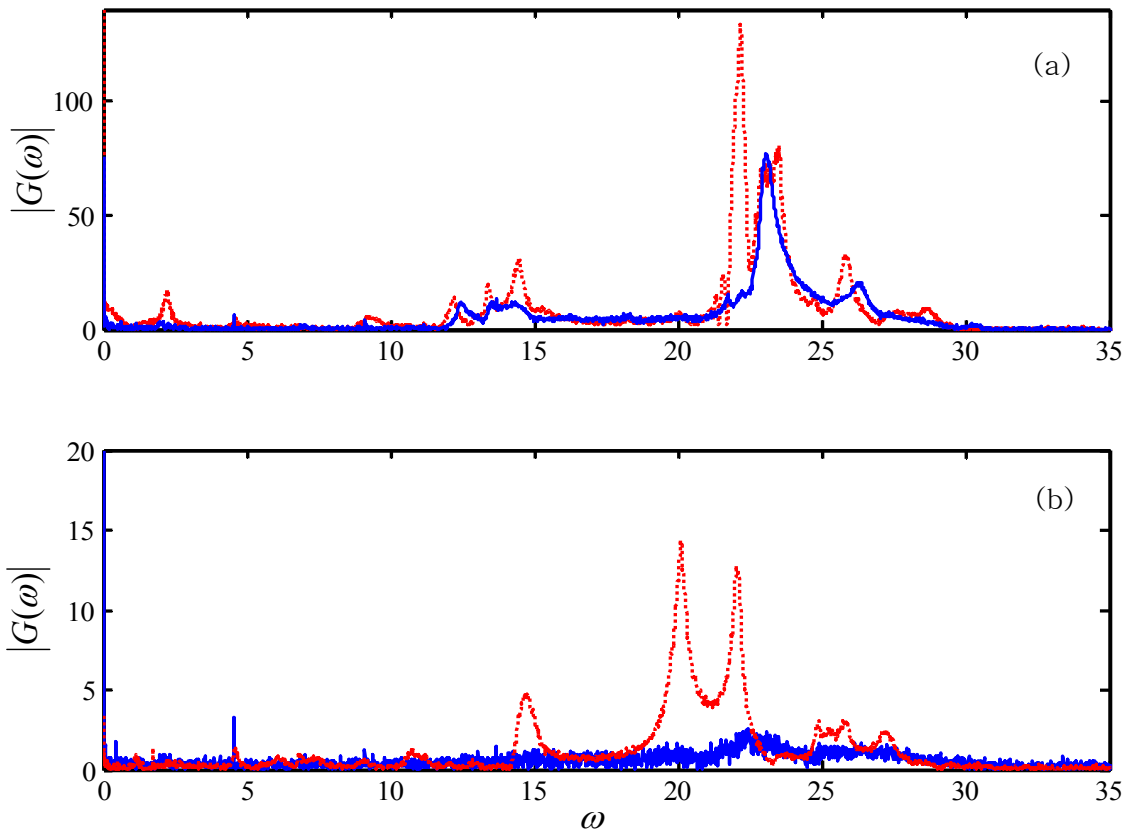

Fig. **5.16**: Frequency response function of Device 3 [clamped (---) and taped (—)]: (a) buckled beam and (b) PZT.

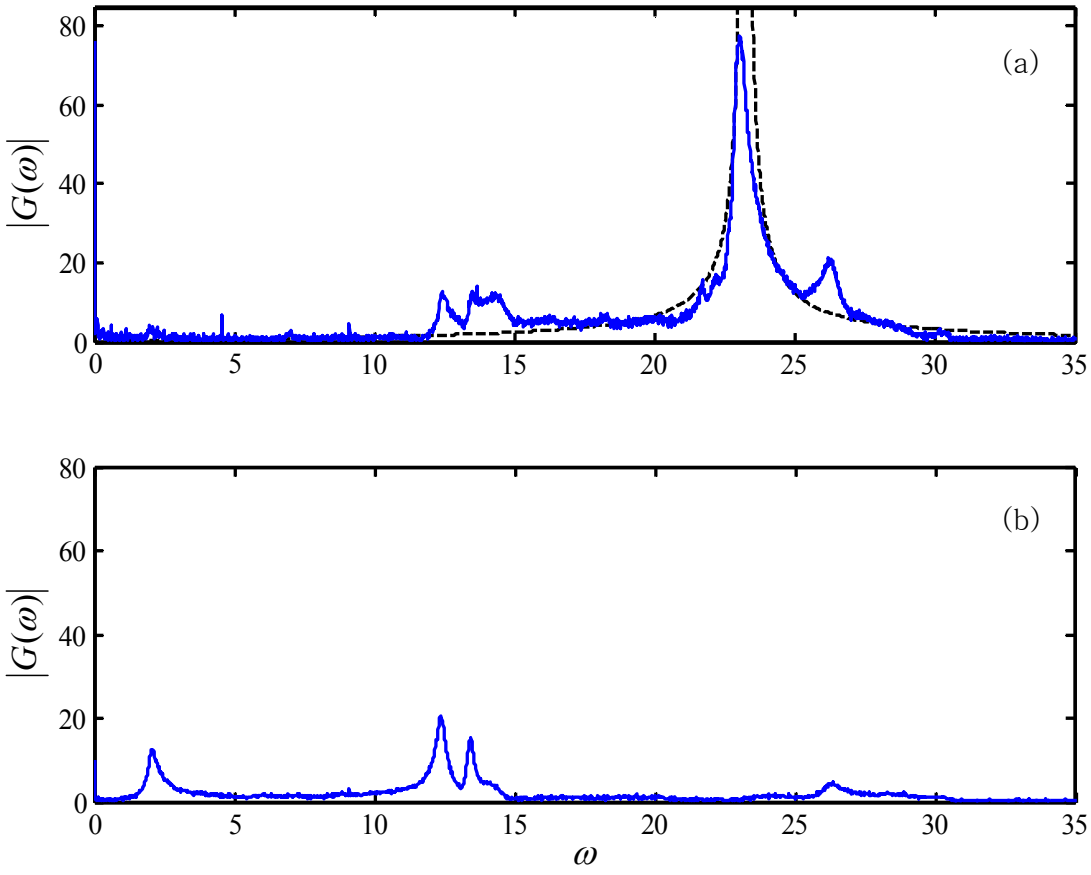

Fig. **5.17**: Frequency response function of Device 3 [Theory (---) and Experiment (—)]: (a) buckled beam (at $a = 0.1$) and (b) support structure.

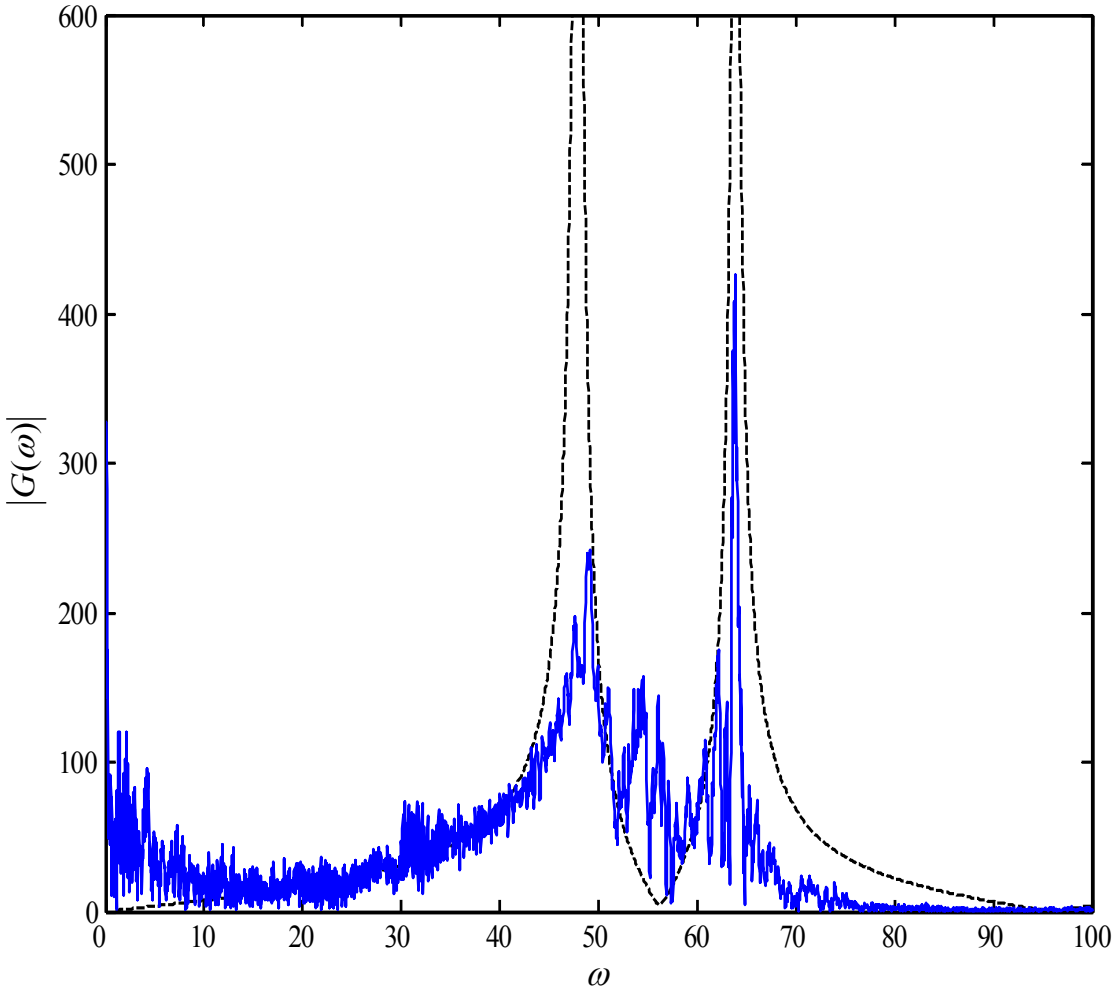

Fig. **5.18**: Frequency response function of Device 2 [Theory (---) and Experiment (—)] (at $a = 0.4$).

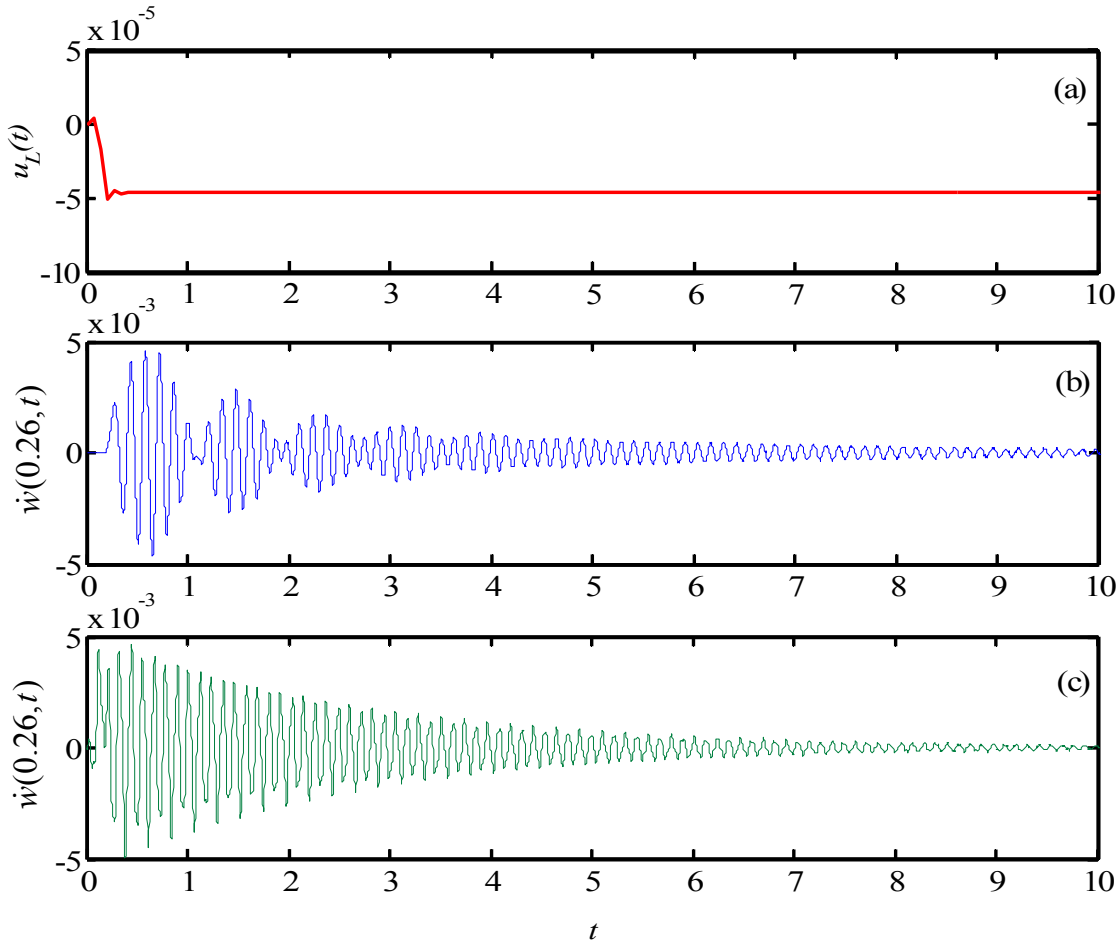

Fig. **5.19**: Step response of Device 2: (a) step input, (b) experimental velocity, and (c) theoretical velocity at ($a = 0.26$).

Table 5.1: Breakdown pressure for bonds and the corresponding tensile strength.

Sample Area (mm^2)	Bond Failure Pressure (MPa)		Tensile Strength of the Bond (MPa)	
	Indium	52%In -48%Sn	Indium	52%In -48%Sn
1.96	0.59	0.69	6.94	8.11
4.875	0.86	1.52	3.8	6.656

Table 5.2: Physical and Piezoelectric Properties (from APC).

Material:	850 (2^{nd})	855 (1^{st})
Relative Dielectric Constant		
K^T	1750	3300
Dielectric Dissipation Factor		
tan δ	1.4	1.3
Curie Point (°C)**		
T_c	360	250
Electromechanical Coupling Factor (%)		
k_p	0.63	0.68
k_{33}	0.72	0.76
k_{31}	0.36	0.40
k_{15}	0.68	0.66
Piezoelectric Charge Constant (10^{-12} C/N or 10^{-12} m/V)		
d_{33}	400	630
$-d_{31}$	175	276
d_{15}	590	720
Piezoelectric Voltage Constant (10^{-3} Vm/N or 10^{-3} m^2/C)		
g_{33}	26	21.0
$-g_{31}$	12.4	9.0
g_{15}	36	27
Young's Modulus (10^{10} N/m^2)		
Y^E_{11}	6.3	5.9
Y^E_{33}	5.4	5.1
Frequency Constants (Hz*m or m/s)		
N_L (longitudinal)	1500	1390
N_T (thickness)	2032	2079
N_P (planar)	1980	1920
Density (g/cm^3)		
ρ	7.7	7.7
Mechanical Quality Factor		
Q_m	80	65

Table 5.3: Parameters, dimensions, initial imperfection, discrepancy between sinusoidal and polynomial profile, and natural frequencies of three devices.

	Device 1		**Device 2**		**Device 3**	
System parameters						
v_l^2	67500		120000		53333	
c	0.228		0.337		0.225	
l_b (μm)	450		600		400	
w_b (μm)	100		100		50	
t_b (μm)	6		6		6	
$P_{Bonding}$ (N)	0.059		0.053		0.09	
$P_{Critical}$ (N)	0.025		0.036		0.044	
$W_{0Max.}$ (μm)	10.1		12.7		1.644	
$w_{0Max.}$	0.02245		0.02118		0.00456	
Results						
Modeling	$w_{0,s}$	$w_{0,p}$	$w_{0,s}$	$w_{0,p}$	$w_{0,s}$	$w_{0,p}$
R^2	0.918	0.999	0.948	0.998	0.899	0.988
Ω_1 (kHz)	457.8	405.2	297.3	252.3	292.5	287.8
ω_1	47.2	41.7	54.5	46.2	23.8	23.4
Ω_2 (kHz)	598.5	664.7	336.6	346.7	757.4	757.5
ω_2	61.7	68.5	61.7	63.1	61.7	61.7
Experiment						
Ω_1 (kHz)	366		269		267	
ω_1	40.3		49.3		21.7	
Ω_2 (kHz)	N.A.		356		778	
ω_2			64.8		63.4	

References

1. Seraphim, D.P., R. Lasky, and C.Y. Li, *Principles of Electronic Packaging*. 1989: Mcgraw Hill.

2. Akhnak, M., et al., *Development of a Segmented Annular Array Transducer for Acoustic Imaging.* Ndt & E International, 2002. 35(7): p. 427-431.

3. Cheong, J., S. Tadigadapa, and C. Rahn. *Piezoelectric Micro-flextensional Actuator*. in *Proceedings of the SPIE - The International Society for Optical Engineering*. 2004. San Jose, CA.

4. Kovacs, G.T.A., *Micromachined Transducers-Sourcebook*. 1998: Mcgraw Hill.

5. Crandall, S.H., N.C. Dahl, and T.J. Lardner, *An Introduction to the Mechanics of Solids*. Second ed. Engineering Mechanics Series. 1978: Mcgraw-hill International Editions.

6. Petersen, K.E., *Electron Devices ED-25.* IEEE Trans., 1978: p. 1241.

7. Roark, R.J. and W.C. Young, *Formulas for Stress and Strain*. 6th ed. 1989, New York: Mcgraw-hill.

8. Riethműller, W. and W. Benecke, *Thermally Excited Sillicon Microactuators.* IEEE Transactions on Electron Devices, 1988. 35(6): p. 758-763.

9. Uchino, K., *Piezoelectric Actuators and Ultrasonic Motors*. Electronic materials: Science and Technology, ed. H.L. Tuller. 1997: Kluwer Academic Publishers.

10. Yu, H., et al., *Domain Switching and Electromechanical Properties of Pulse Poled $Pb.Zn_1O_3Nb_2O_3.O_3.PbTiO_3$ Crystals.* Journal of Applied Physics, 2001. 89(1): p. 561-567.

Chapter 6

Summary and Future Work

In this thesis, a flextensional microactuator using bulk PZT substrate and bonded to a micromachined silicon beam structure is designed, fabricated, modeled, and tested. A high alignment precision, high strength, and low temperature In/Sn solder bonding process has been used to realize the flextensional microactuator. This research shows that a flextensional microactuator design consisting of a bulk PZT bonded to a micromachined silicon beam can produce large transverse displacement from small longitudinal input. Static deflection measurements on the actuator show a flextensional actuation gain factor of ~20 for these devices. The fabrication process produces functional devices with variable initial imperfection. For maximal actuator displacement and gain factor, the theoretical model recommends a thin beam structure and initial imperfection tuned to the maximum contraction provided by the PZT. For large PZT displacement, a perfect beam provides maximum gain factor but some imperfection is required to guarantee actuator movement in the desired (up or down) direction. For small PZT displacement, more initial imperfection improves performance. The theoretical model for general initial shape predicts direction and magnitude of beam displacement based on the initial shape. The theory more accurately predicts the response of beams with simple initial shapes. Experimentally observed hysteresis may be due to the PZT actuator or higher order buckling not predicted by the theory. Actuators with large initial imperfection generally produce larger blocked forces. Actuators with small initial

imperfection produce larger blocked forces against a softer constraint. With high k or small v_l, the buckling PZT contraction is larger.

Also, this thesis theoretically and experimentally investigates the dynamic response of a piezoelectric flextensional microactuator. When compared to sinusoidal initial beam shapes used by previous researchers, polynomial initial beam shapes enable more accurate prediction of beam natural frequencies, frequency response, and time response when compared to experimental results. The inclusion of squeeze film damping between the beam and PZT support enables the model to predict response times. Experiments show that mounting the PZT with soft carbon tape limits PZT vibration.

As a result of implementing In/Sn solder bonding based fabrication, improved repeatability, reliability, and yield was achieved in comparison to the initial fabrication process based upon adhesive bonding. The low temperature bonding process described here can be used for the heterogeneous integration of various materials for MEMS fabrication as well as for their packaging.

The following topics can be considered for future work.

- ✓ Making and testing new prototypical devices according to the applications, for example, as a switch, GLV, or mirror.
- ✓ Scaling down the dimensions of the actuator for much compacter devices, especially, the length of the PZT including decreasing the thickness of a SOI wafer to measure a blocked force. In the current study, the support structure prevented a nano indenter from contacting the buckled beam because the tip bumped into the support structure before contacting the buckled beam. However, the support structure thickness should be increased to ensure a clamped boundary

condition. The length of the buckled beam could be enlarged, but we also need to consider a slow dynamic response due to that effect.

- ✓ Decreasing the bonding temperature of In/Sn solder bonding to use the PZT with larger d_{31} coefficients. (This is also a parameter to make an actuator much more compact.)

Appendix A

Design and Fabrication

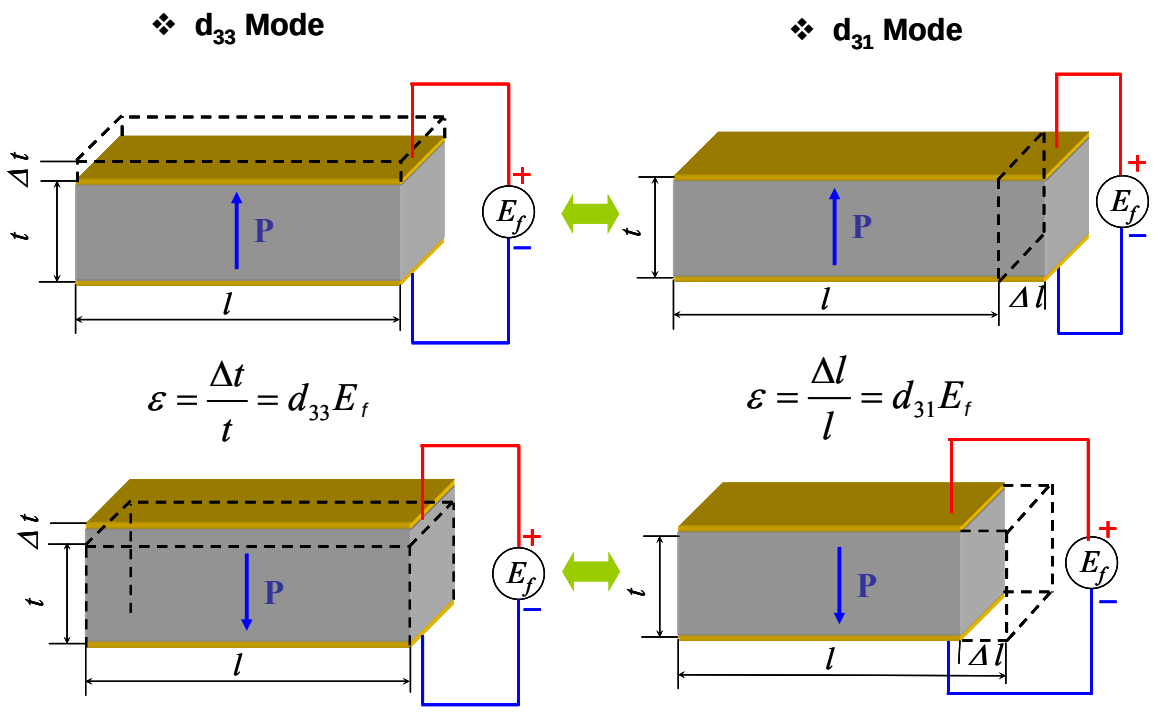

Fig. **A.1**: Characteristics of PZT.

Figure **A.1** shows general motion of the PZT. These two modes are dependent each other. In this research, d_{31} mode is used as an input source. If the applied electric field is same direction as the poling, the PZT is extended as the top figure. Otherwise, it is contracted like a bottom figure [1].

A.1 First Fabrication

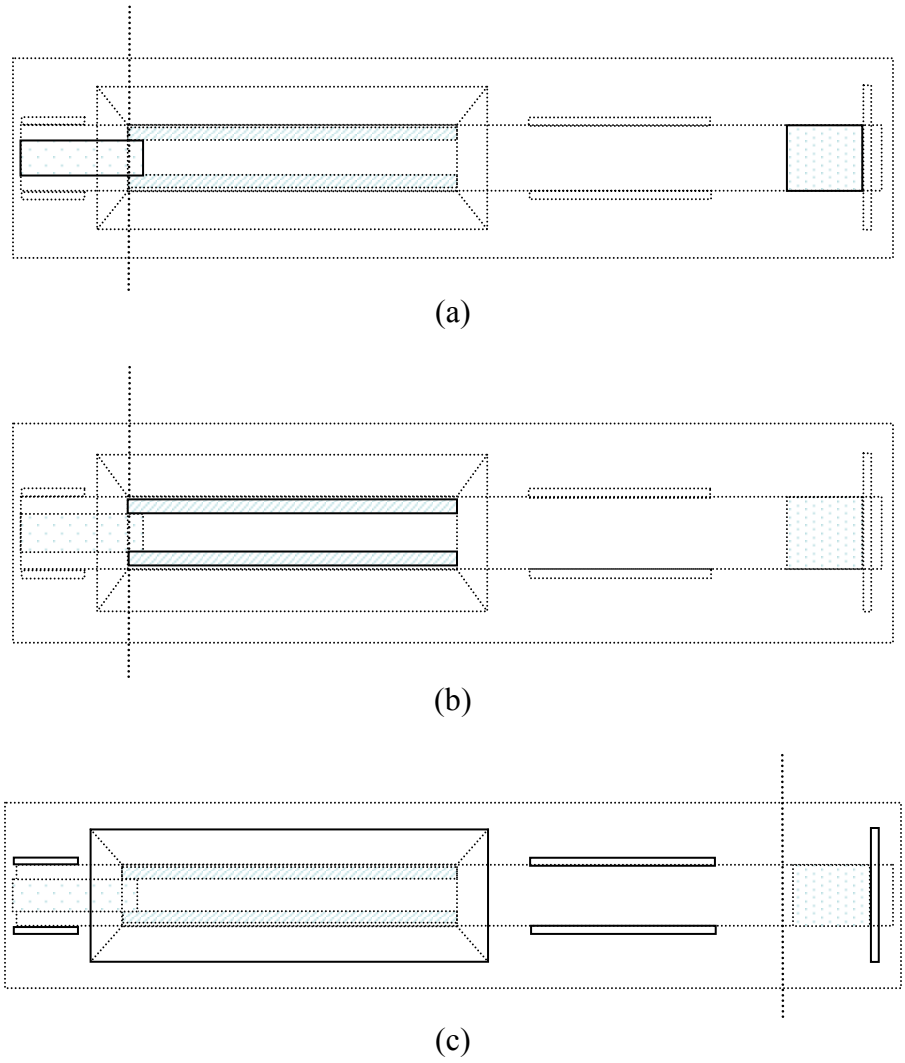

Fig. A.2: Mask layers for the first fabrication (Not to Scale): (a) for electrode and bonding, (b) for RIE etching, and (c) for EDP.

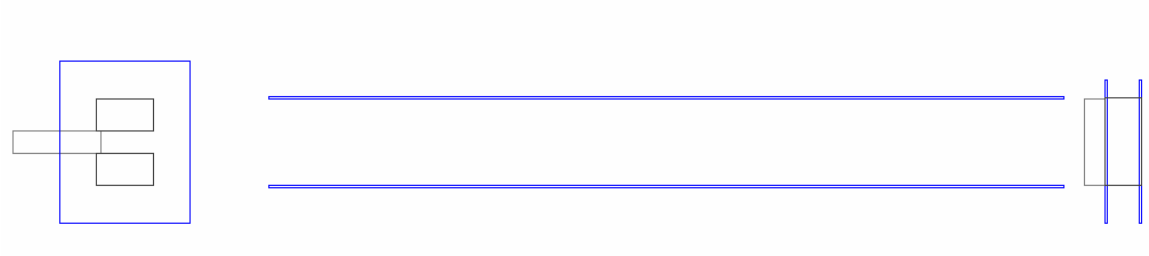

Fig. **A.3**: Total layout for the first fabrication using commercial program (To Scale).

1. Double side Polished Si Wafer

2. 5 μm deep boron doping

3. Thermal Oxidation (0.65 μm)

4. Thermal Anneal (1100°C for 30 min)

5. Strip oxide on top of the wafer

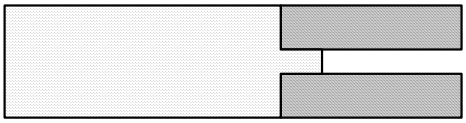

6. Lithography for bridge definition

7. RIE to define the bridge

8. Pattern and etch bottom oxide

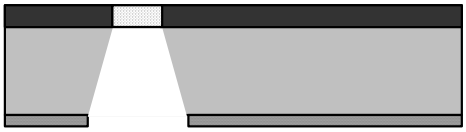

9. Selective Etching of Undoped-Si in EDP

Top view & bottom view after EDP etching

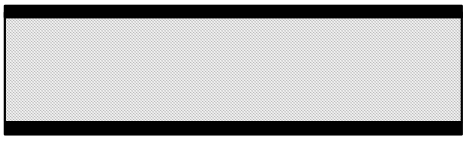

10. Deposit Cr/Au on PZT

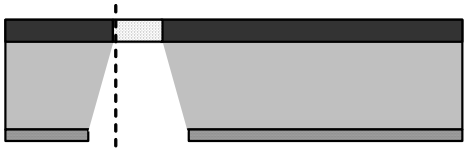

11. Dice left side to form a beam

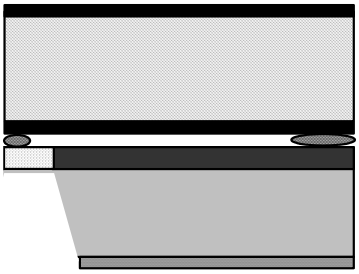

12. Bond PZT on top of etched Si

Fig. **A.4**: Schematic illustration of the first fabrication process.

A.2 Second Fabrication

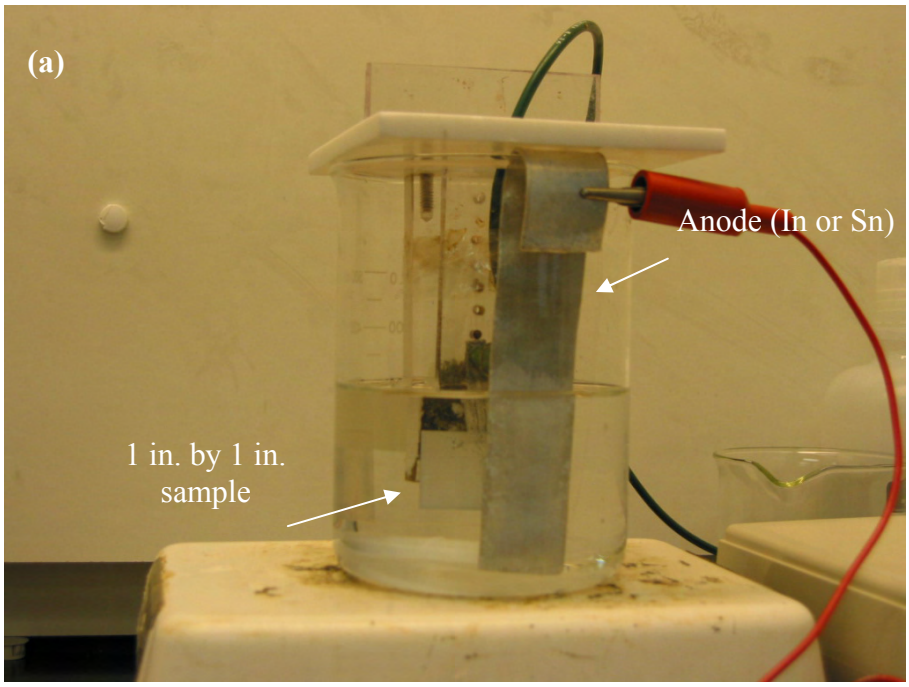

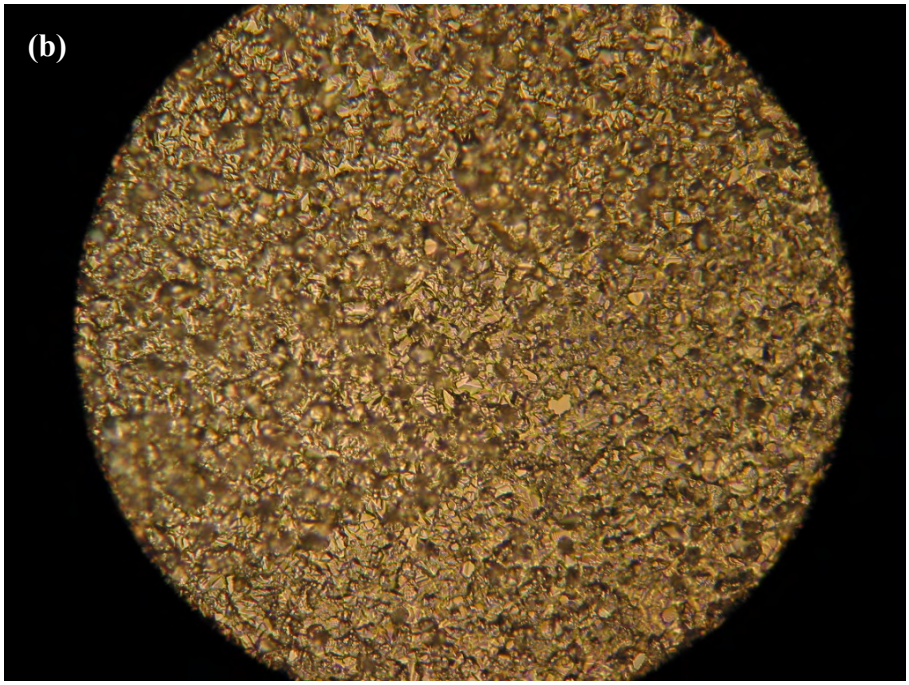

Fig. A.5: Pictures of (a) a pulsed electroplating apparatus and (b) a surface of the sample after electroplating through a microscope.

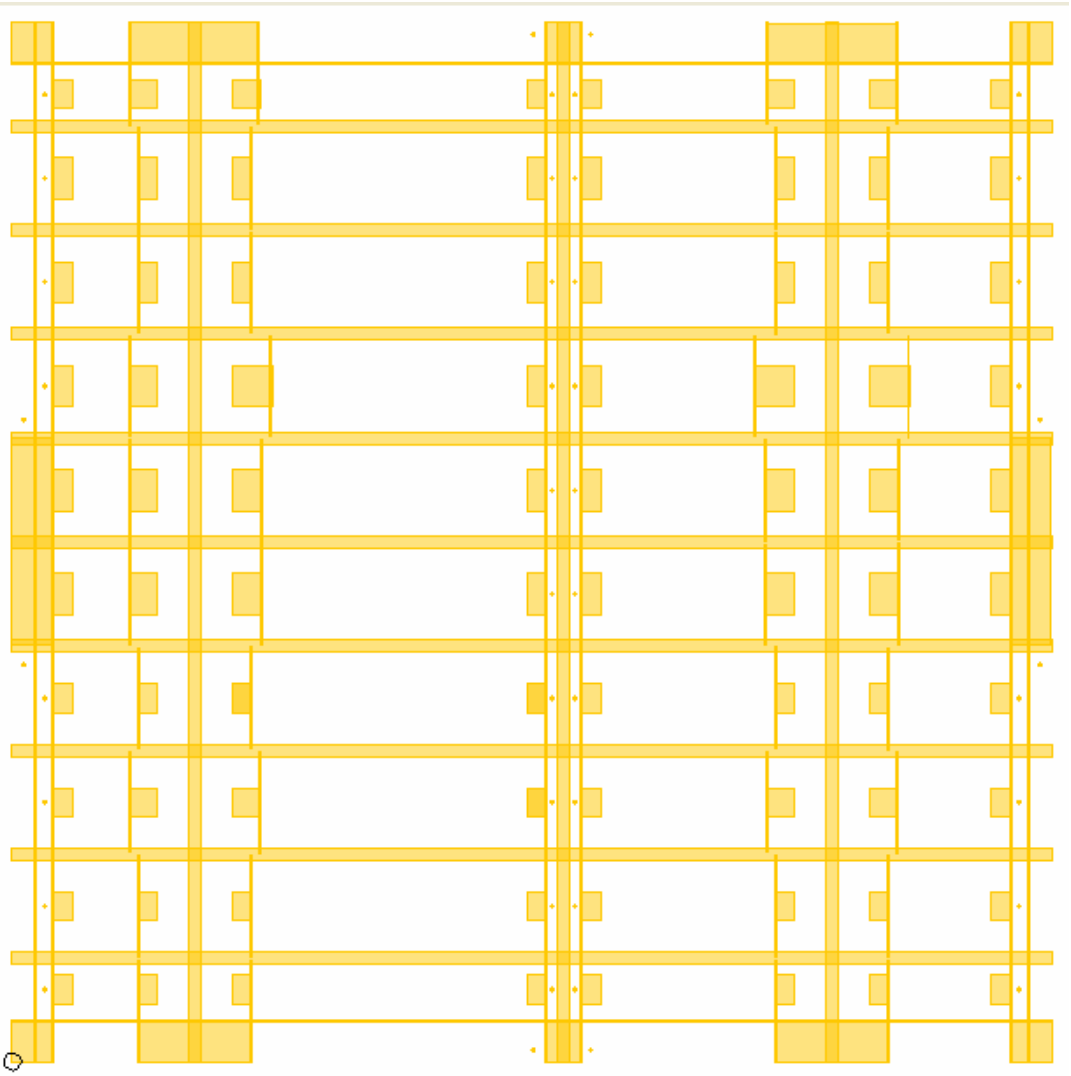

Fig. A.6: Mask design of electroplating for the second fabrication.

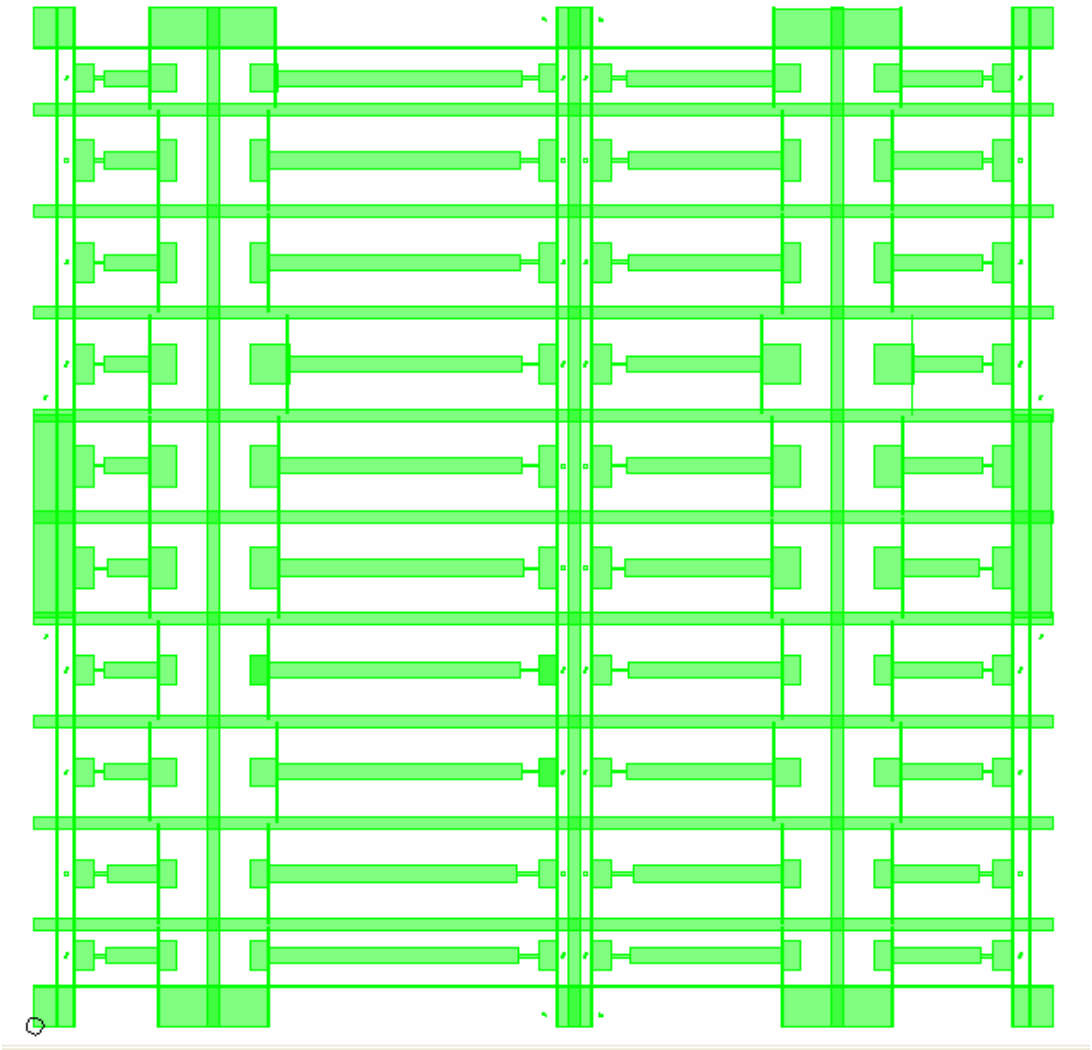

Fig. A.7: Mask design of RIE for the second fabrication.

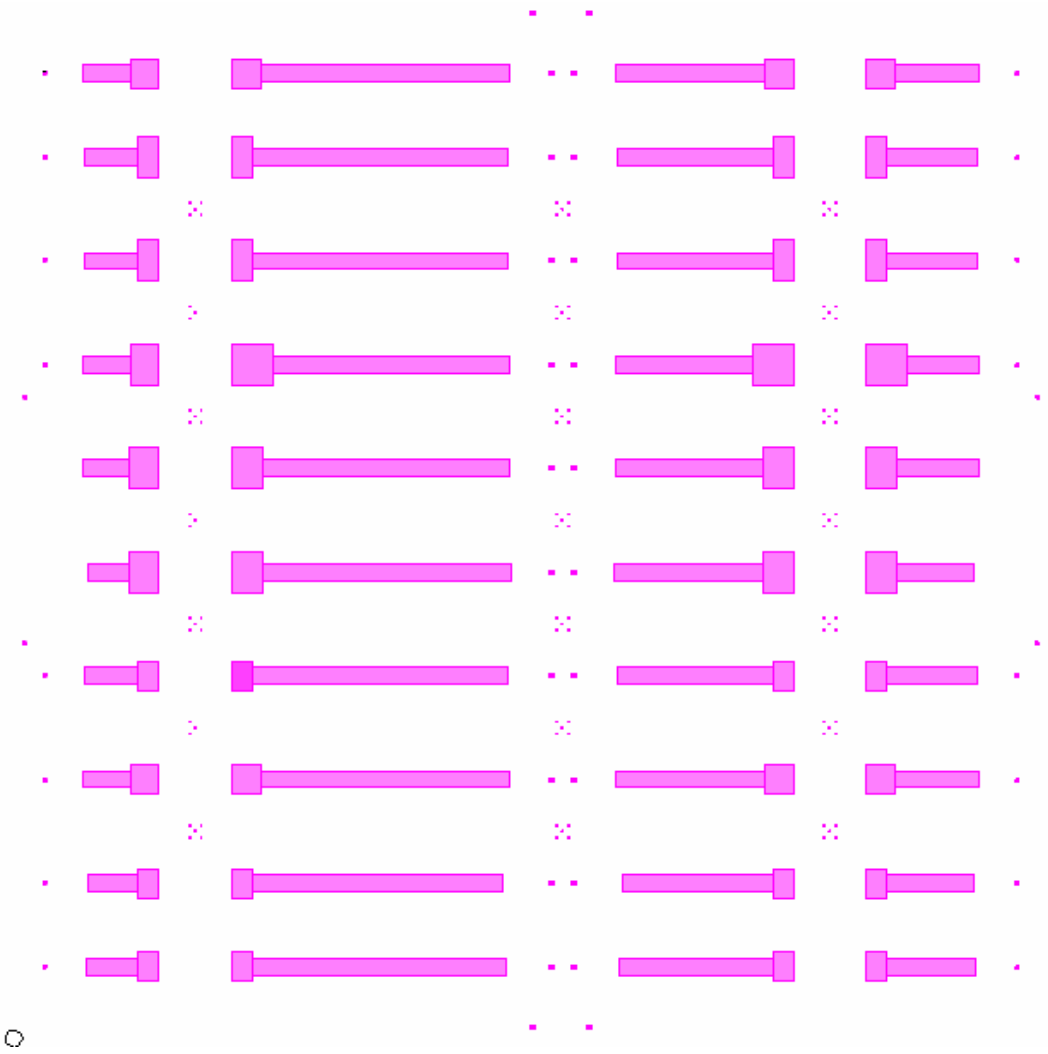

Fig. A.8: Mask design of DRIE for the second fabrication.

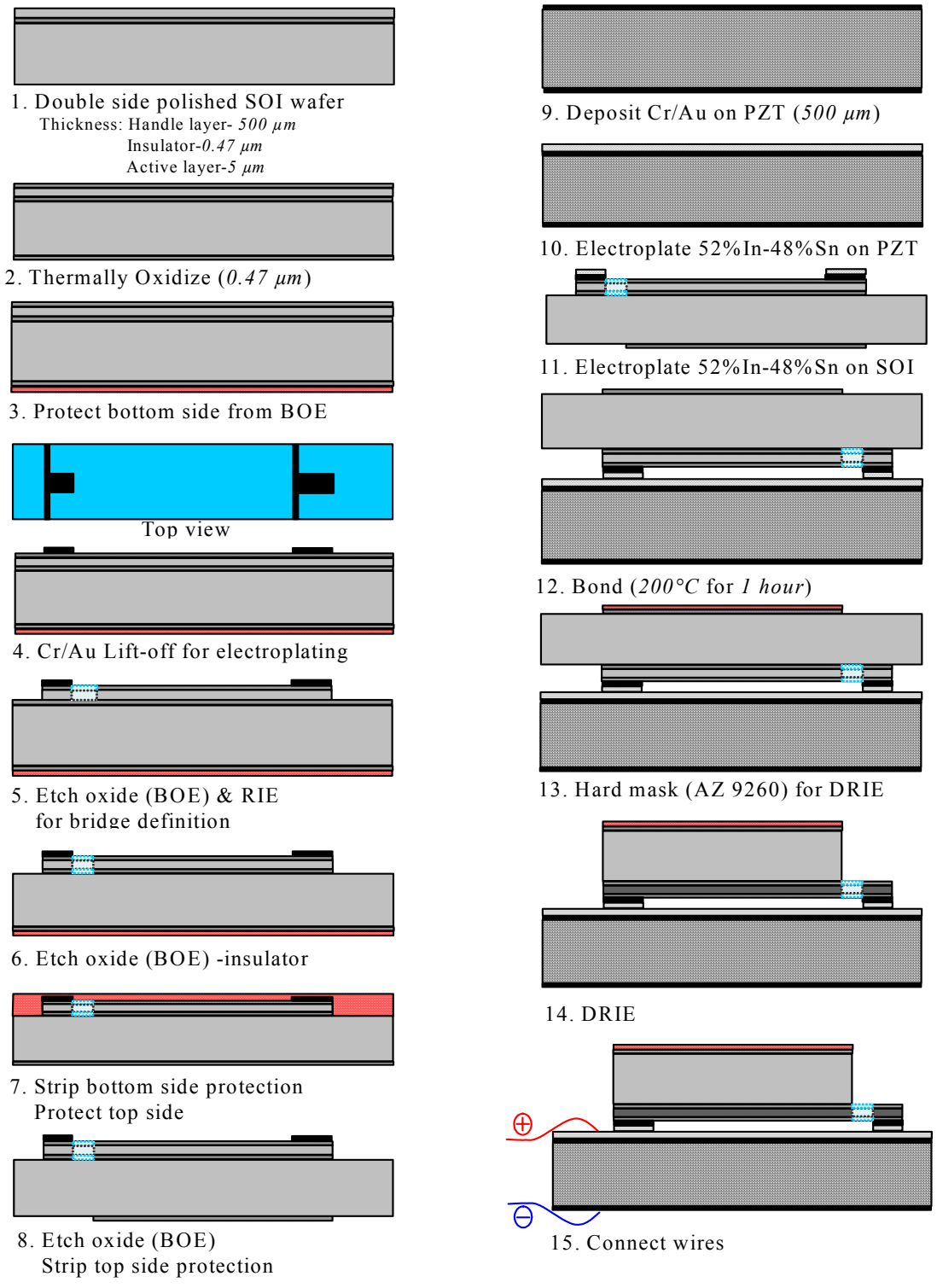

Fig. **A.9**: Schematic illustration of the second fabrication process.

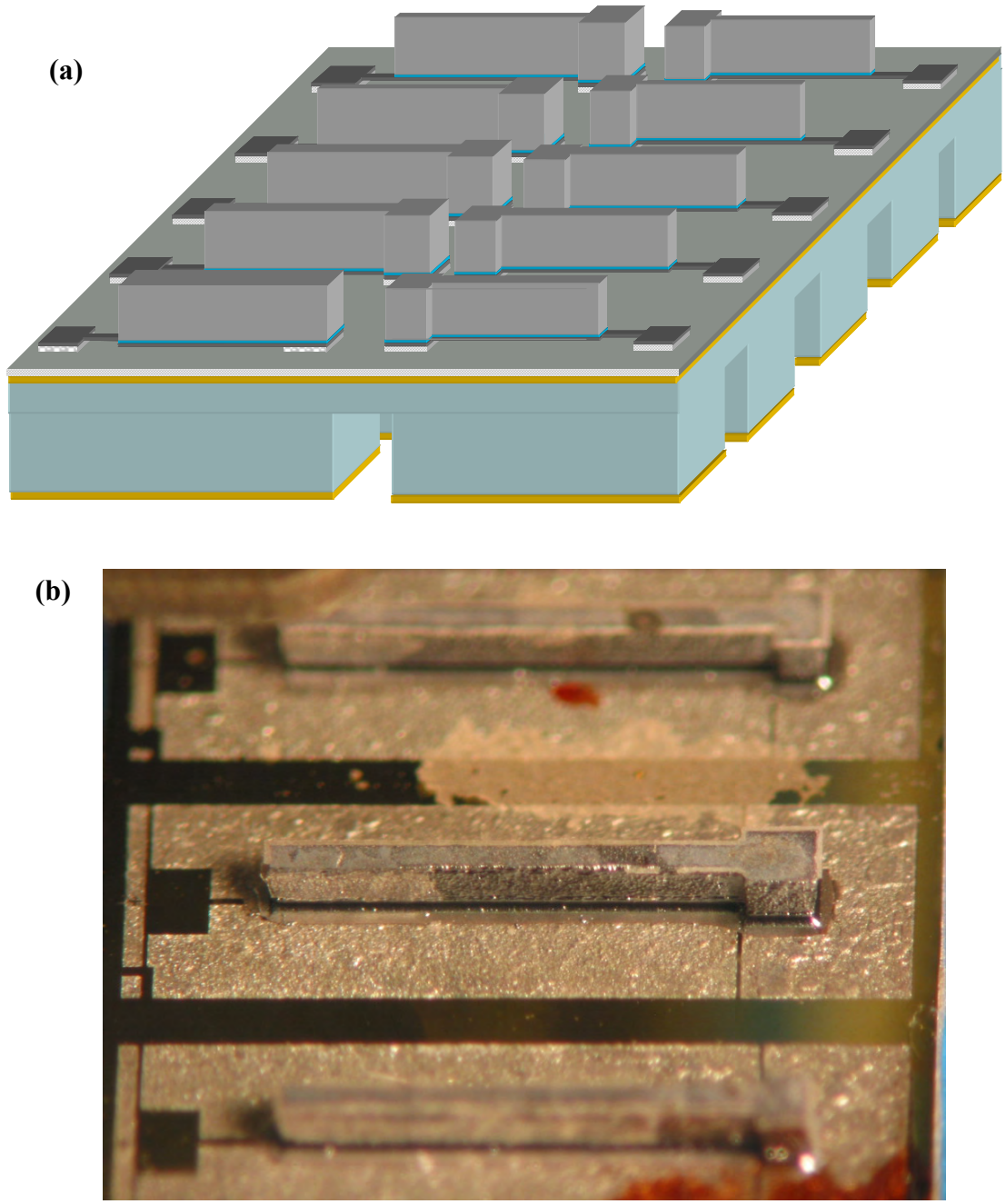

Fig. **A.10**: Released Structure just after DRIE on 1 in. by 1 in. chip: (a) schematic plan and (b) picture of an oblique view.

References

1. Uchino, K., *Piezoelectric Actuators and Ultrasonic Motors*. Electronic materials: Science and Technology, ed. H.L. Tuller. 1997: Kluwer Academic Publishers.

Appendix B

Static Analysis

B.1 Displacement

Equation **B.1** represents exact solution coefficients of Eq. **3.9**.

$$C_1 = -\frac{\left\{\begin{array}{l}\left(-120p^{\frac{3}{2}}a_6+720\sqrt{p}a_6-60p^{\frac{3}{2}}a_5-24p^{\frac{2}{3}}a_4-\frac{dw}{dx}(0)p^{\frac{5}{2}}+p^{\frac{5}{2}}\frac{dw}{dx}(1)\right)\sin\left(\sqrt{p}\right)\\+\left(30p^2a_6-360pa_6+20p^2a_5+12p^2a_4+p^3\frac{dw}{dx}(0)+p^3w(0)-p^3w(1)\right)\cos\left(\sqrt{p}\right)\\-360pa_6+90p^2a_6+40p^2a_5+12p^2a_4-w_{,x}(1)p^3+w(1)p^3-p^3w(0)\end{array}\right\}}{(p^{\frac{5}{2}})\sin\left(\sqrt{p}\right)+2p^2\cos\left(\sqrt{p}\right)-2p^2}$$

$$C_2 = -\frac{\left\{\begin{array}{l}\left(30p^{\frac{3}{2}}a_6-360a_6\sqrt{p}+20p^{\frac{3}{2}}a_5+12p^{\frac{3}{2}}a_4+p^{\frac{5}{2}}w(0)+w_{,x}(0)p^{\frac{5}{2}}-w(1)p^{\frac{5}{2}}\right)\sin(\sqrt{p})\\+\left(-720a_6+120pa_6+60pa_5+24pa_4+p^2w_{,x}(0)-w_{,x}(1)p^2\right)\cos(\sqrt{p})\\+720a_6-120pa_6-60pa_5-24pa_4+w_{,x}(1)p^2-p^2w_{,x}(0)\end{array}\right\}}{p^2\sin(\sqrt{p})+2p^{\frac{3}{2}}\cos(\sqrt{p})-2p^{\frac{3}{2}}} \qquad \textbf{(B.1)}$$

$$C_3 = -\frac{\left\{\begin{array}{l}\left(30p^{\frac{3}{2}}a_6-360a_6\sqrt{p}+20p^{\frac{3}{2}}a_5+12p^{\frac{3}{2}}a_4+p^{\frac{5}{2}}w(0)-w(1)p^{\frac{5}{2}}\right)\sin(\sqrt{p})\\+\left(120pa_6+60pa_5+24pa_4-p^2w_{,x}(0)-720a_6-w_{,x}(1)p^2\right)\cos(\sqrt{p})\\+720a_6-120pa_6-60pa_5+w_{,x}(1)p^2-24pa4+p^2w_{,x}(0)\end{array}\right\}}{p^{\frac{5}{2}}\sin(\sqrt{p})+2p^2\cos(\sqrt{p})-2p^2}$$

$$C_4 = \frac{\left\{\begin{array}{l}\left(-720a_6+120pa_6+60pa_5+24pa_4+p^2w_{,x}(0)+p^3w(0)\right)\sin(\sqrt{p})\\+\left(-30p^{\frac{3}{2}}a_6+360\sqrt{p}a_6-20p^{\frac{3}{2}}a_5-12p^{\frac{3}{2}}a_4-p^{\frac{5}{2}}w_{,x}(0)+p^{\frac{5}{2}}w(0)+p^{\frac{5}{2}}w(1)\right)\cos(\sqrt{p})\\+360a_6\sqrt{p}-90p^{\frac{3}{2}}a_6-40p^{\frac{3}{2}}a_5+w_{,x}(1)p^{\frac{5}{2}}-12p^{\frac{3}{2}}a_4-w(1)p^{\frac{5}{2}}-w(0)p^{\frac{5}{2}}\end{array}\right\}}{[p^{\frac{5}{2}}\sin(\sqrt{p})+2p^2\cos(\sqrt{p})-2*p^2]\sqrt{p}}$$

B.2 Blocked Force

B.2.1 Elastic Obstacle

Figure **B.1** shows a schematic diagram of the blocked force model. The objective is to determine the blocked force F_B as a function of the applied PZT force P and/or displacement U_L. Here, we can assume that the elastic property of the obstacle is represented as K, and the obstacle is located in $X = A$.

Using the same assumptions as in section **3.1** for quasi-static displacement, the transverse displacement is governed by [1, 2]

$$EI\left(\frac{d^4W}{dX^4} - \frac{d^4W_0}{dX^4}\right) + P\frac{d^2W}{dX^2} = -K(W - W_0)\delta(X - A) \qquad \textbf{(B.2)}$$

where $W_0 = \frac{G}{2}[1 - \cos(\frac{2\pi}{l_b}X)]$, K is the stiffness of an external elastic obstacle, A is the position of the external obstacle, and δ is the dirac function [3].

Integration Eq. **B.2** twice from 0 to X, two equations according to each domain can be obtained as

$$EI\frac{d^2W}{dX^2} + PW = C_1X + 2EI\frac{\pi^2}{l_b^2}G\left[\cos(\frac{2\pi}{l_b}X) - 1\right] + C_2 \qquad \text{for } X < A \qquad \textbf{(B.3)}$$

$$\begin{aligned} &EI\frac{d^2W}{dX^2} + PW && \text{for } X \geq A \\ &= C_1X - K\left[W(A) - W_0(A)\right](X - A) + 2EI\frac{\pi^2}{l_b^2}G\left[\cos(\frac{2\pi}{l_b}X) - \cos(\pi)\right] + C_3 \end{aligned} \qquad \textbf{(B.4)}$$

Using matching conditions and one boundary condition as

$$\frac{d^2W}{dX^2}(A^+) = \frac{d^2W}{dX^2}(A^-) \tag{B.5}$$

$$W(A^+) = W(A^-) \tag{B.6}$$

$$\frac{d^2W}{dX^2}(0) = \frac{d^2W}{dX^2}(l_b) \tag{B.7}$$

unknown coefficients of Eqs. **B.3** and **B.4** can be reduced respectively as

$$EI\frac{d^2W}{dX^2} + PW = \frac{K\left[W(A) - W_0(A)\right]}{2}X + 2EI\frac{\pi^2}{l_b^2}G\left[\cos(\frac{2\pi}{l_b}X) - 1\right] + C_2 \tag{B.8}$$

$$\begin{aligned} EI\frac{d^2W}{dX^2} + PW = {} & \frac{K\left[W(A) - W_0(A)\right]}{2}X + 2EI\frac{\pi^2}{l_b^2}G\left[\cos(\frac{2\pi}{l_b}X) - 1\right] + C_2 \\ & - K\left[W(A) - W_0(A)\right](X - A) \end{aligned} \tag{B.9}$$

To minimize the number of parameters in Eqs. **B.8** and **B.9**, the nondimensional variables and parameters are introduced.

$$X = l_b x,\ W = l_b w,\ A = l_b a,\ G = l_b g,\ [W(A) - W_0(A)] = l_b \beta,\ \rho = \frac{Pl_b^{\,2}}{EI},\ k = \frac{Kl_b^{\,3}}{EI} \tag{B.10}$$

Substitution of Eqs. **B.10** into Eqs. **B.8** and **B.9** respectively produces

$$\frac{d^2w}{dx^2} + \rho w = (1-a)k\beta x + 2\pi^2 g\left[\cos(2\pi x) - 1\right] + \frac{l_b}{EI}C_2 \qquad \text{for } x < a \tag{B.11}$$

$$\frac{d^2w}{dx^2} + \rho w = (1-a)k\beta(1-x) + 2\pi^2 g\left[\cos(2\pi x) - 1\right] + \frac{l_b}{EI}C_2 \quad \text{for } x \geq a\,. \tag{B.12}$$

Equations **B.11** and **B.12** show the ordinary differential equations governing the transverse displacement from the straight line respectively overcoming the obstacle. To solve these ordinary differential equations including unknown C_2, we need 5 boundary conditions as follows:

$$w(0)=0,\ \frac{dw}{dx}(0)=0 \tag{B.13}$$

$$w(1)=0,\ \frac{dw}{dx}(1)=0 \tag{B.14}$$

$$\frac{dw}{dx}(a^{-})=\frac{dw}{dx}(a^{+}) \tag{B.15}$$

Therefore, the nondimensionalized blocked force can be found using Eq. **B.16**

$$f_B = k[w(a)-w_0(a)] \tag{B.16}$$

and the actual blocked force can be converted as

$$F_B=\frac{EI}{l_b^{\,2}}f_B = K[w(a)-w_0(a)]l_b\,. \tag{B.17}$$

Also, if one wants to know the blocked force according to U_L, one can invert Eq. **B.18** to solve for u_L.

$$\begin{aligned} p &= \frac{l_b^{\,2}}{EI}P \\ &= v_l^2\left[-u_L-\frac{1}{2}\left[\int_0^{a^-}\left\{\left(\frac{dw}{dx}\right)^2-\left(\frac{dw_0}{dx}\right)^2\right\}dx+\int_{a^+}^{1}\left\{\left(\frac{dw}{dx}\right)^2-\left(\frac{dw_0}{dx}\right)^2\right\}dx\right]\right] \end{aligned} \tag{B.18}$$

Figures **B.2**~ **B.7** show the theoretical results of deflection and blocked force at midspan according the input u_L.

B.2.2 Solid Obstacle

Figure **B.8** shows a schematic diagram of the blocked force model with solid obstacle instead of the elastic one. The objective is also to determine the blocked force

F_B as a function of the applied PZT force P and/or displacement U_L. The domain is also divided into $W^L(X)$ for $X \in (0, A)$ and $W^R(X)$ for $X \in (A, l_b)$.

Using the same assumptions, non-dimensional variables, and parameters as in **3.1**, the transverse displacement is governed by

$$\frac{d^4 w^L}{dx^4} - \frac{d^4 w_0}{dx^4} + p\frac{d^2 w^L}{dx^2} = 0 \qquad \textbf{(B.19)}$$

$$\frac{d^4 w^R}{dx^4} - \frac{d^4 w_0}{dx^4} + p\frac{d^2 w^R}{dx^2} = 0. \qquad \textbf{(B.20)}$$

Substitution of a sinusoidal initial imperfection

$$w_0(x) = \frac{g}{2}[1 - \cos(2\pi x)] \qquad \textbf{(B.21)}$$

into Eqs. **B.19** and **B.20** produces the solution

$$w^L(x) = -p\cos(\sqrt{p}x)C_1 - p\sin(\sqrt{p}x)C_2 + C_3 x + C_4 + \frac{2\pi^2 g\cos(2\pi x)}{p - 4\pi^2} \qquad \textbf{(B.22)}$$

$$w^R(x) = -p\cos(\sqrt{p}x)D_1 - p\sin(\sqrt{p}x)D_2 + D_3 x + D_4 + \frac{2\pi^2 g\cos(2\pi x)}{p - 4\pi^2} \qquad \textbf{(B.23)}$$

Solving for the eight constants $C_1, \ldots, D_4$ requires eight boundary conditions.

$$w^L(0) = \frac{dw^L}{dx}(0) = w_0(0),\ w^L(a) = w_0(a), \qquad \textbf{(B.24)}$$

$$w^R(1) = \frac{dw^R}{dx}(1) = w_0(1),\ w^R(a) = w_0(a), \qquad \textbf{(B.25)}$$

$$\frac{dw^L}{dx}(a) = \frac{dw^R}{dx}(a), \qquad \textbf{(B.26)}$$

$$\frac{d^2 w^L}{dx^2}(a) = \frac{d^2 w^R}{dx^2}(a). \qquad \textbf{(B.27)}$$

The blocked force is calculated

$$F_B = -\frac{EI}{l_b^2}[\frac{d^3w^R}{dx^3}(a) - \frac{d^3w^L}{dx^3}(a)]. \qquad \textbf{(B.28)}$$

Finally, one may determine the requisite u_L from Eq. **B.29**

$$u_L = -\frac{p}{v_l^2} - \frac{1}{2}\left[\int_0^a \left\{\left(\frac{dw^L}{dx}\right)^2 - \left(\frac{dw_0}{dx}\right)^2\right\}dx + \int_a^1 \left\{\left(\frac{dw^R}{dx}\right)^2 - \left(\frac{dw_0}{dx}\right)^2\right\}dx\right]. \qquad \textbf{(B.29)}$$

Figures **B.9** and **B.10** plot the blocked force versus beam displacement. Figure **B.9** is for the smallest initial imperfection (g=1e-6), and Fig. **B.10** is for the medium [g=1e-3 (red dashed)] and the largest [g=5e-3 (green dotted)] cases. For the range of u_L shown, the blocked force is proportional to the applied contraction. For positive u_L (extension), the actuation pulls down, providing a negative force. For contraction ($u_L < 0$), a positive force is produced. The force increases proportionally with increasing imperfection. In the analytical results, the profiles are keeping the first symmetric mode until the 3rd critical load, so there is no big change in the ratio which means slope of the relationship between the blocked force and contraction as shown in Table **B.1**. However, after 3rd critical load, the shape looks like 2nd symmetric mode, so the ratio is somewhat increased. Also, the blocked force goes to infinite around 4th critical load (320*EI/L^2).

Finally, the ratio looks proportional to the initial imperfections.

Here, the snap-through action of this buckled beam due to blocked force should be considered because this clamped buckled beam is an example of a bistable structure in Fig. **B.11** if the external force is moving. The relationship between the deflection

according to blocked force and longitudinal force can be represented as Eqs. **B.30** and **B.31** [4, 5]

$$F(\eta) = -\frac{4(\eta l_b)^2 EI}{l_b^{\,3}} \sqrt{(d_o - d_P(\eta)) l_b} \times [3 - \frac{3}{\eta l_b} \tan(\frac{\eta l_b}{4}) + \tan^2(\frac{\eta l_b}{4})]^{-\frac{1}{2}} \quad \textbf{(B.30)}$$

$$W(\eta) = -\frac{L^3}{(\eta l_b)^2 EI} F(\eta)[0.25 - \frac{1}{\eta l_b} \tan(\frac{\eta l_b}{4})] \xrightarrow{F \to 0} \frac{2}{\pi} \sqrt{(d_o - d_P(\eta)) l_b} \quad \textbf{(B.31)}$$

where d_0 is the excess length of the free uncompressed beam from which $dp(\eta) = (\eta l_b)^2 I / l_b A$, that is, contraction from the longitudinal force is taken off, and $\eta^2 = \frac{P}{EI}$. The nondimensionalized force and deflection can be represented as Eqs. **B.32** and **B.33** to compare the results which are already obtained in blocked force model.

$$f_B = \frac{l_b^{\,2}}{EI} F_B = -4(\eta l_b)^2 \sqrt{\frac{[d_o - d_P(\eta)]}{l_b}} \times [3 - \frac{3}{\eta l_b} \tan(\frac{\eta l_b}{4}) + \tan^2(\frac{\eta l_b}{4})]^{-\frac{1}{2}} \quad \textbf{(B.32)}$$

$$w = \frac{W}{l_b} = -\frac{1}{(\eta l_b)^2} f(\eta)[0.25 - \frac{1}{\eta l_b} \tan(\frac{\eta l_b}{4})] \xrightarrow{f \to 0} \frac{2}{\pi} \sqrt{\frac{[d_o - d_P(\eta)]}{l_b}} l_b \quad \textbf{(B.33)}$$

However, during the snap-through F is no longer a function of η. In this transition, the blocked force becomes directly proportional to the deflection at a centre point as Eq. **B.34**.

$$w(f) \approx -\frac{1}{207.7} f \quad \textbf{(B.34)}$$

Therefore, the blocked force should be under the intersection (A in Fig. **B.12**) of Eqs. **B.33** and **B.34** to avoid the snap –through action.

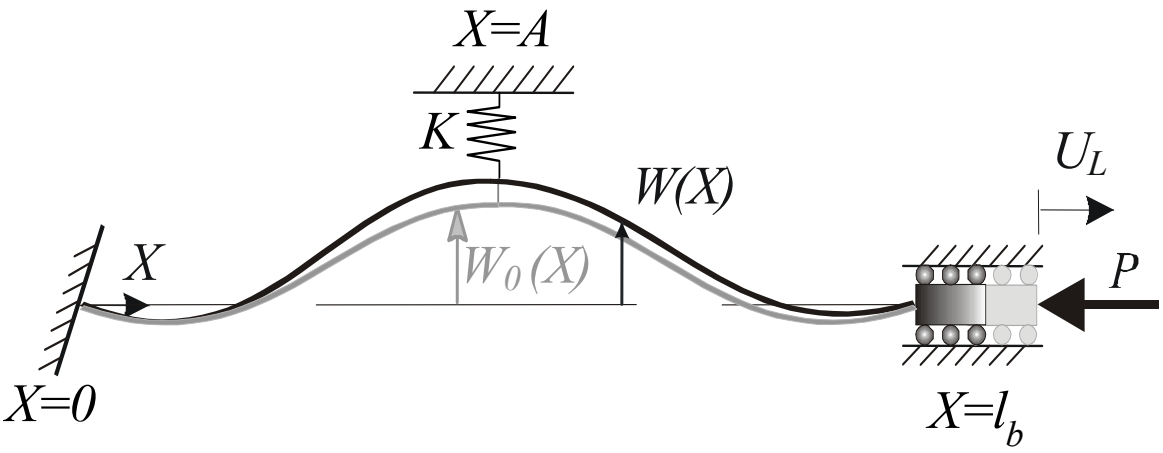

Fig. **B.1**: Schematic diagram of the blocked beam.

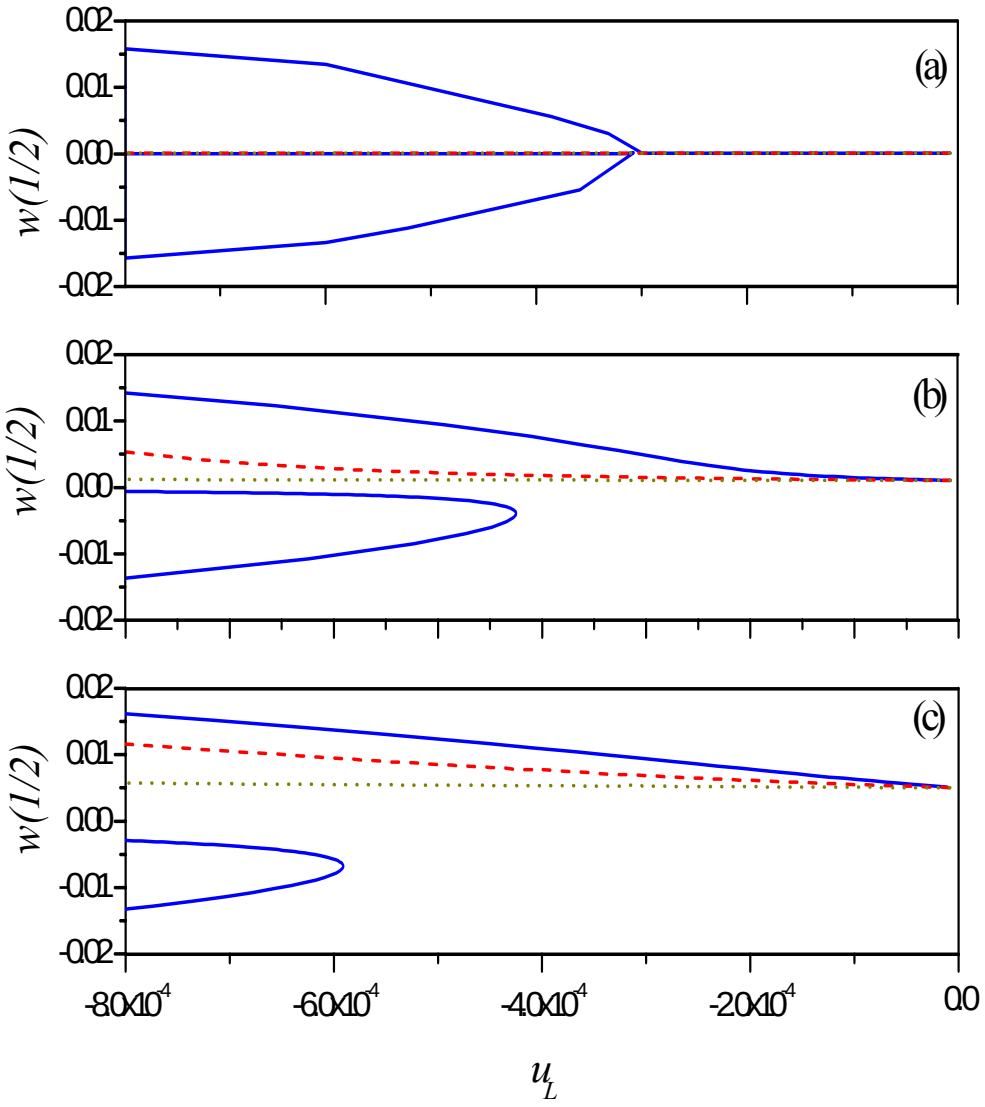

Fig. **B.2**: Theoretical results for a 520 μm×50 μm×5 μm beam buckled by a 4.66 mm long PZT actuator: (a) is for g=1e-6, (b) is for g=1e-3, and (c) is for g=5e-3 according to k=23.86 (solid), 238.6 (dash), and 2386 (dot).

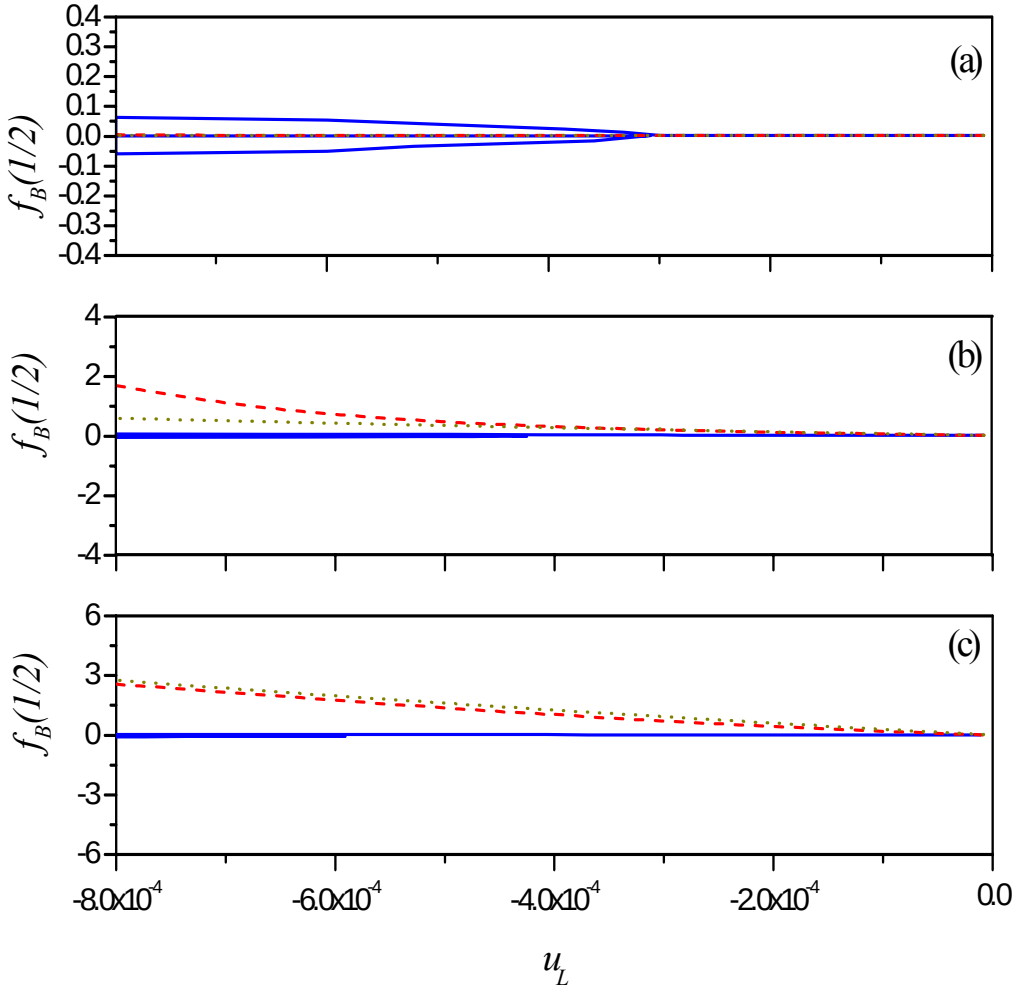

Fig. **B.3**: Theoretical results for a 520 μm×50 μm×5 μm beam buckled by a 4.66 mm long PZT actuator: (a) is for g=1e-6, (b) is for g=1e-3, and (c) is for g=5e-3 according to k=23.86 (solid), 238.6 (dash), and 2386 (dot).

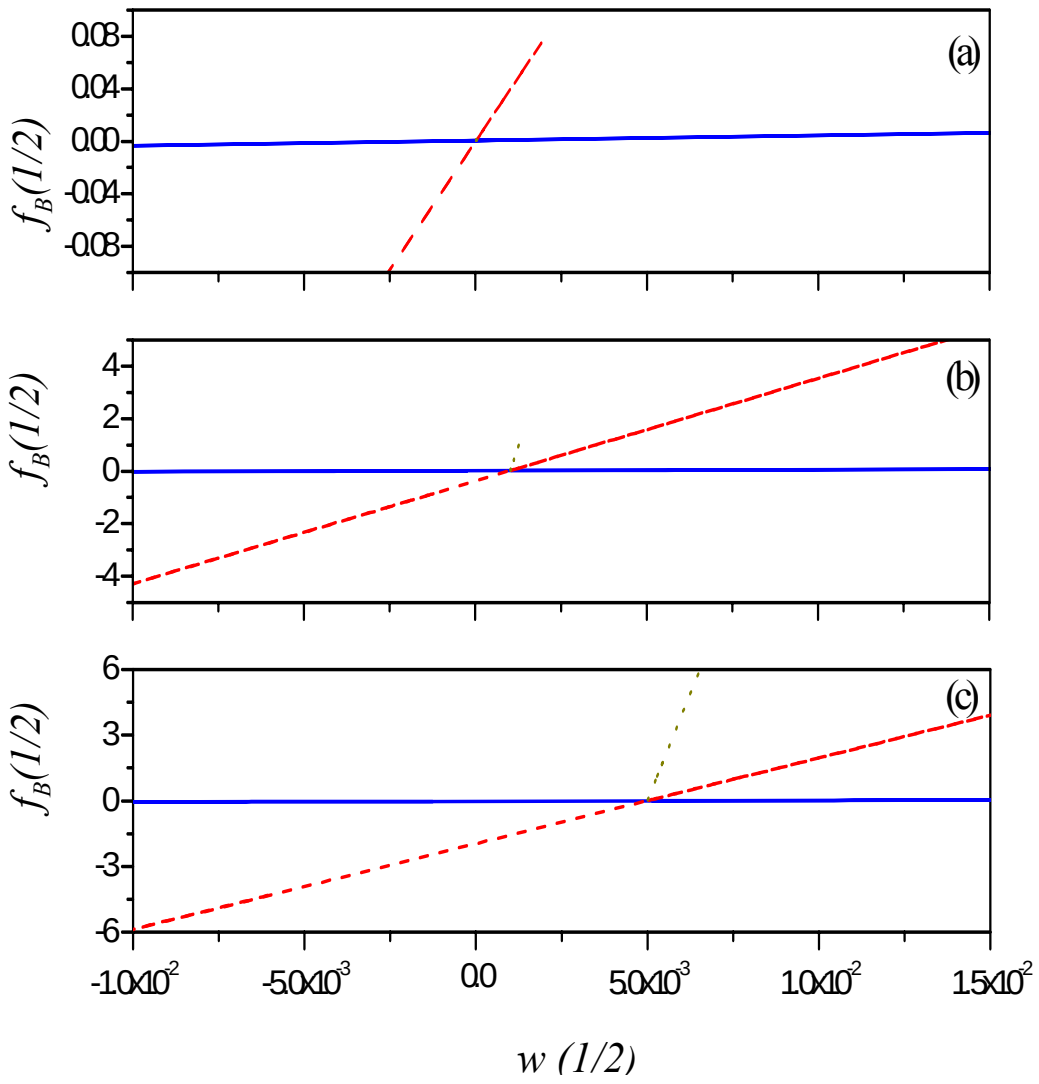

Fig. **B.4**: Theoretical results for a 520 μm×50 μm×5 μm beam buckled by a 4.66 mm long PZT actuator: (a) is for g=1e-6, (b) is for g=1e-3, and (c) is for g=5e-3 according to k=23.86 (solid), 238.6 (dash), and 2386 (dot).

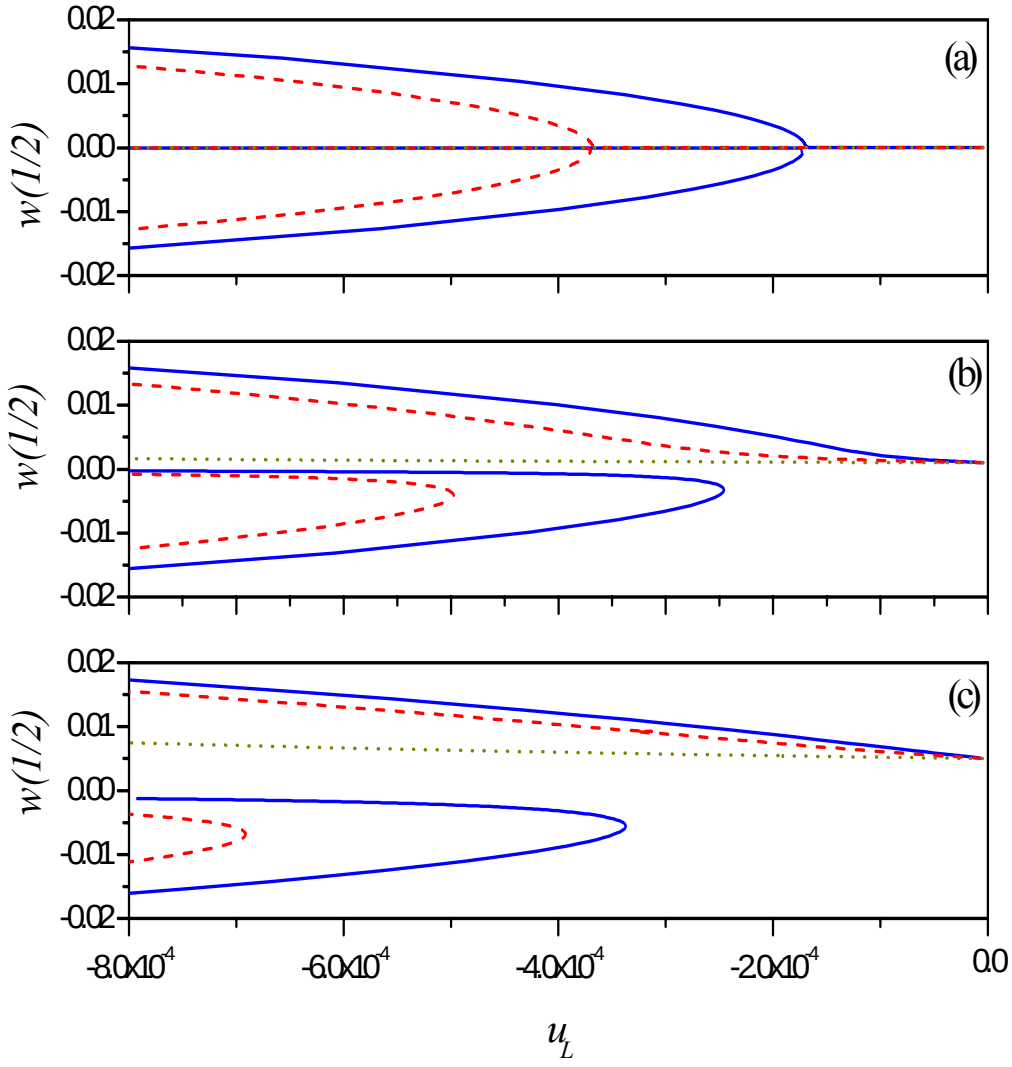

Fig. **B.5** Theoretical results for a 700 μm×200 μm×5 μm beam buckled by a 4.66 mm long PZT actuator: (a) is for g=1e-6, (b) is for g=1e-3, and (c) is for g=5e-3 according to k=23.86 (solid), 238.6 (dash), and 2386 (dot).

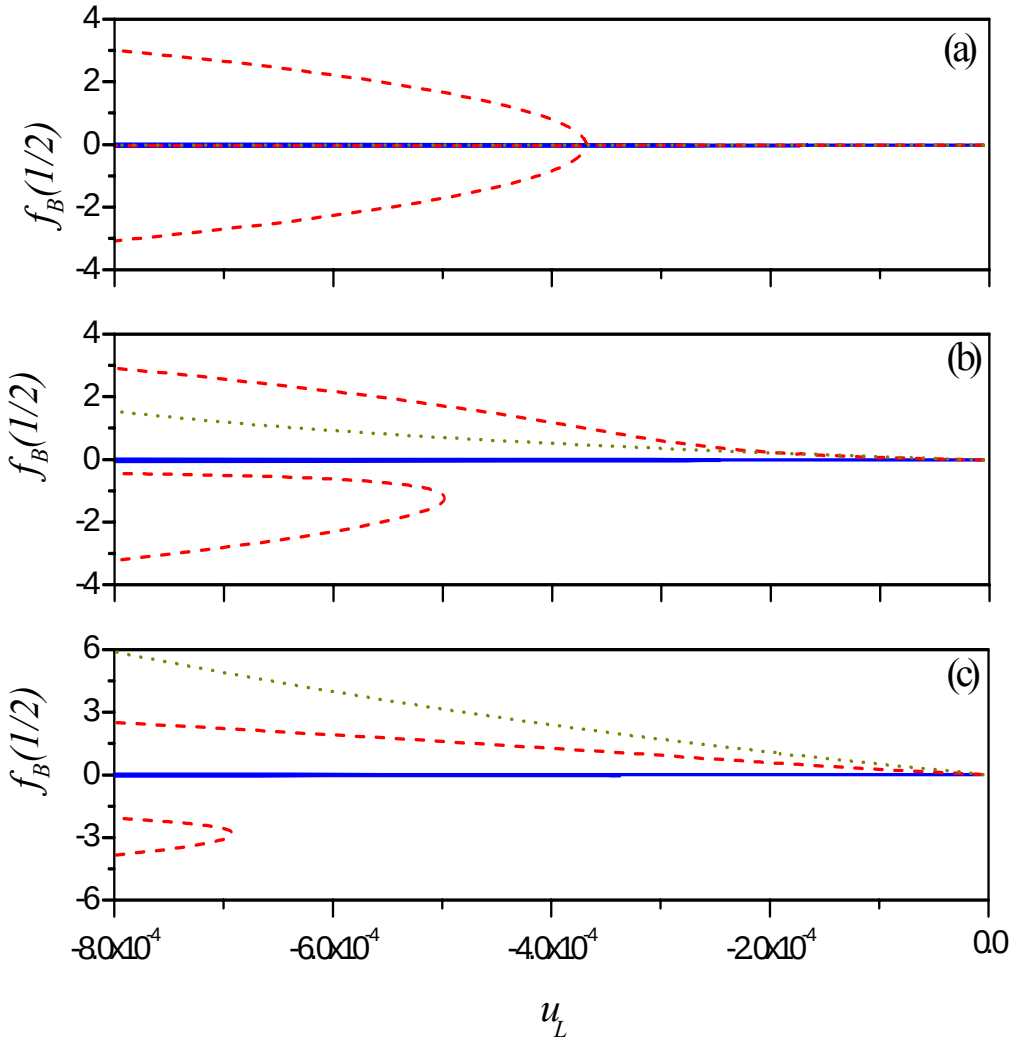

Fig. **B.6**: Theoretical results for a 700 μm×200 μm×5 μm beam buckled by a 4.66 mm long PZT actuator: (a) is for g=1e-6, (b) is for g=1e-3, and (c) is for g=5e-3 according to k=23.86 (solid), 238.6 (dash), and 2386 (dot).

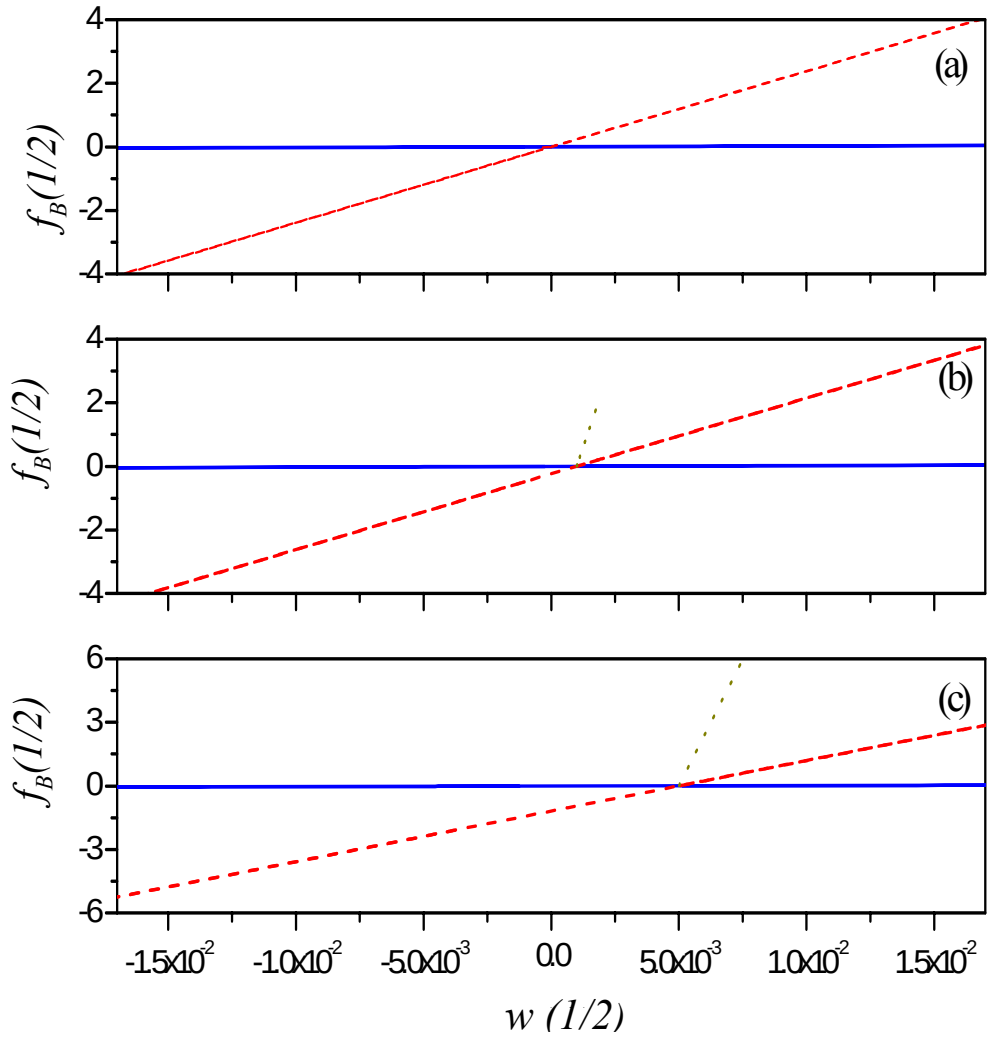

Fig. **B.7**: Theoretical results for a 700 μm×200 μm×5 μm beam buckled by a 4.66 mm long PZT actuator: (a) is for g=1e-6, (b) is for g=1e-3, and (c) is for g=5e-3 according to k=23.86 (solid), 238.6 (dash), and 2386 (dot).

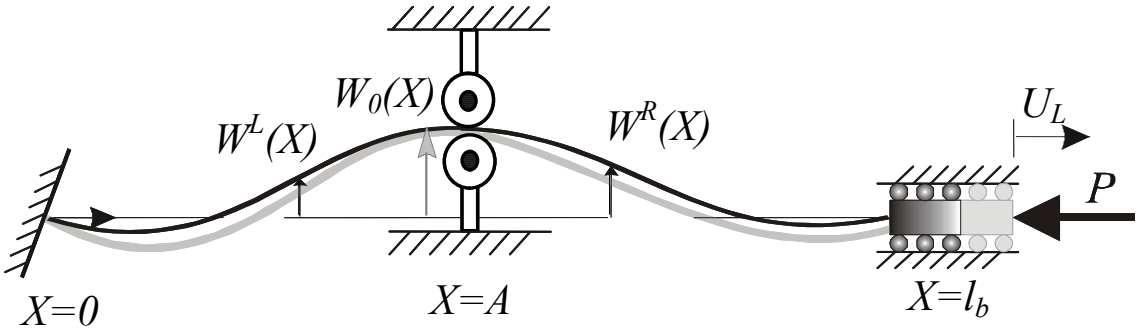

Fig. **B.8**: Schematic diagram of the blocked force model.

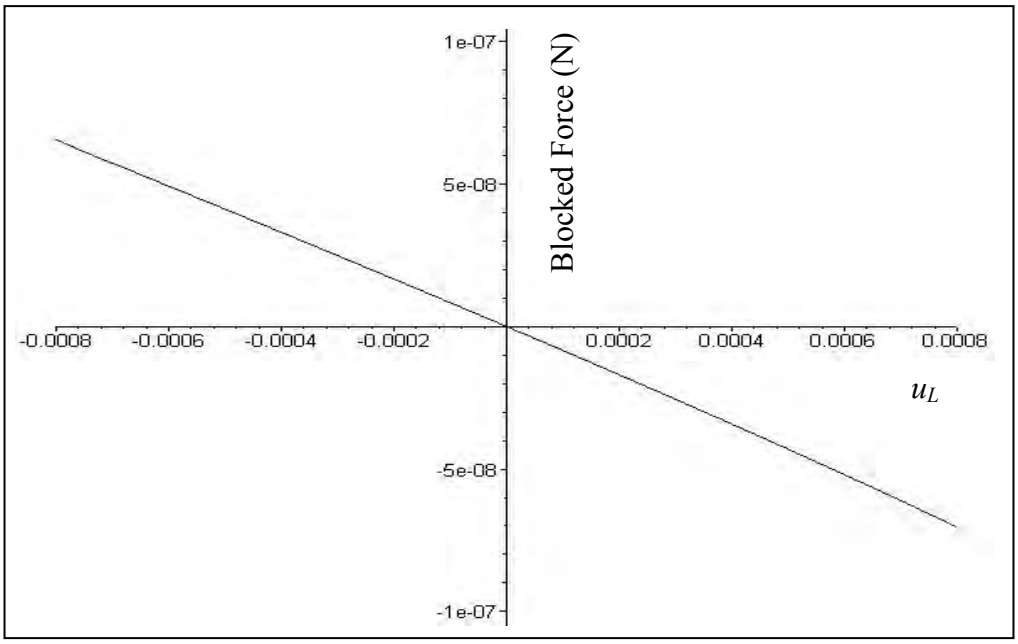

Fig. **B.9**: Blocked force versus contraction for sinusoidal initial shape (g=1e-6)

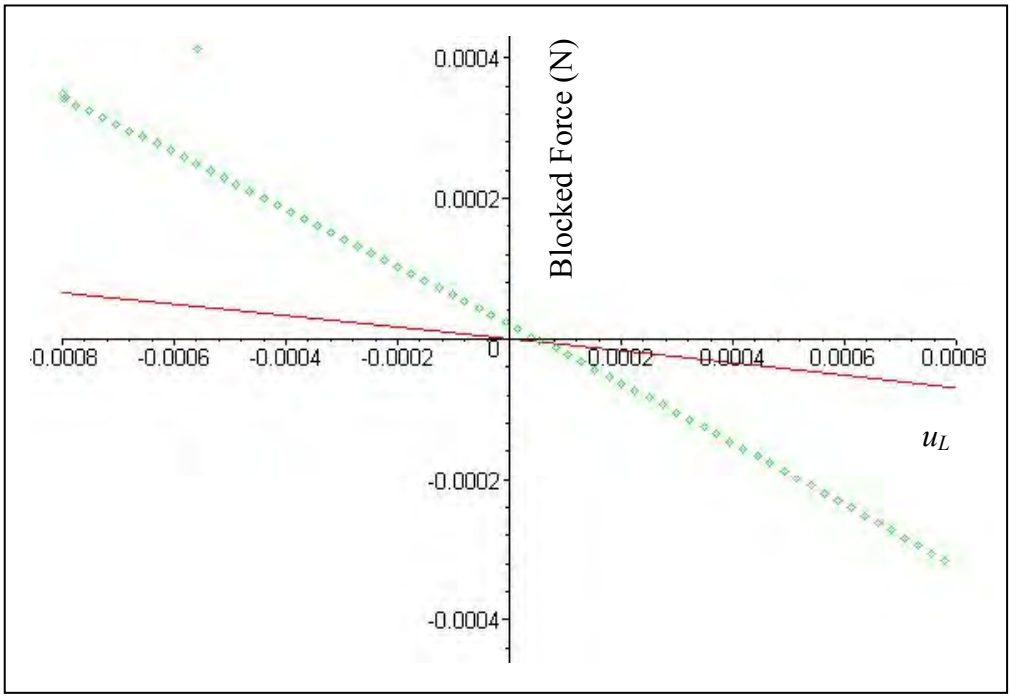

Fig. **B.10**: Blocked force versus contraction for sinusoidal initial shape [g=1e-3 (solid) and g=5e-3 (dotted)].

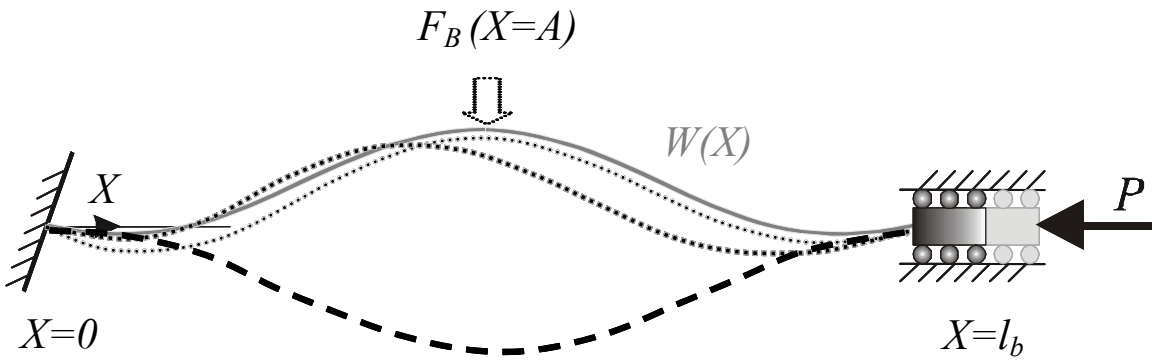

Fig. **B.11**: Schematic diagram of snap-through of the blocked.

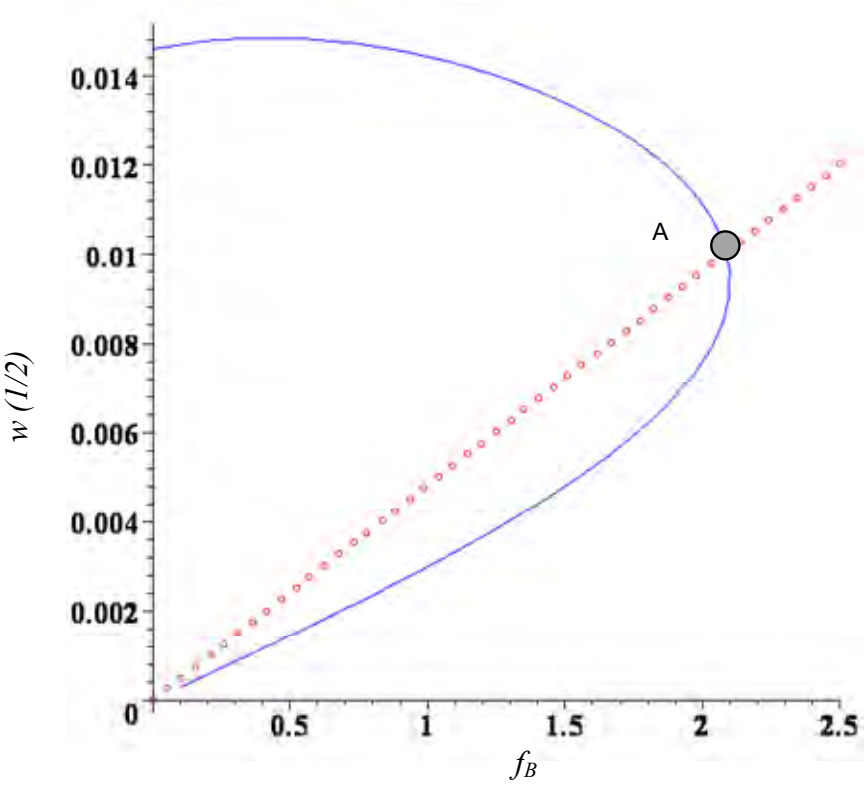

Fig. **B.12**: The relationship between the blocked force and a midspan displacement (solid curve) and the relationship after longitudinal force reaches the second critical load (dot line)

Table **B.1**: The ratio of blocked force to contraction.

Amplitude of initial imperfection	Ratio (Blocked force/U_L)						
g=1e-6	-0.164	1st critical load ($80.797^* EI/L^2$)	-0.171	2nd critical load ($157.9136^* EI/L^2$)	-0.187	3rd critical load ($238^* EI/L^2$)	-0.214
g=1e-3	-163.9		-170.9		-0.186.9		-214
g=5e-3	-767.2		-824.2		-889.4		-1002.5

References

1. Crandall, S.H., N.C. Dahl, and T.J. Lardner, *An Introduction to The Mechanics of Solids*. Second ed. Engineering Mechanics Series. 1978: Mcgraw-hill International Editions.

2. Timoshenko, S.P. and J.M. Gere, *Mechanics of Materials*. 1972, D.Van Nostrand.

3. Hayek, S.I., *Advanced Mathematical Methods in Science and Engineering*. 2001: Marcel dekker co.

4. Vangbo, M. and Y. Backlund, *A Lateral Symmetrically Bistable Buckled Beam.* J. Micromech. Microeng., 1998. 8: p. 29-32.

5. Vangbo, M., *An Analytical Analysis of a Compressed Bistable Buckled Beam.* Sensors and Actuators A, 1998. 69: p. 212-216.

Appendix C

Dynamic Analysis

C.1 Mounting

Mounting a device was a big issue from the design stage. One solution was clamping one side as Fig. C.1 (a), and other solution was attaching the device on the soft conductive material in Fig. C.1 (b). At first, the clamping solution was chosen because the motion of the PZT would be limited by the attached material. However, to reduce the effect of the PZT in dynamic test, the attaching solution was adopted. So a double sided adhesive carbon tape, which is very soft, was chosen. Before applying this to real devices, both static and dynamic performance was tested with only PZT. For static performance, it was checked that there is no change with clamping mounting. Figure C.2 shows experimental set-up to get dynamic responses.

Figure C.3 shows the frequency responses of the PZT with and without a carbon tape. As shown Fig. C.3 (b), the carbon tape is good to reduce the magnitude and to eliminate complicated motion of the PZT for analyzing only the micromachined beam. So it is concluded that this carbon tape can be used to hold real devices. Figure C.4 shows the picture of a actuator that is mounted on the carbon tape.

Figure C.5 shows the advantage of using carbon tape to analyze and to control the dynamic behavior of the micromachined beam. As mentioned, the method of

clamping one side causes to generate complicated motion of the PZT as Fig. C.5 (a), so it makes hard to analyze only the frequency response of the buckled beam as Fig. C.5 (b). However, due to effect of the carbon tape, some peaks of the PZT shown in Fig. C.5 (a) are eliminated as Fig. C.5 (c). The output of the buckled beam are also related not to the PZT but to the non-etched beam as Fig. C.5 (d). Therefore, this carbon tape is very useful to package this kind of devices, and we can control the motion of the etched beam from the design stage.

C.2 Numerical Codes

Section C.2.1 is for constants of integration in Eq. 4.12.

C.2.1 Modal Analysis

This is for getting natural frequency.

```
> restart:with(linalg, adj, coldim, det, diag, inverse, minor, multiply, rowdim, transpose) :
> with(linalg):
> with(plots):
> with(LinearAlgebra):
```

Initial imperfection w0

```
> w0:=a0+a1*xi+a2*xi^2+a3*xi^3+a4*xi^4+a5*xi^5+a6*xi^6:
> ode1:=diff(eta(xi),xi,xi,xi,xi)-omega^2*eta(xi)=A*vl^2*diff(w0,xi,xi):
```

```
> LH:=dsolve(ode1,parametric):
```

Separation with homogeneous and particular solution

```
> eta_h:=
        _C1*sin(omega^(1/2)*xi)+_C2*cos(omega^(1/2)*xi)+_C3*exp(omega^(1/2)*xi
        )+_C4*exp(-omega^(1/2)*xi):
> eta_p:=
        simplify(_C5*((omega^2*a2+360*a6+3*a3*xi*omega^2+6*a4*xi^2*omega^2+
        10*a5*xi^3*omega^2+15*a6*xi^4*omega^2)/omega^4)):
> new_eta:=eta_h+eta_p:
> new_eta_d:=diff(new_eta,xi):
> A:=int(diff(w0,xi)*diff(new_eta,xi),xi=0..1):
> B:=simplify((diff(new_eta,xi,xi,xi,xi)-omega^2*new_eta-A*vl^2*diff(w0,xi,xi))*35*
          omega^(5/2)):
> C:=collect(B,[_C1,_C2,_C3,_C4,_C5]):
> BC1:=collect(evalf(subs(xi=0,new_eta)),[_C1,_C2,_C3,_C4,_C5]):
> BC2:=collect(evalf(subs(xi=1,new_eta)),[_C1,_C2,_C3,_C4,_C5]):
> BC3:=collect(evalf(subs(xi=0,new_eta_d)),[_C1,_C2,_C3,_C4,_C5]):
> BC4:=collect(evalf(subs(xi=1,new_eta_d)),[_C1,_C2,_C3,_C4,_C5]):
> `AA`:=
        matrix(5,5,[[coeff(BC1,_C1),coeff(BC1,_C2),coeff(BC1,_C3),coeff(BC1,_C4),
        coeff(BC1,_C5)],[coeff(BC2,_C1),coeff(BC2,_C2),coeff(BC2,_C3),coeff(BC2
        ,_C4),coeff(BC2,_C5)],[coeff(BC3,_C1),coeff(BC3,_C2),coeff(BC3,_C3),coef
        f(BC3,_C4),coeff(BC3,_C5)],[coeff(BC4,_C1),coeff(BC4,_C2),coeff(BC4,_C3
```

```
),coeff(BC4,_C4),coeff(BC4,_C5)],[coeff(C,_C1),coeff(C,_C2),coeff(C,_C3),c
oeff(C,_C4),coeff(C,_C5)]]):
```

Parameters

```
> L:=400e-6:
> a0:=4E-05:
> a1:=- 0.0015:
> a2:=0.1346:
> a3:=- 0.5453:
> a4:=0.9929:
> a5:=- 0.8846:
> a6:=0.304:
>   h:=6e-6:
>   vl:=sqrt(12*l^2/h^2):
> m:=l*w*h*density/l:
> w:=50e-6:
> density:=2460:
> E:=125e9:
> I_m:=w*h^3/12:
> AAA:=simplify(evalf(subs(xi=0.5,det(AA)))):
> plot(AAA,omega=1..40,-2..2):
```

"nat" is a natural frequency.

```
> RootOf(AAA=0,omega,23):
> nat:=evalf(%):
```

```
> freq:=evalf(nat*sqrt(E*I_m/(m*l^4))/(2*Pi)):
> omega:=nat:
> `BB`:=matrix(4,1,[[-C5*(omega^2*a2+360.*a6)/omega^4],[-
      C5*(omega^2*a2+360.*a6+3.*a3*omega^2+6.*a4*omega^2+10.*a5*omega^
      2+15.*a6*omega^2)/omega^4],[-3.*C5*a3/omega^2],[-
      C5*(3.*a3*omega^2+12.*a4*omega^2+30.*a5*omega^2+60.*a6*omega^2)/o
      mega^4]]):
> `CC`:=
      Matrix(4,4,[[0,1,1,1],[sin(omega^(1/2)),cos(omega^(1/2)),exp(omega^(1/2)),ex
      p(-1.*omega^(1/2))],[omega^(1/2),0,omega^(1/2),-
      omega^(1/2)],[cos(omega^(1/2))*omega^(1/2),-
      sin(omega^(1/2))*omega^(1/2),omega^(1/2)*exp(omega^(1/2)),-
      omega^(1/2)*exp(-1.*omega^(1/2))]]):
> F:=inverse(CC):
> evalf(det(CC)):
> G:=multiply(F,BB):
> simplify(G):
> re:=
      simplify(G[1,1]*sin(omega^(1/2)*xi)+G[2,1]*cos(omega^(1/2)*xi)+G[3,1]*ex
      p(omega^(1/2)*xi)+G[4,1]*exp(-
      omega^(1/2)*xi)+C5*(omega^2*a2+360*a6+3*a3*xi*omega^2+6*a4*xi^2*o
      mega^2+10*a5*xi^3*omega^2+15*a6*xi^4*omega^2)/omega^4):
> C5:=1:
```

```
> plot(re,xi=0..1):
```

Solution independent with initial imperfection

```
> restart : with(linalg, adj, coldim, det, diag, inverse, minor, multiply, rowdim,
            transpose) :
> with(linalg):
> with(plots):
> with(LinearAlgebra):
> `A`:=Matrix(4,4,[[0,1,1,1],[sin(omega^(1/2)),cos(omega^(1/2)),exp(omega^(1/2)),exp(-
            1.*omega^(1/2))],[omega^(1/2),0,omega^(1/2),-
            omega^(1/2)],[cos(omega^(1/2))*omega^(1/2),-
            sin(omega^(1/2))*omega^(1/2),omega^(1/2)*exp(omega^(1/2)),-
            omega^(1/2)*exp(-1.*omega^(1/2))]]):
>`A2`:=matrix(3,3,[[0,1,1],[sin(omega^(1/2)),cos(omega^(1/2)),exp(omega^(1/2))],[ome
ga^(1/2),0,omega^(1/2)]]):
> P:=det(A):
> a:=h*w:
```

Parameters

```
> m:=l*w*h*density/l:
> l:=400e-6:
> h:=6e-6:
> vl:=sqrt(12*l^2/h^2):
> m:=l*w*h*density/l:
> w:=50e-6:
```

```
> density:=2460:

> E:=125e9:

> I_m:=w*h^3/12:

> P2:=evalf(P):

> plot(P2,omega=0..200,-0.000002..0.000002):

> RootOf(P2=0,omega,61):

> nat:=evalf(%):

> freq:=evalf(nat*sqrt(E*I_m/(m*l^4))/(2*Pi)):

> omega:=nat:

> `B2`:=matrix(3,1,[[-C4],[-exp(-1.*omega^(1/2))*C4],[omega^(1/2)*C4]]):

> C2:=inverse(A2):

> G2:=multiply(C2,B2):

> simplify(G2):

> re2:=
        simplify(G2[1,1]*sin(omega^(1/2)*xi)+G2[2,1]*cos(omega^(1/2)*xi)+G2[3,1]
        *exp(omega^(1/2)*xi)+C4*exp(-omega^(1/2)*xi)):

> C4:=1e9:

> plot(re2,xi=0..1):
```

C.2.2 Frequency Response Function

C.2.2.1 is related with Eqs. 4.13 ~ 4.18, and C.2.2.2 is for Eq. 4.20.

C.2.2.1 Maple

This is for getting Frequency Response Functions.

```
> restart:
> with(linalg, adj, coldim, det, diag, inverse, minor, multiply, rowdim, transpose) :
> with(linalg):
> with(plots):
> with(LinearAlgebra):
> w0:=a0+a1*xi+a2*xi^2+a3*xi^3+a4*xi^4+a5*xi^5+a6*xi^6:
> ode1:=diff(eta(xi),xi,xi,xi,xi)+(c*i*omega-omega^2)*eta(xi)= CI*vl^2*diff(w0,xi,xi)
        +vl^2*diff(w0,xi,xi)*ul:
> LH:=dsolve(ode1,parametric):
```

The solution can be devided into a homogeneous solution (eta_h) and a particular solution (eta_p). eta_p2 and eta_p3 are just modified to collect _CI.

```
> eta_h:=_C1*exp((-omega*(c*i-omega))^(1/4)*xi)+_C2*exp(-(-omega*(c*i-omega))
        ^(1/4)*xi) +_C3*exp((-omega*(c*i-omega))^(1/4)*xi*i)+_C4*exp(-i*(-
        omega*(c*i-omega))^(1/4)*xi):
> eta_p:=2*vl^2*(-3*a3*xi*omega^3*ul-3*a3*xi*omega^3*CI +3*a3*xi*omega*ul*c^2
        + 3*a3*xi*omega*CI*c^2-6*a4*xi^2*omega^3*ul-6*a4*xi^2*omega^3*CI
```

```
        +360*i*CI*a6*c+360*i*ul*a6*c-CI*a2*omega^3+6*a4*xi^2*omega*ul*c^2
        +6*a4*xi^2*omega*CI*c^2-10*a5*xi^3*omega^3*ul-10*a5*xi^3*omega^3*CI
        -15*a6*xi^4*omega^3*ul-15*a6*xi^4*omega^3*CI+6*i*a3*xi*omega^2*ul*c
        +6*i*a3*xi*omega^2*CI*c+2*i*CI*a2*omega^2*c+12*i*a4*xi^2*omega^2*ul
        *c+12*i*a4*xi^2*omega^2*CI*c+20*i*a5*xi^3*omega^2*ul*c+20*i*a5*xi^3
        *omega^2*CI*c+30*i*a6*xi^4*omega^2*ul*c+30*i*a6*xi^4*omega^2*CI*c+
        2*i*ul*a2*omega^2*c+10*a5*xi^3*omega*ul*c^2+10*a5*xi^3*omega*CI*c^
        2+15*a6*xi^4*omega*ul*c^2-ul*a2*omega^3-360*ul*a6*omega-
        360*CI*a6*omega +15*a6*xi^4*omega*CI*c^2+CI*a2*omega*c^2
        +ul*a2*omega*c^2)/omega^2/(2*i*c*omega-omega^2+c^2)/(c*i-omega):
> eta_P2:=collect(eta_p,[CI,ul]):
> eta_p3:=_CI*(30*i*a6*xi^4*omega^2*c+6*i*a3*xi*omega^2*c-3*a3*xi*omega^3+
        3*a3*xi*omega*c^2-6*a4*xi^2*omega^3+12*i*a4*xi^2*omega^2*c
        +6*a4*xi^2*omega*c^2+360*i*a6*c-10*a5*xi^3*omega^3-
        15*a6*xi^4*omega^3 +10*a5*xi^3*omega*c^2+20*i*a5*xi^3*omega^2*c
        +15*a6*xi^4*omega*c^2+2*i*a2*omega^2*c-a2*omega^3-360*a6*omega
        +a2*omega*c^2)/omega^2/(2*i*c*omega-omega^2+c^2)/(c*i-omega)
        +2*vl^2*(30*i*a6*xi^4*omega^2*c+6*i*a3*xi*omega^2*c-
        3*a3*xi*omega^3+3*a3*xi*omega*c^2-6*a4*xi^2*omega^3
        +12*i*a4*xi^2*omega^2*c +6*a4*xi^2*omega*c^2+360*i*a6*c-
        10*a5*xi^3*omega^3 -15*a6*xi^4*omega^3+10*a5*xi^3*omega*c^2
        +20*i*a5*xi^3*omega^2*c+15*a6*xi^4*omega*c^2+2*i*a2*omega^2*c-
```

```
        a2*omega^3-360*a6*omega+a2*omega*c^2)/omega^2/(2*i*c*omega-
        omega^2+c^2)/(c*i-omega)*ul:
> new_eta:=eta_h+eta_p3:
> new_eta_d:=diff(new_eta,xi):
> CI:=int(diff(w0,xi)*diff(new_eta,xi),xi=0..1):
> BC5:=diff(new_eta,xi,xi,xi,xi)+(i*omega-omega^2)*new_eta-CI*vl^2*diff(w0,xi,xi)-
        vl^2*diff(w0,xi,xi)*ul:
```

Boundary conditions

```
> BC1:=evalf(subs(xi=0,new_eta)):
> BC2:=evalf(subs(xi=1,new_eta)):
> BC3:=evalf(subs(xi=0,new_eta_d)):
> BC4:=evalf(subs(xi=1,new_eta_d)):
> A:=
        matrix([[coeff(BC1,_C1),coeff(BC1,_C2),coeff(BC1,_C3),coeff(BC1,_C4),coef
        f(BC1,_CI)],[coeff(BC2,_C1),coeff(BC2,_C2),coeff(BC2,_C3),coeff(BC2,_C4),
        coeff(BC2,_CI)],[coeff(BC3,_C1),coeff(BC3,_C2),coeff(BC3,_C3),coeff(BC3,_
        C4),coeff(BC3,_CI)],[coeff(BC4,_C1),coeff(BC4,_C2),coeff(BC4,_C3),coeff(B
        C4,_C4),coeff(BC4,_CI)],[coeff(BC5,_C1),coeff(BC5,_C2),coeff(BC5,_C3),coe
        ff(BC5,_C4),coeff(BC5,_CI)]]):
> b:=matrix([[-coeff(BC1,ul)],[-coeff(BC2,ul)],[-coeff(BC3,ul)],[-coeff(BC4,ul)],[-
        coeff(BC5,ul)]]):
> e:=matrix([[coeff(new_eta,_C1),coeff(new_eta,_C2),coeff(new_eta,_C3),
        coeff(new_eta,_C4), coeff(new_eta,_CI)]]):
```

```
> d:=matrix([[coeff(new_eta, ul)]]):

> with(CodeGeneration):

> Matlab(A):

> Matlab(b):

> Matlab(e):

> Matlab(d):
```

These obtained matrix and vectors are transfered to MATLAB for Eq. **4.20**.

C.2.2.2 Matlab

```
clear;

%Coefficients of initial imperfection

 a0= 0;

 a1=- 0.0036;

 a2=- 0.0576;

 a3=2.0255;

 a4=- 6.0136;

 a5=6.2272;

 a6= -2.1779;

%Parameters

 l=600e-6;

 c=0.337;

 h=6e-6;
```

```
wide=100e-6;
density=2460;
E=125e9;
I_m=wide*h^3/12;
vl=sqrt(12*l^2/h^2);
m=l*wide*h*density/l;
%Position for test
xi=0.4
%omegavec=logspace(10,log10(sqrt(10)),1000);
z=10000;
omegavec=logspace(0,2,z);
%For omega=omegavec,
 for k=1:z
    omega=omegavec(k),
%Following vector and matrics are from other results
   A = [comes from C.2.2.1];
   b = [comes from C.2.2.1];
   e_T= [comes from C.2.2.1];
   d = [comes from C.2.2.1];
G(k) = i*omega*(e_T*(inv(A)*b)+d);
   G2=abs(G);
end
waxis = omegavec;
```

```
plot(waxis,G2/10);
xlabel('Nondimensional frequency')
ylabel('Mobility')
hold on;
% This is for experiemtal results.
t=0:2e-7:0.01;
load Device2.mat;
x=Device2(:,2);
[freq.xfft]=fftplot(t,x)
```

C.3 Multi-mode Galerkin Discretization

Figure C.6 and Eq. C.1 shows the four modes that are used in Galerkin's method.

$$
\begin{aligned}
w_0 1 &= \text{-}.9999998691\cos(4.730040745x) + .9825023299\sin(4.730040745x) \\
&\quad + 1.000000158\cosh(4.730040745x) \text{ - } .9825023744\sinh(4.730040745x) \\
w_0 2 &= 1.000000304\cos(7.853204624x) \text{ - } 1.000777084\sin(7.853204624x) \\
&\quad \text{-}.9999995200\cosh(7.853204624x) + 1.000776832\sinh(7.853204624x) \\
w_0 3 &= 1.000285795\cos(10.99560784x) \text{ - } .9997022221\sin(10.99560784x) \\
&\quad \text{-}.9996899045\cosh(10.99560784x) + .9996563515\sinh(10.99560784x) \\
w_0 4 &= \text{-}.9999252306\cos(14.13716549x) + .9997981301\sin(14.13716549x) \\
&\quad + .9997779074\cosh(14.13716549x) \text{ - } .9997793629\sinh(14.13716549x)
\end{aligned}
\qquad \text{(C.1)}
$$

Equation C.2 are calculated matrix and vector from Eq. 4.23.

B(1,1) = 0.1230262E2
B(1,2) = -0.9421982E-5
B(1,3) = 0.973028E1
B(1,4) = 0.9692004E-2
B(2,1) = -0.9421982E-5
B(2,2) = 0.4605013E2
B(2,3) = 0.1596899E-1
B(2,4) = 0.1714403E2
B(3,1) = 0.973028E1
B(3,2) = 0.1596899E-1
B(3,3) = 0.9890974E2
B(3,4) = -0.759539E-2
B(4,1) = 0.9692004E-2
B(4,2) = 0.1714403E2
B(4,3) = -0.759539E-2
B(4,4) = 0.1714803E3

D(1,1) = 0.5005639E3
D(1,2) = -0.301174E-3
D(1,3) = 0.680831E-1
D(1,4) = -0.1654444E1
D(2,1) = -0.301174E-3
D(2,2) = 0.3803537E4
D(2,3) = 0.1513484E1
D(2,4) = -0.3368285E1
D(3,1) = 0.680831E-1
D(3,2) = 0.1513484E1
D(3,3) = 0.1461764E5
D(3,4) = 0.7167196E1
D(4,1) = -0.1654444E1
D(4,2) = -0.3368285E1
D(4,3) = 0.7167196E1
D(4,4) = 0.3994383E5

(**C.2**)

r(1,1) = -0.1654444E1
r(2,1) = -0.3368285E1
r(3,1) = 0.7167196E1
r(4,1) = 0.3994383E5

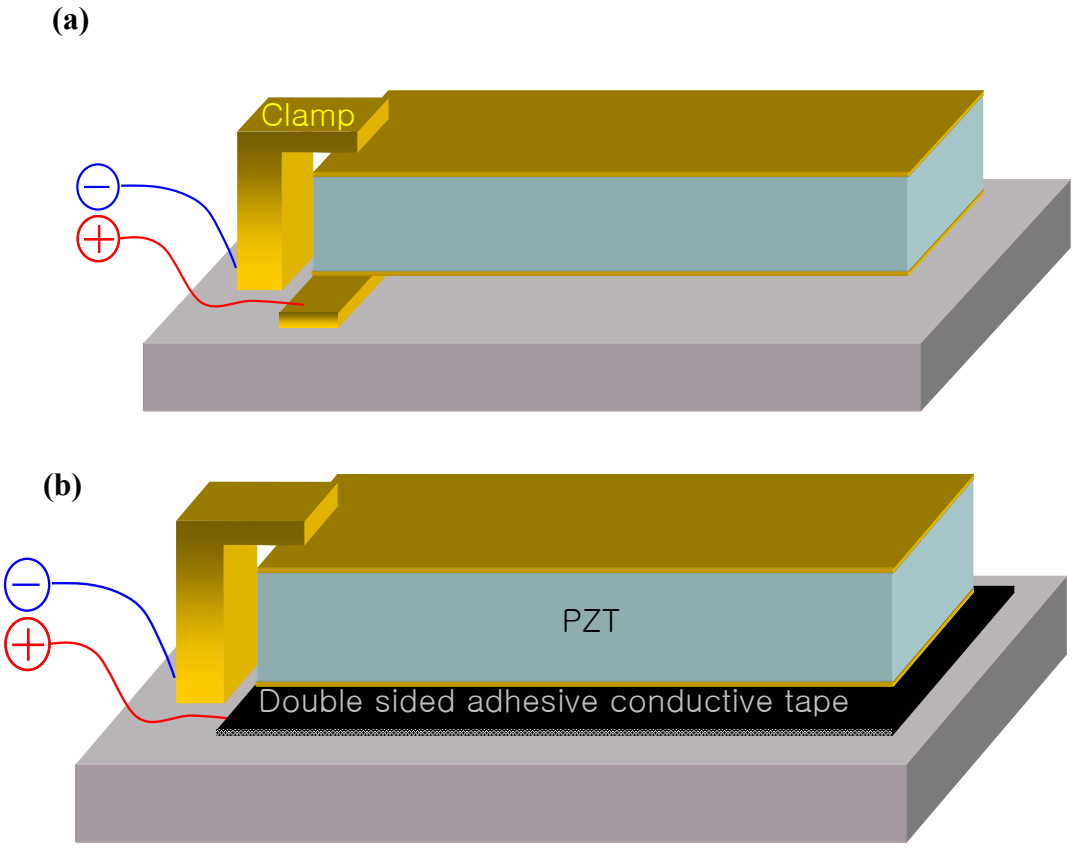

Fig. **C.1**: Mounting method: (a) clamping and (b) taping.

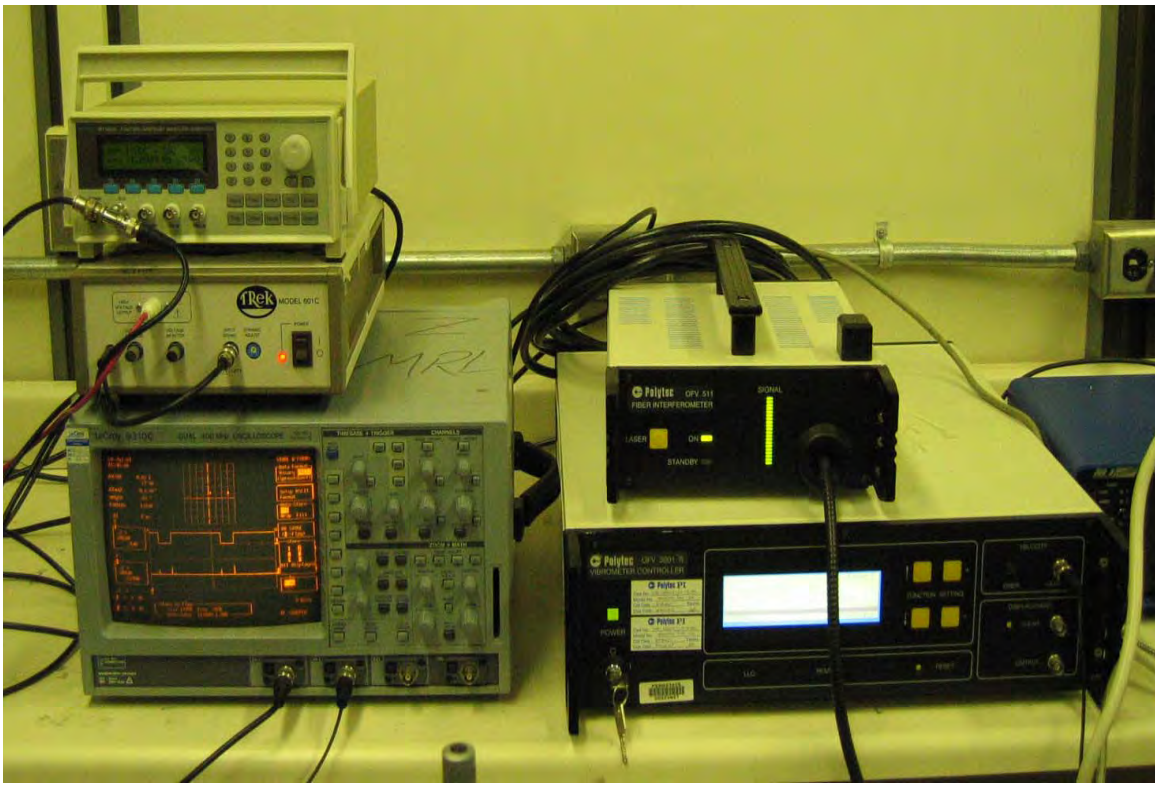

Fig. C.2: Picture of dynamic experimental test stand.

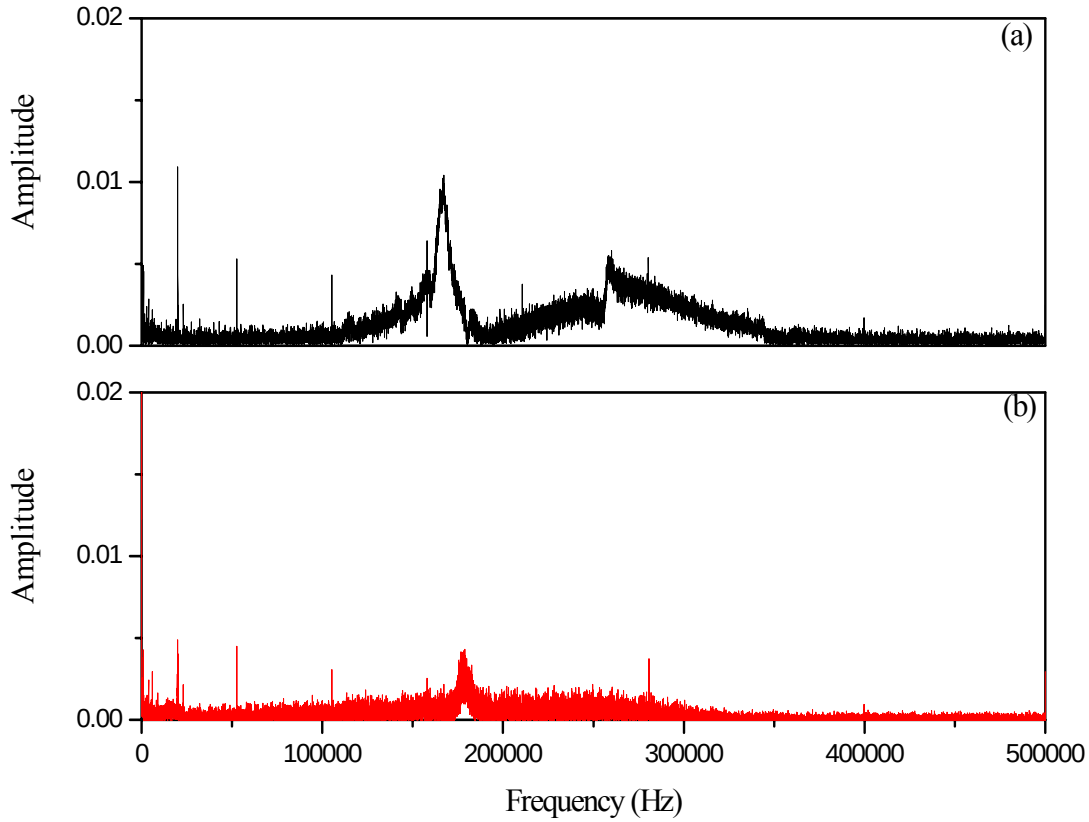

Fig. **C.3**: Frequency function response of PZT according to mounting method: (a) clamp and (b) taping.

Fig. C.4: Picture of a flextensional microactuator mounted on a carbon tape.

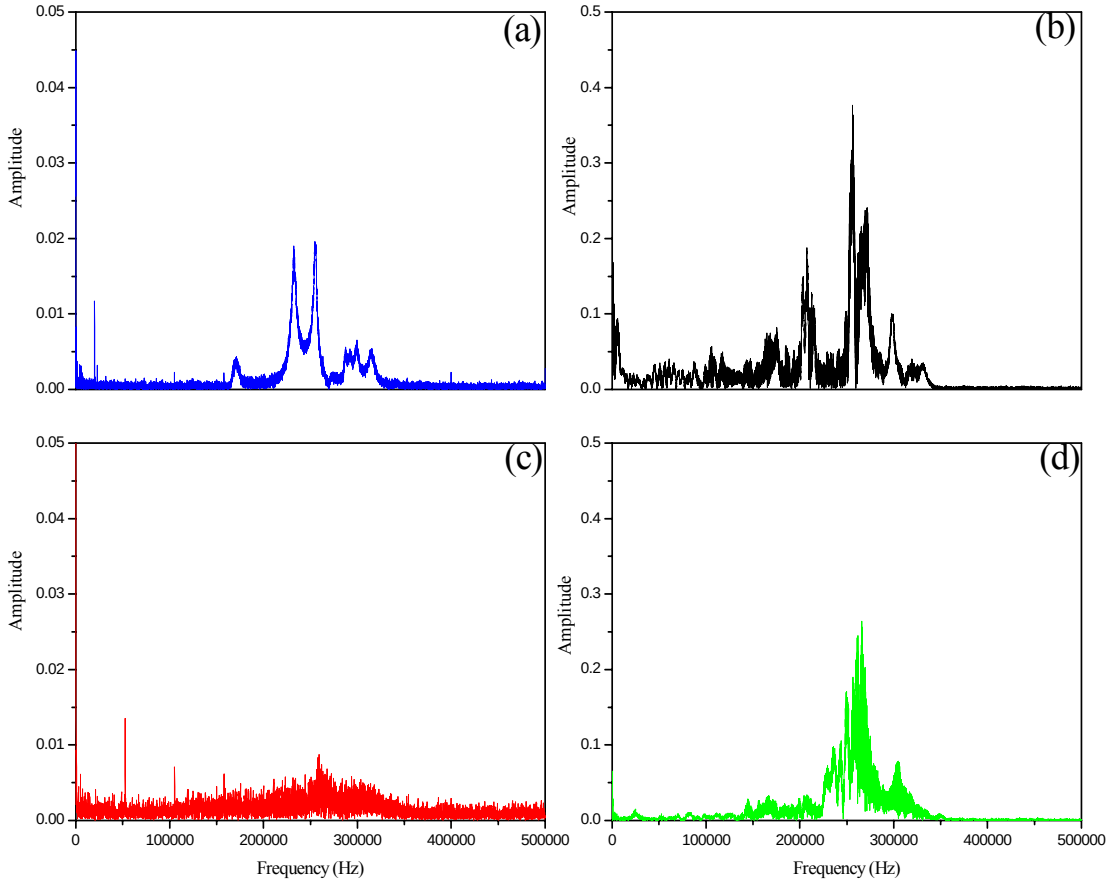

Fig. **C.5**: Frequency response functions of PZT [(a) and (c)] and buckled beam [(b) and (d)] according to clamp [(a) and (b)] and tape [(c) and (d)].

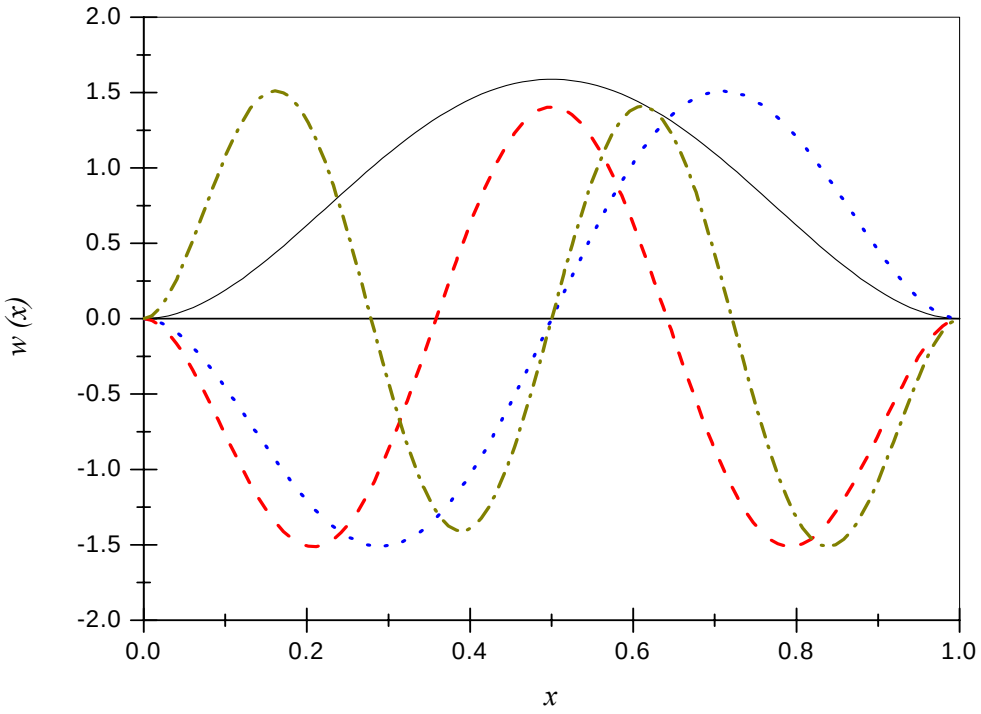

Fig. **C.6**: Four-mode approximation used in Galerkin Discretizaton.

VITA

Jongpil Cheong

Jongpil Cheong was born in Taejon, South Korea in 1971. He received his B.S. in Mechanical Engineering at Korea University in 1998 and his M.S. degree in Mechanical Design & Production Engineering at Seoul National University, Korea in 2000. In fall 2001, he enrolled in the Ph.D. program in Mechanical and Nuclear Engineering at the Pennsylvania State University.

His thesis work was in the area of a piezoelectric flextensional microactuator based on amplifying a displacement and a solder bonding technology in MEMS.